MASTERARBEIT | MASTER'S THESIS

Titel | Title

High-pressure investigations of synthetic teineite

verfasst von | submitted by

Sharif Abdel Azim BSc

angestrebter akademischer Grad | in partial fulfilment of the requirements for the degree of

Master of Science (MSc)

Wien | Vienna, 2025

Studienkennzahl lt. Studienblatt | Degree programme code as it appears on the student record sheet:	UA 066 815
Studienrichtung lt. Studienblatt | Degree programme as it appears on the student record sheet:	Masterstudium Erdwissenschaften
Betreut von | Supervisor:	Univ.-Prof. Mag. Dr. Ronald Miletich

Statement Under Oath

Hereby I declare to have composed my master's thesis completely on my own, using no other sources and help than cited. Direct and indirect trains of thought from other sources are marked as such in an appropriate manner.

Eidesstattliche Erklärung

Hiermit erkläre ich, dass ich diese Masterarbeit selbstständig verfasst und keine anderen als die angegebenen Quellen und Hilfsmittel benutzt und die aus fremden Quellen direkt oder indirekt übernommene Gedanken als solche kenntlich gemacht habe.

Wien, 2025 / Vienna, 2025

Acknowledgement

Primarily I would like to thank Univ.-Prof. Mag. Dr. Ronald Miletich-Pawliczek for entrusting me with this project, taking his time showing me all the necessary basics, his unconditional support and motivating reassurance during this project. Additionally, my thanks belong to Dr. Kamil Dziubek, who was responsible for measuring SXRD* at ELETTRA, helped during SXRD* measurements at the IfMK** as well as refinement of structure data, always made time to share his experience and aided me on my way through the project. Special thanks also belong to ao. Prof. i.R. Dr. Herta Silvia Effenberger, offering her valuable time and profound expertise, being a key figure during the conduct of SXRD measurements, as well as guiding me patiently through the process of structure refinement. I would also like to thank Sofija Milos, Bsc MSc for the countless occasions she offered her help and shared her experience, even when she herself was having limited time. Another person this project would have been impossible without is Dr. Dominik Talla, who synthesized the samples used in this study and aided me multiple times with technical issues during Raman measurements. Also, I would like to thank Thomas Rosen for setting up my working PC and providing required programs for data processing, as well as Wolfgang Prosche and Erich Polacek for refilling liquid nitrogen for cryogenic Ar loading and ao. Prof. Mag. Dr. Gerald Giester for providing necessary chemical agents. Finally, I would like to thank my family and friends, who endured my journey through the bachelors' and masters' studies and made sacrifices on my behalf. Without you, none of this would have been possible.

* SXRD - Single Crystal X-Ray Diffraction
** IfMK - Institut für Mineralogie und Kristallographie der Universität Wien

Abstract

Synthetic teineite ($CuTeO_3 \cdot 2H_2O$, space group $P2_12_12_1$) was isothermally compressed up to 8 GPa by means of an ETH-type diamond anvil cell. Upon compression in-situ Raman spectroscopy analysis revealed a first-order phase transition between 6.86 and 7.67 GPa. In addition to the expected blueshift of Raman bands between 50 and 850 cm^{-1}, as well as softening of Raman modes, novel dominant bands emerged at around 391 and 440 cm^{-1}, associated with the v_4 Raman mode and 720 cm^{-1}, correlated to the v_3 Raman mode. Developing from the orthorhombic base vectors *a*=6.63 Å, *b*=9.62 Å and *c*=7.43 Å at 1 bar, SXRD data at 7.52 GPa display a shrinkage of unit-cell parameters *a* of 21.99%, *c* of 9.84% and an increase of 5.63% for parameter *b*, while maintaining the initial spacegroup and coordination numbers of 4+1 for Cu. However, the Te coordination environment experiences a pressure induced modification from the initial coordination number of 3 to 3+3. The proposed high-pressure structure model indicates a reorientation of coordination polyhedra, as well as change in connectivity, from Te and Cu coordination polyhedra initially sharing solely corners to sharing an edge in addition. The cumulation of these conditions result in a structural compaction, most notable within the (010) plane. Following decompression, Raman spectra revealed the existence of a significant hysteresis, with a phase transition reversal occurring between 3.26 and 1.54 GPa. This is marked by discontinuities of Raman band shifts and large steps in pressure, in consequence of volumetric changes within the crystal.

Zusammenfassung

Synthetischer Teineit ($CuTeO_3 \cdot 2H_2O$, Raumgruppe $P2_12_12_1$) wurde isothermal auf bis zu 8 GPa komprimiert mittels einer Diamantstempelzelle des ETH Typs. Nach Kompression zeigten in situ Ramanspektroskopieanalysen eine Phasentransformation erster Ordnung zwischen 6,86 und 7,67 GPa an. Zusätzlich zu der erwarteten Blauverschiebung von Ramanbanden zwischen 50 cm^{-1} and 850 cm^{-1}, als auch die Abschwächung von Raman-Moden, tauchten neue dominante Banden bei etwa 391 und 440 cm^{-1} auf, dem v_4 Raman-Mode zuschreibbar und 720 cm^{-1}, korrelierend mit dem v_3 Raman-Mode. Von den orthorhombischen Basisvektoren *a*=6.63 Å, *b*=9.62 Å and *c*=7.43 Å bei 1 bar aus entwickelnd, zeigten SXRD Daten bei 7,52 GPa eine Verkleinerung von Einheitszellenparameter *a* um 21,99%, *c* um 9,84% und eine Vergrösserung von 5,63% für Parameter *b,* während die ursprüngliche Punktgruppe und Koordinationszahl von 4+1 für Cu beibehalten werden. Die Koordinationsumgebung von Te hingegen erfährt eine druckinduzierte Modifikation von der ursprünglichen Koordinationszahl 3 zu 3+3. Das vorgeschlagene Hochdruck-Strukturmodell deutet auf eine Reorientierung von Koordinationspolyedern hin, als auch Verbindung dieser, wobei anfänglich Te und Cu Koordinationspolyeder ausschließlich Ecken teilten und nun auch eine Kante. Die Kumulierung dieser Umstände resultieren in einer strukturellen Kompaktion, am deutlichsten erkennbar in der (010) Ebene. Der Dekompression folgend, offenbarten Ramanspektren das Vorhandensein einer deutlichen Hysterese, mit einer Rücktransformation der Phase zwischen 3,26 und 1,54 GPa stattfindend. Diese ist gekennzeichnet durch Diskontinuitäten des Ramanbandenshifts und starke Drucksprünge, infolge der volumetrischen Änderungen innerhalb des Kristalls.

Table of Contents

1. Introduction

Industrial Relevance of Te-Bearing Minerals

Tellurite minerals are a group of compounds that are rare in the Earth's crust. These minerals typically form in the oxidation zones of ore deposits as secondary phases. While tellurite minerals themselves are not directly used in industry, the extractable element tellurium has several important industrial applications, such as being part of solar cells (Das and Banik, 2022), semiconductor devices (Berger, 1997), as well as catalysts (Knee, 1984). In the optical industry, tellurite glasses have gained broad attention due to their exceptionally wide transparency window and high refraction index, making them key components in optical fibers and infrared optics (Jha et al., 2012).

State of Knowledge and Previous Work

Te-bearing oxycompounds exhibit a diverse array of structural motifs, ranging from monomeric and layered configurations to cyclic and non-cyclic finite oligomers. Tellurium in its 4+ oxidation state, as in the case of teineite, demonstrates a wide spectrum of coordination numbers, often encompassing 3-, 4-, and 5-fold coordination with oxygen but seldom 2- and 6-fold coordination (Christy et al., 2016). In terms of symmetry, structural features, such as the acentricity of the Te^{4+} polyhedron, can often result in the manifestation of unusual physical properties, including non-linear optical behavior (Christy et al., 2016). Teineite, which was first discovered in 1939 at the Teine mine, Hokkaido (Japan) (Yosimura, 1939), can be classified as a tellurite mineral without additional cations and with H_2O. The mineral with its typical blue color has the chemical formula $Cu^{2+}Te^{4+}O_3 \cdot 2H_2O$ (Zemann and Zemann, 1960) and crystallizes in the orthorhombic space group (no.19) $P2_12_12_1$ (Strunz and Nickel, 2001). Effenberger (1977) described the crystal structure of teineite as a three-dimensional net, where copper is coordinated 4+1 by oxygen atoms, creating a figure, similar to a tetragonal pyramid in an almost square planar arrangement at the base and an additional oxygen atom representing the tip of said polyhedron. Tellurium forms a TeO_3 pyramid together with three oxygen atoms, a coordination also typically seen in zemannite (Miletich, 1995). The position of H-atoms could not be assessed by X-ray diffraction at the time and was only determinable by means of bond strength calculations and geometry (Effenberger, 1977).

Since its initial discovery in 1939, teineite has also been found in several other locations, as proceeding studies focused on several topics, such as formation and alteration processes, Raman spectroscopy and SXRD. For further references see Rewitzer (2001), Anthony et al. (1995), Du Ry et al. (1976), Andreeva et al. (2013), Isbrekken (1991), Kato and Sakurai (1968) and Williams and Matter (1975).

Motivation and aim of this Study

As already mentioned, several studies focused on teineite, such as formation conditions, crystal structure, Raman spectra and associated mineral assemblages. Efforts of conducting this study were mainly driven by considering an already known natural isochemical polymorph of teineite, i.e. millsite (Rumsey et al., 2018). Moreover, high-pressure investigations of teineite's Se-analogue, chalcomenite (Gonzalez-Platas et al., 2019), were also taken as motivation, being in the same spacegroup (no.19) as teineite and potentially comparable in terms of Raman band changes as a result of phase transitions. Additionally, given the relative scarcity of high-pressure studies on tellurite minerals, the potential of finding novel high pressure polymorphs can be deemed relatively high. With this the primary objective was to investigate the minerals' structure under high pressure, specifically identifying and characterizing phase transitions, for both compression and decompression. Thus, apart from optical microscopy for visual characterization, Raman spectroscopy and single crystal X-ray diffraction (SXRD) were used as complementary methods to conduct this study.

2. Methods

2.1 Synthesis

As for the process of synthesis, teineite was created via recrystallization of a solid precipitation product (Cu-Te-O precursor) in contact with an aqueous solution of $CuSO_4$ at room temperature. For this three major steps were necessary: first, K_2TeO_3(aq) was produced by letting the chemical agents described in Equation 1) react in a beaker placed on a magnetic stirrer, mixing the components at 80°C for about an hour and adding additional TeO_2(s) to keep an excess of the component until the reaction was deemed complete. After that K_2TeO_3(aq) was filtered away and stored for the next step.

$$TeO_2(s) + 2KOH(aq) = K_2TeO_3(aq) + H_2O(l) \quad (1)$$

In the second step a Cu-Te-O precursor ($CuTeO_3$ x H_2O (s)) was created by mixing K_2TeO_3(aq) and $CuSO_4$(aq) in a beaker with an excess of $CuSO_4$(aq) according to the reaction:

$$K_2TeO_3(aq) + CuSO_4(aq) = K_2SO_4(aq) + \downarrow CuTeO_3 \; x \; H_2O \; (s) \quad (2)$$

Afterwards, the solid products were filtered via vacuum filtration, washed multiple times with distilled water and dried. For the final step a $CuSO_4$ solution with an optimal pH range between of 3-3.5 was poured over the Cu-Te-O precursor, which was placed in a beaker. After 48 months, a batch of synthetic teineite, visible in Figure 1, was yielded, of which chosen crystals were used in this study.

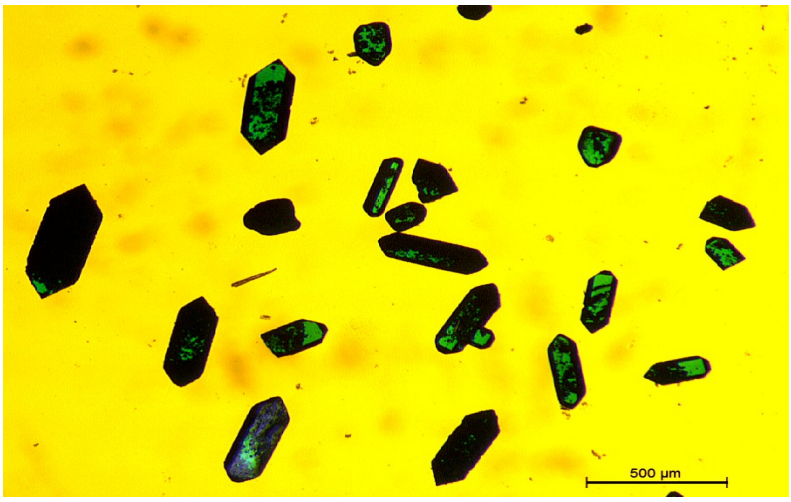

Figure 1: picture taken from a small fraction of synthetic teineite crystals yielded after 48 months of growing.

2.2 Diamond Anvil Cell and Loading Procedures

For applying hydrostatic pressure diamond anvil cells (DACs) of the ETH-type (Allan et al.,1996; Miletich et al., 2000) with a Boehler-Almax diamond culet of 0.6 mm and tungsten carbide supported seats were used (see Figure 2), mounted with a steel gasket to create a pressure chamber and loaded with a synthetic teineite crystal and ruby each time, being pressurized up to 8 GPa.

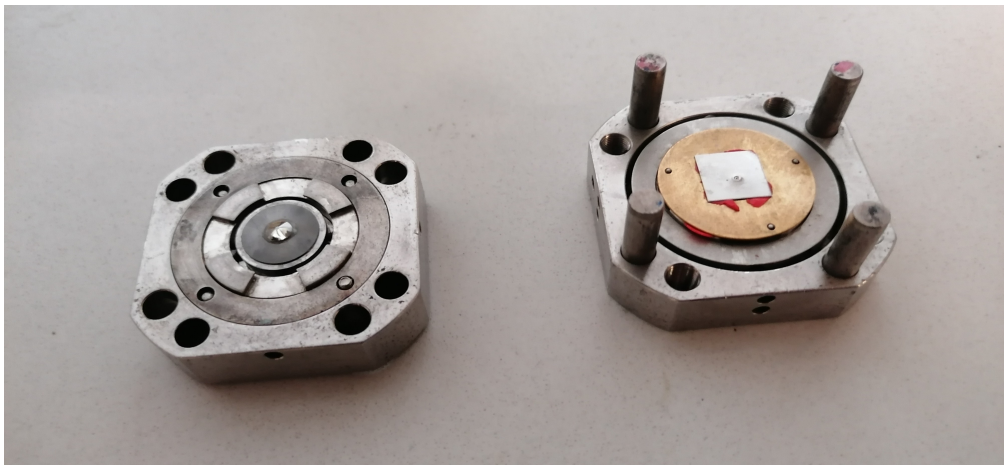

Figure 2: ETH-type diamond anvil cell. Left: DAC part with visible diamond culet in the center. Right: DAC part with mounted gasket.

All used DACs and gaskets with their specifications are listed in Table 1. The respective gaskets were produced by creating an indent on a steel gasket, initially 250 µm in thickness, and pressed down to a range in between 90 and 110 µm. Afterwards, a hole was drilled with a Boehler µDriller from Almax-easyLab, using a tungsten needle with 250 µm in diameter.

Table 1. Gasket and loading method specifications for conducted Raman and X-ray (conventional X-ray tube and Synchrotron radiation) investigations at non-ambient pressure conditions.

DAC [a]	h [µm] [b]	d [µm] [c]	offset [µm] [d]	loading [e]	series [f]
#25	109(3)	270(5)	5 right; 5 top	cryogenic Ar	s1
#23	102(3)	260(5)	1 right; 2 bottom	gas loading Ar	x-ray 1/ axr1
#12	97(3)	265(5)	6 right; 6 bottom	gas loading Ar	s2
#23	103(3)	270(5)	1.5 right; 6.5 bottom	4:1 M-E	x-ray 2/x-ray 3

[a] ETH-type diamond anvil cell with 0.6mm diamond culets and tungsten carbide seats used for experiments.
[b] Height of the steel gasket after pre-indentation.
[c] Diameter of the pre-experimental drill hole of the gasket.
[d] Drill hole offset with the gasket facing the same side as during pre-indentation.
[e] Conducted methods of loading pressure transmitting media within the diamond anvil cell.
[f] Series of conducted experiments: s1, s2 and axr1 are Raman measurement series, whereas x-ray 1 and x-ray 2 are SXRD measurements conducted with MoKα radiation and x-ray 3 with synchrotron radiation.

The loading for the first Raman measurement series was carried out by loading the cell cryogenically with liquid Argon (Mao and Bell, 1980) (see Figure 3).

Figure 3: Apparatus for cryogenic loading of Argon. Left: Styrofoam container, used for placing the autoclave (middle) inside and filling the container with liquid nitrogen in the space between to cool down the gaseous Ar inside the autoclave. Right: lid for the autoclave.

Afterwards, multiple attempts to load the cell in the same way failed, as the crystals seem to lose their adhesion to the diamond culet very easily as soon as they are drenched in a liquid substance. Due to this issue, gas loading with Argon (see Figure 4) was conducted for both, Raman measurement series s2 as well as axr1/x-ray 1, to reduce the risk of operator induced movement of the crystal during the DAC closing procedure.

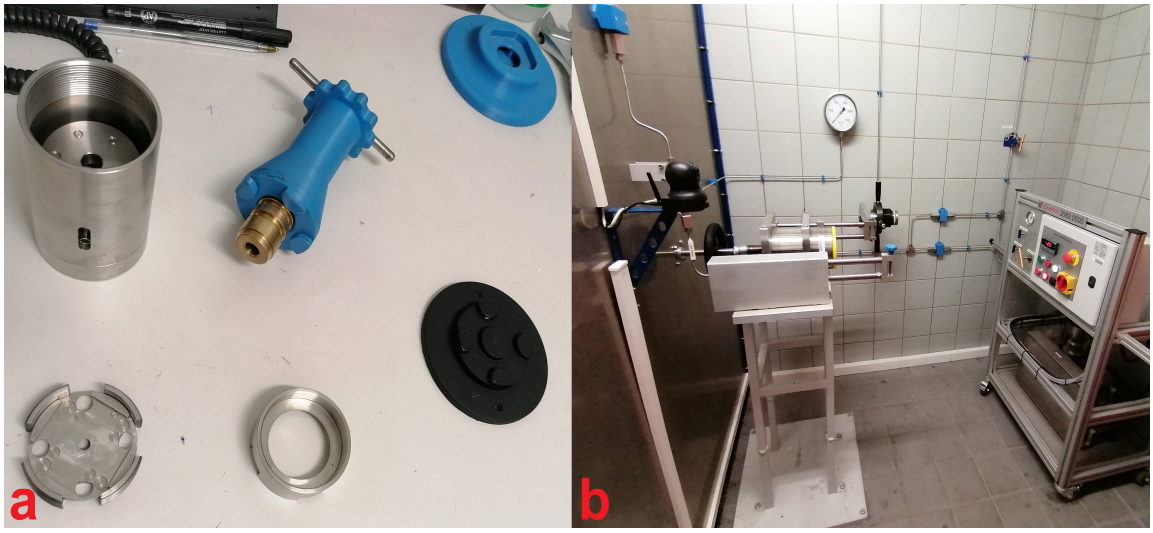

Figure 4: a) Device for loading the cell into the gas loading system; **b)** gas loading system, left: chamber for loading the fixed DAC into the system, right: control panel for checking pressure.

Observed from all the previous measurement series, crystals were demonstrating the emergence of multiple domains during pressure increase. Therefore, the pressure medium was switched from Argon to a 4:1 Methanol-Ethanol mixture (Klotz et al., 2009), loaded manually for ”x-ray 2” and “x-ray 3“. Referring back to the problem of crystals losing their adhesion to the diamond culet, this was also the case for loading attempts with 4:1 M-E, partially due to the appearance of bubbles inside the sample chamber.

2.3 Optical Microscopy

To evaluate crystal morphology and dimensions for experimental selection optical microscopy was applied. Furthermore, it enabled the monitoring of possible pressure-driven domain formation and laser-induced sample alteration during Raman measurements. The equipment used consisted of 3 different devices located at the IfMK: First, the Leica M165C with 0.73-12x magnification was operated. Second, an x5 and x50 LWD objective was utilized during Raman measurements with the Horiba LabRAM HR. Third, the KEYENCE VHX7100 microscope, with integrated focus stacking and with a 20-60,000x magnification range was used.

2.4 Raman Spectroscopy

Data for Raman spectroscopy was derived by working with a Horiba LabRAM HR at the IfMK equipped with a HR800 spectrometer (Horiba Jobin Yvon) and a Si-based, Peltier cooled CCD detector in accordance with backscattering geometry. Further, a 532 nm excitation laser was used with 1800 lines per mm grating and a x50LWD objective (detailed measurement settings are described in chapter 3.2). For calibration a silicon standard sample, provided by HORIBA, was used to calibrate in accordance to the Rayleigh line. Labspec6 (HORIBA Scientific) was used to generate data and those obtained spectra were fitted via Peakfit (Systat Software, Inc.), in which the Gauss-Lorentz area method was applied. All graphs were constructed by using Gnuplot (administered through SourceForge). To calculate the pressure inside the loaded DAC the position of the R1 luminescence line of ruby (Datchi et al., 2007) was used and its value integrated into the following formula (Shen et al., 2020):

$$P\,[GPa] = 1.87(\pm 0.01)\times 10^{3}\,(\Delta\lambda/\lambda_0)\,[1+5.63(\pm 0.03)(\Delta\lambda/\lambda_0)] \qquad (3)$$

The R1 line of ruby luminescence at 1 bar was measured and showed different positions for each loading, which can be the result of multiple causes. Conditions of the measured ruby, such as strain and variable Cr concentration (Shen et al., 2020) must be taken into account. Another reason, which is neglectable if a proper standard sample was chosen, is the calibration of the Raman device to the Rayleigh line, as it is only possible to approximate the zero position, thus, always carrying an error of a certain degree into received data. For compression and decompression timetables, as well as initially tracked Raman bands for all high-pressure measurement series please refer to the Appendix.

2.5 Single Crystal X-Ray Diffraction

SXRD measurements were conducted at the IfMK, using the STOE StadiVari, equipped with an open Eulerian cradle, MoKα microfocus X-ray tube and Dectris Pilatus 300k detector, using X-Area (Stoe & Cie GmbH) as operating and data integration program. For model refinement SHELX (Sheldrick, 2008) was used with the scaling approach, also applied via SHELX. For measuring pressure inside the diamond anvil cell, the shift of the R1 luminescence line of ruby (Shen et al., 2020) was utilized. Additionally, single-crystal X-ray diffraction (λ = 0.4956 Å, beam diameter ca. 80 µm) measurements under pressure were performed on the Xpress beamline at the Elettra Sincrotrone Trieste (Lotti et al., 2020). The PILATUS3 S 6M detector was placed at 249.9 mm from the sample. The pressure was measured based on the shift of the R1 luminescence line of ruby (Shen et al, 2020). The beamline parameters were calibrated with CeO_2 powder and a quartz single crystal using the programs Dioptas (Prescher and Prakapenka, 2015) and CrysAlisPro (Rigaku Oxford Diffraction, 2024), respectively. Data collections were performed using step scans of 0.5° with 0.3 s exposure over a total ω scan range of ±37°. The lattice parameters and the integrated intensities of the Bragg reflections were obtained from the measured images using the program CrysAlisPro (Rigaku Oxford Diffraction, 2024). The crystal structure was solved using direct methods implemented in the SHELXT program (Sheldrick, 2015), while the iterative structure refinements were performed with SHELXL (Sheldrick, 2008). Structure models are displayed via the program VESTA (Momma and Izumi, 2011). For further information regarding timetables for compression and decompression refer to the Appendix.

3. Results

3.1 Optical Microscopy

In this section figures are displayed from samples used for high-pressure Raman measurements and high-pressure single-crystal X-ray diffraction (HP-SXRD). Their appearance as well as change of such with varying pressure will be discussed in chapter 3.2 for high-pressure Raman measurements and in chapter 3.3 for HP-SXRD measurements.

High-Pressure Raman Measurement Series s1

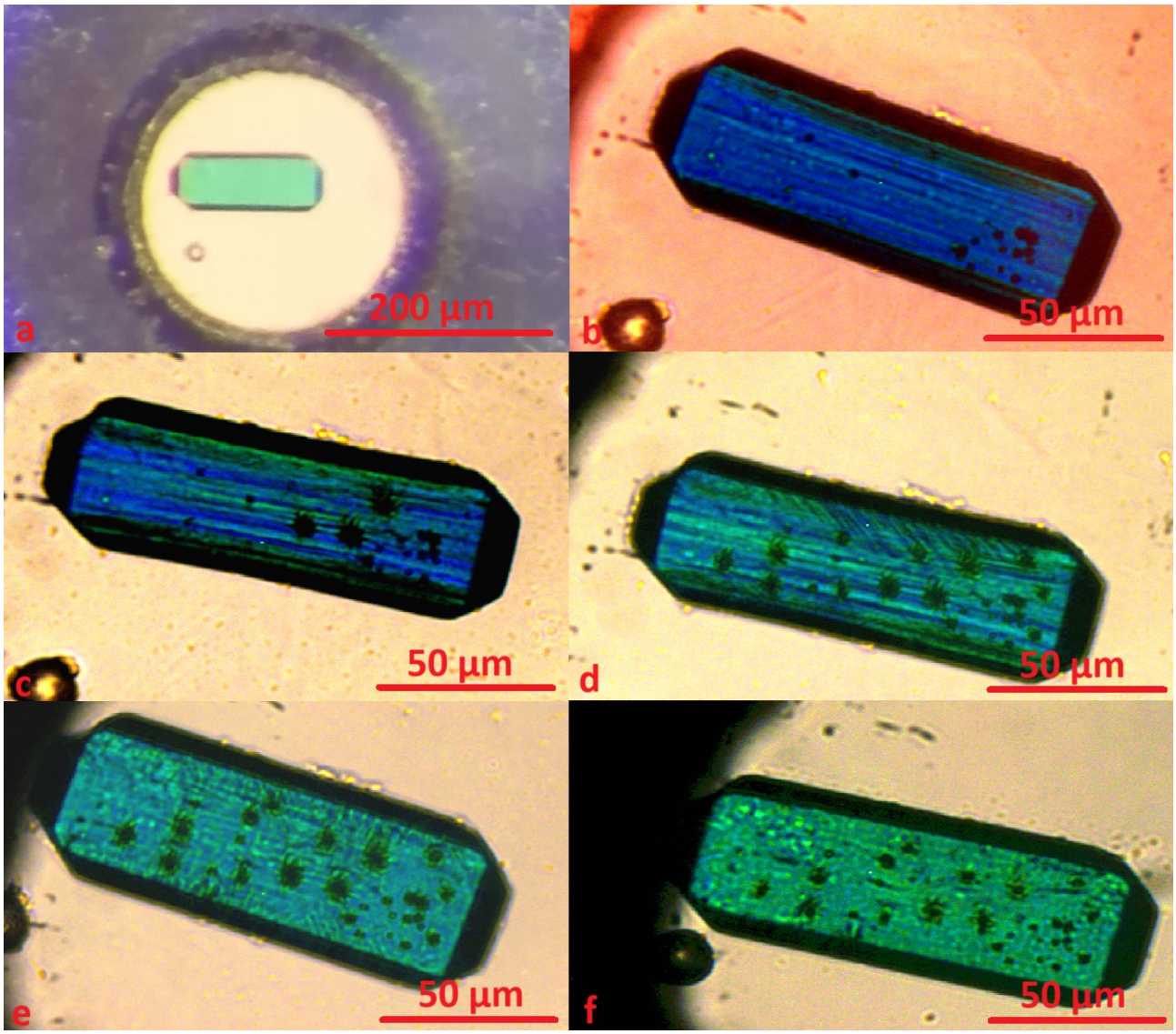

Figure 5: Microscopic pictures of synthetic teineite for high-pressure Raman measurement series 1: **a)** sample and ruby (lower left corner) after loading at 1.56 GPa; **b)** synthetic teineite with visible lamellae at 6.86 GPa during compression; **c)** synthetic teineite with significant laser-induced damage at 7.36 GPa before decompression; **d)** crystal at 5.68 GPa showing two lamellae directions with a 45 degree tilt relative to each other; **e)** lamellae becoming seemingly less visible at 1.54 GPa during decompression; **f)** visible disappearance of previously seen distinctive lamellae after the final decompression step reaching 1 bar.

High-Pressure Raman Measurement Series axr1/ HP-SXRD Measurement x-ray 1

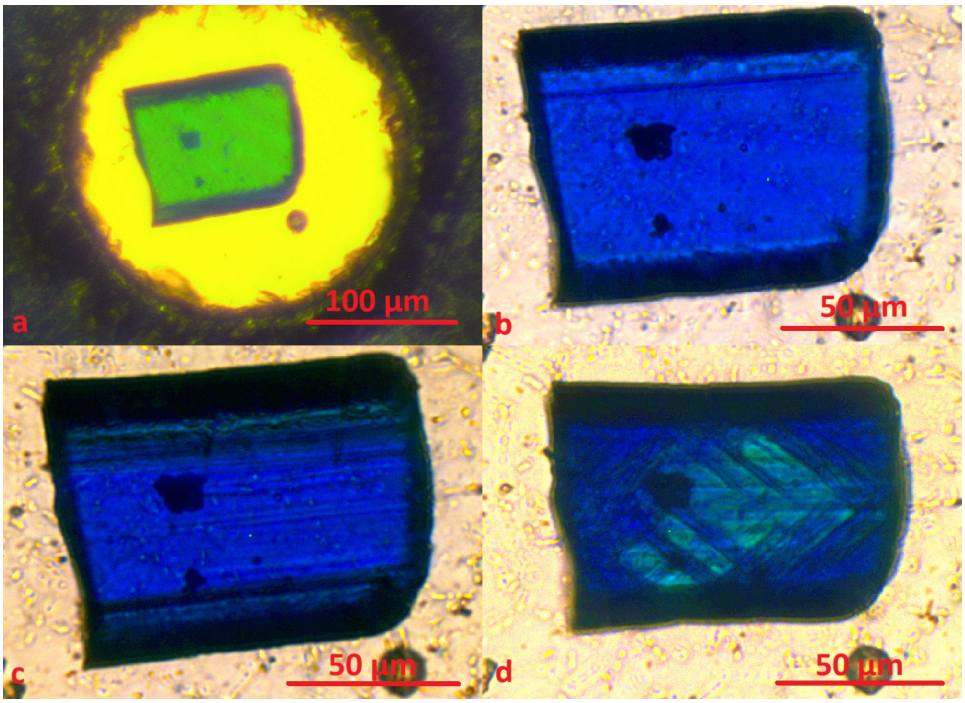

Figure 6: Microscopic pictures of synthetic teineite for high-pressure Raman measurement series axr1/ HP-SXRD measurement x-ray 1: **a)** sample after loading inside diamond anvil cell at 1.13 GPa; **b)** synthetic teineite at 6.85 GPa displaying a grain boundary within the crystal; **c)** multiple visible lamellae on synthetic teineite at 7.30 GPa; **d)** intricate pattern of grain boundaries within the sample at 7.67 GPa.

High-Pressure Raman Measurement Series s2

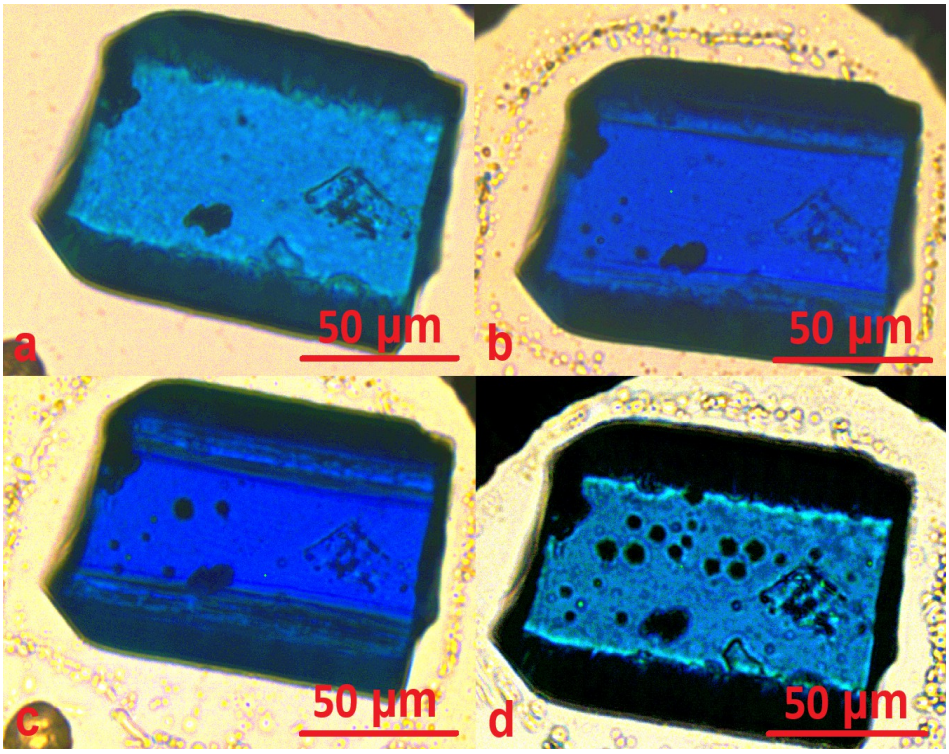

Figure 7: Microscopic pictures of synthetic teineite for high-pressure Raman measurement series s2: **a)** sample crystal at 1.03 GPa**; b)** synthetic teineite showing first signs of grain boundaries inside the crystal at 7.14 GPa **; c)** multiple domains visible within the sample crystal at 7.84 GPa**; d)** synthetic teineite at 1.96 GPa apparently showing the disappearance of innermost lamellae.

HP-SXRD Measurement x-ray2/x-ray 3

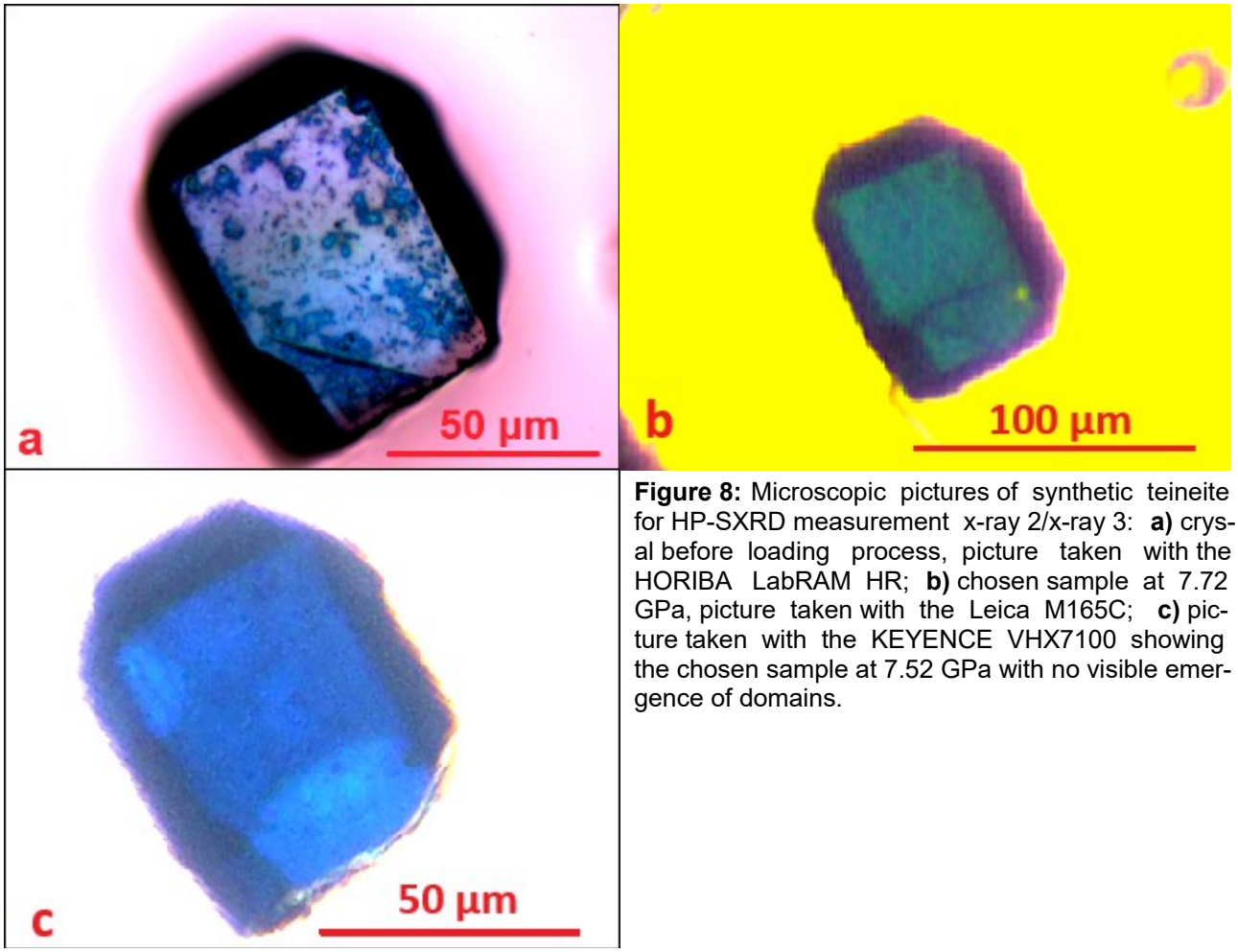

Figure 8: Microscopic pictures of synthetic teineite for HP-SXRD measurement x-ray 2/x-ray 3: **a)** crystal before loading process, picture taken with the HORIBA LabRAM HR; **b)** chosen sample at 7.72 GPa, picture taken with the Leica M165C; **c)** picture taken with the KEYENCE VHX7100 showing the chosen sample at 7.52 GPa with no visible emergence of domains.

3.2 Raman Spectroscopy

Ambient Measurements

Measurements at 1 bar were carried out at first to establish a basic knowledge of the samples' Raman bands (see Figure 9), making it possible to compare to already existing spectra but also to clarify the possibility of sample alteration due to longer laser exposition. The basic setting in Labspec6 was as follows: 532 nm excitation laser, 1800 lines per mm grating, 2 to 15 sec acquisition, 2 accumulation, slit 100, hole 300, x50 LWD objective, a range in between 50 to 850 cm^{-1} and varying filter settings from 10% to 100%. Adapting the filter and acquisition time settings are necessary, especially when moving up in pressure, as the sample is easily damaged by the laser at higher settings, which leaves visible marks even at ambient conditions. Thus, raising the background noise in received spectra, as well as broadening of attained Raman bands.

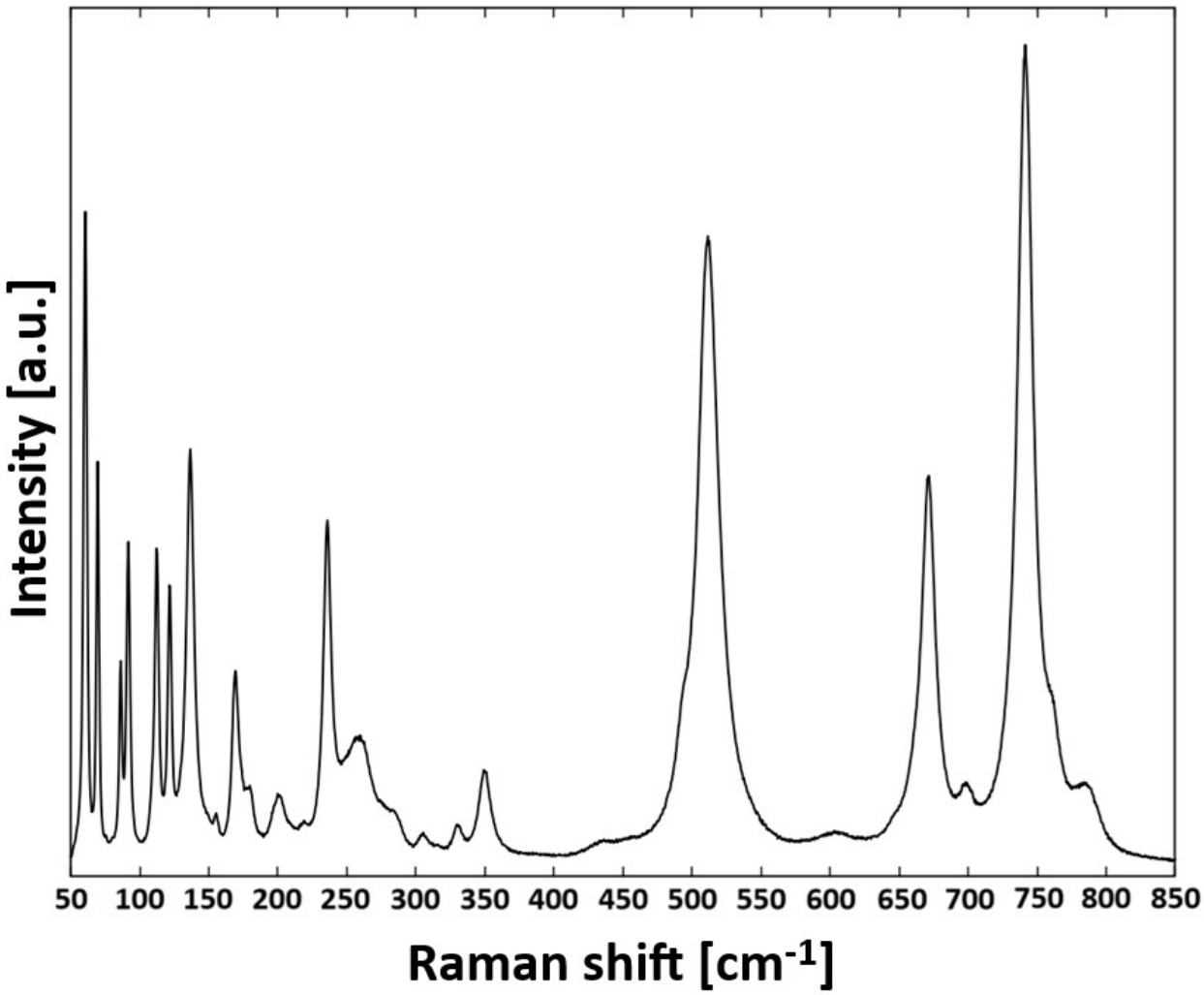

Figure 9: Ambient measurement of significant Raman bands for synthetic teineite on the HORIBA LabRAM HR with Labspec6.

For this reason, measurement points had to be changed on the sample as well. This was proceeded by measuring three samples in different orientations, with the beam path being parallel to the crystallographic b-axis (with cell metrics lineup b>c>a, after Zemann and Zemann (1960)), to examine the difference in intensity relative from one Raman band to another. The first orientation dependent measurement series (see Figure 10) was carried out by measuring a synthetic teineite crystal, 340x120x80 µm in size, with the previously mentioned parameters, this time with 5 seconds acquisition and 10% filter. The crystal was turned counterclockwise for 10 degrees after every measurement, until 180 degrees were reached in total. The second orientation dependent series (see Figure 11) was done by measuring a crystal with a size of 105x80x40 µm.

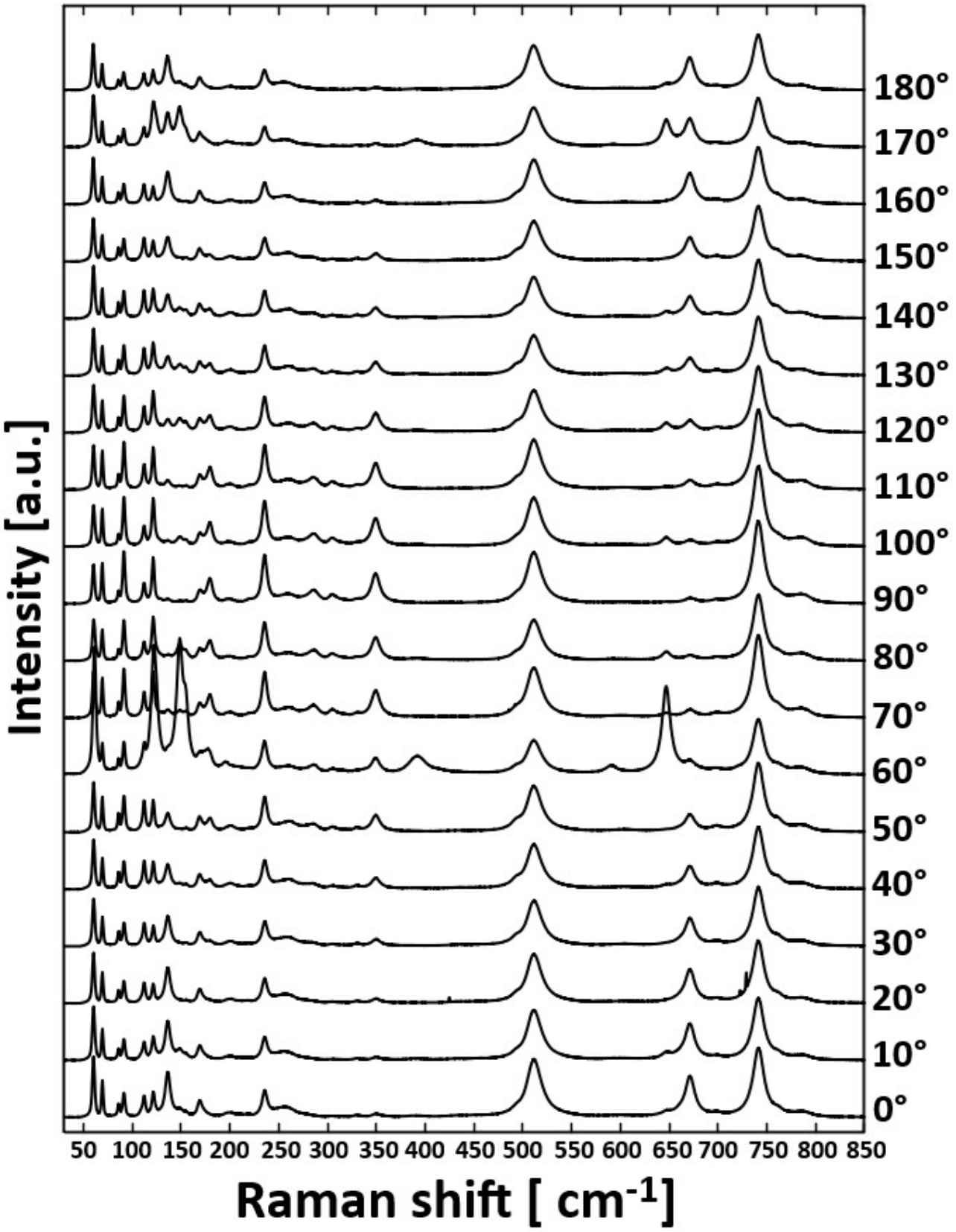

Figure 10: First orientation Raman measurement series for synthetic teineite at ambient conditions. The crystal was turned counterclockwise in 10 degree steps until 180 degrees were reached. Vertical offset of spectra for demonstration purposes only.

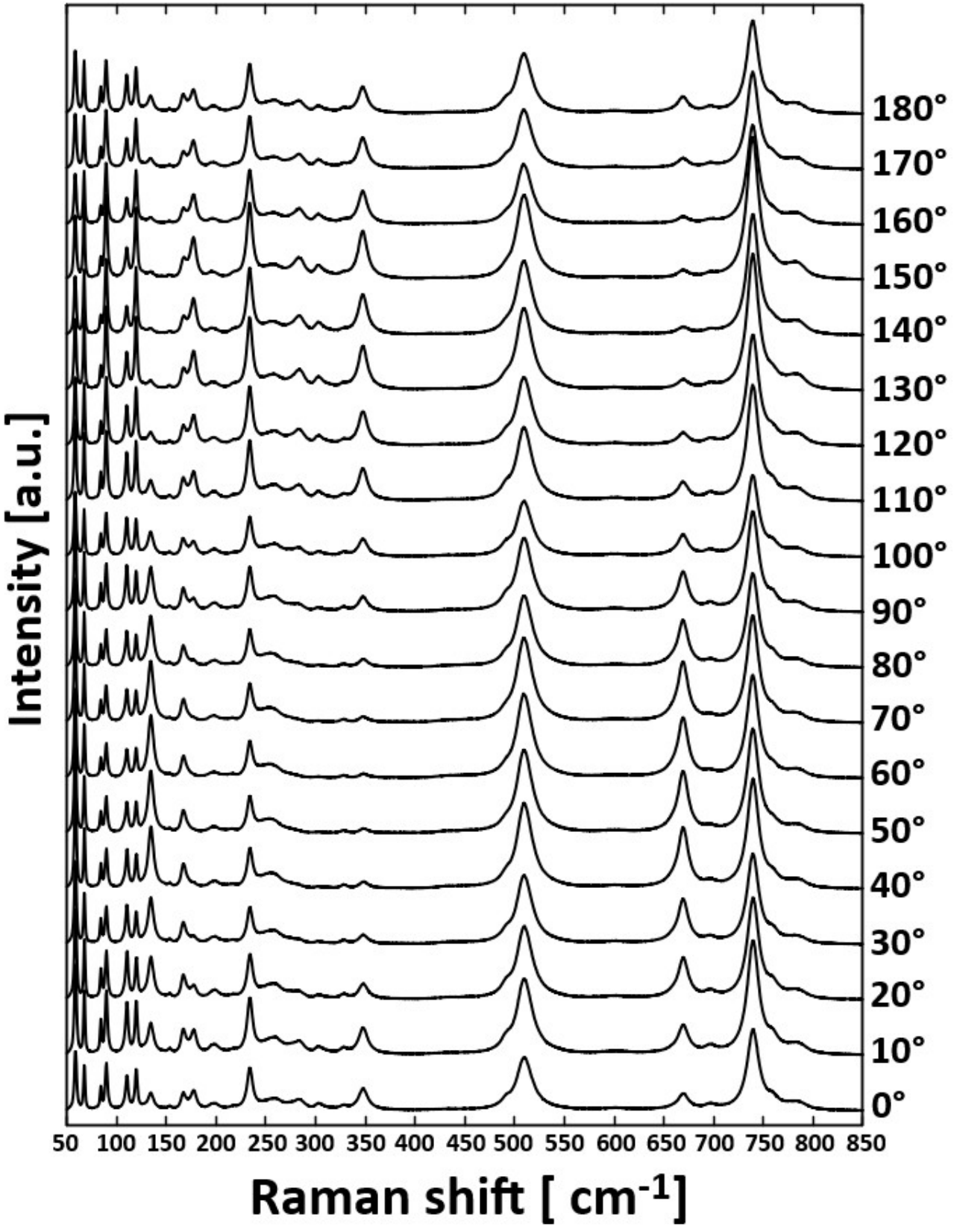

Figure 11: Second orientation Raman measurement series for synthetic teineite. The crystal was turned counterclockwise in 10 degree steps until 180 degrees were reached. Vertical offset for demonstration purposes only.

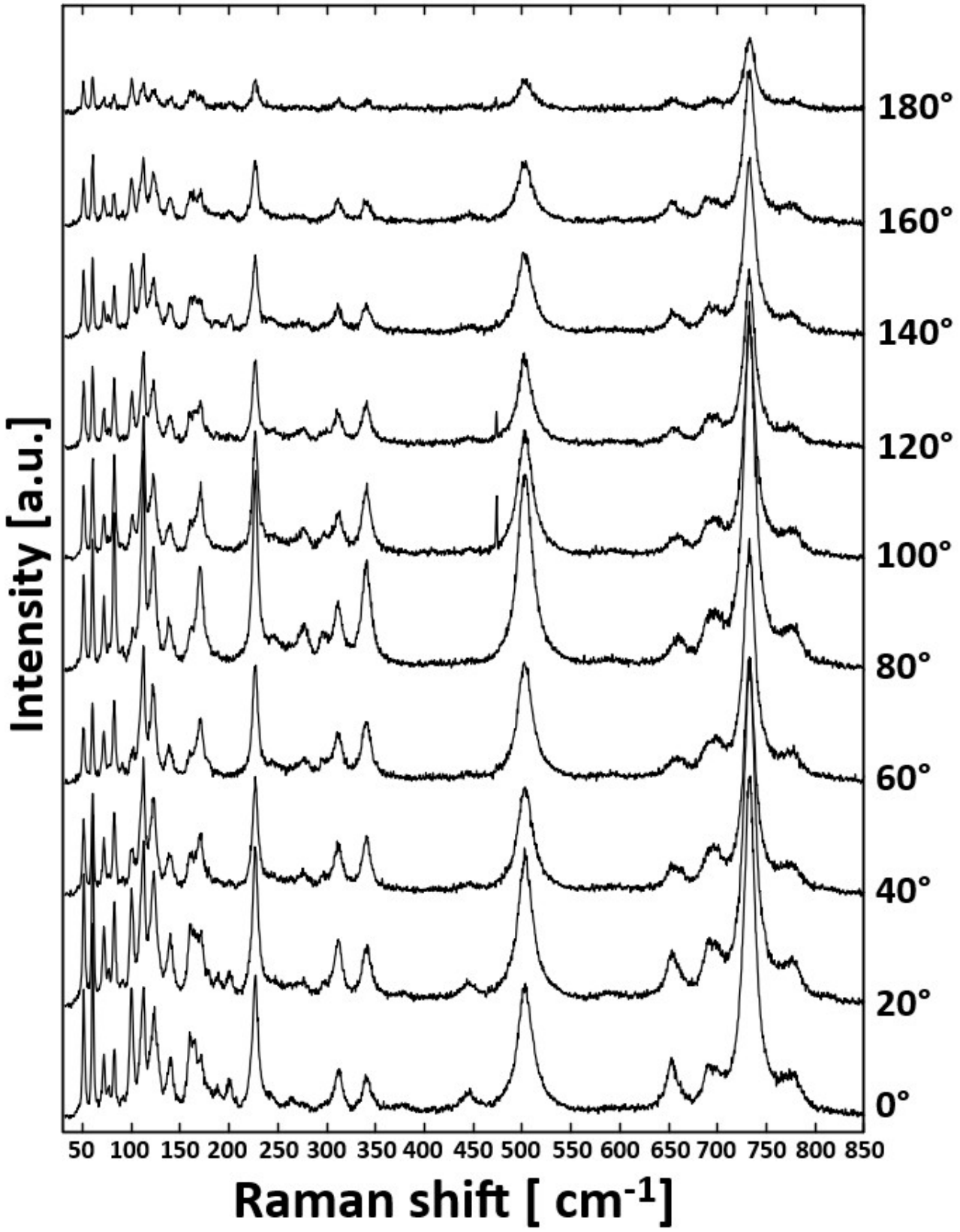

Figure 12: Third orientation dependent Raman measurements for synthetic teineite. The crystal was turned counterclockwise in 20 degree steps until 180 degrees were reached. Vertical offset integrated for visual purposes only.

As with the previous orientation measurements, the crystal for the second series was turned counterclockwise in 10 degree steps for each spectra, until the crystal was turned 180 degrees in total. For these measurements 15 sec acquisition and 25% filter with the discussed settings in the beginning of chapter 3.2 were chosen. The third orientation dependent ambient measurements (see Figure 12) were conducted by turning a synthetic teineite crystal, 280x120x40 µm in size, counterclockwise in 20 degree steps until 180 degrees were reached. Previously mentioned settings were used, with the difference of using 2 sec. acquisition and 10% filter.

Following the display of ambient Raman measurements of synthetic teineite, pressure variable Raman spectra will be shown, starting with Raman measurement series s1. Results are presented in the order of Table 1 from top to bottom. The first series, as well as series s2 consist of compression and decompression experiments. For Raman series axr1, the same cell was used beforehand for an SXRD measurement (x-ray 1). To avoid damage to the sample by the laser, the synthetic teineite was compressed without measuring the crystal with the Horiba LabRam HR. When at least 7 GPa was reached, a X-ray measurement was conducted and afterwards Raman measurements during decompression were done. Measurement setups, as well as changes, if occurred, will be noted for each measurement series.

High-Pressure Raman Measurement Series s1

For series s1 DAC025 was loaded with a synthetic teineite crystal of 140x60x40 µm in size (see Figure 5a). The Labspec6 setup for series s1 consisted of the following parameters: 532nm laser, 1800 grating, x50LWD objective, 15 sec acquisition, 2 accumulation, slit 100, hole 300. In the beginning a filter of 100% was applicable up until 2.57 GPa, where the filter was turned down to 50% due to increasing laser damage with rise in pressure. Compression series 1 was conducted over the course of 9 days. As the DAC was compressed no further visible changes in the crystal lattice were noticed, until lamellae appeared at 6.86 GPa (see Figure 5b), before the last measurement steps were taken. As displayed in Figure 13, Raman bands at initially 112 and 120 cm^{-1} are distinguishable up until 5.34 GPa. Similarly, bands at 85 and 93 cm^{-1} exhibit a reduction in relative intensity, becoming poorly resolved above 5.59 GPa (see Figure 16). At 2.57 GPa a weak Raman band appears at 131 cm^{-1} and gains intensity with increasing pressure. At 7.73 GPa a very dominant band appears at approximately 435 cm^{-1} (see Figure 17).

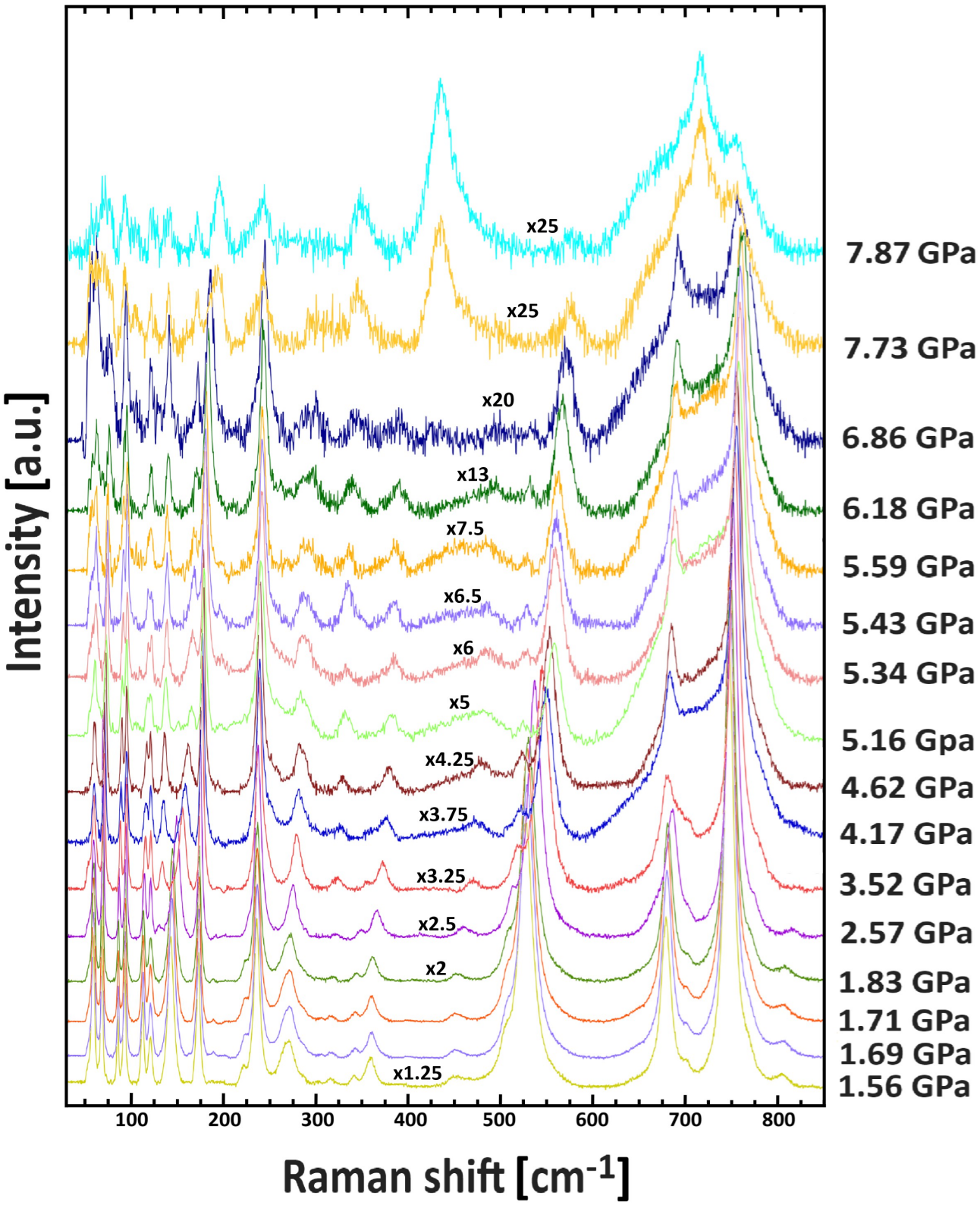

Figure 13: Waterfall plot of subsequent Raman spectra within compression series 1. Start from bottom with continuation onward to the top. Spectra which have been rescaled in the y-axis direction are marked with a multiplier on top. Vertical offset for easier visibility only.

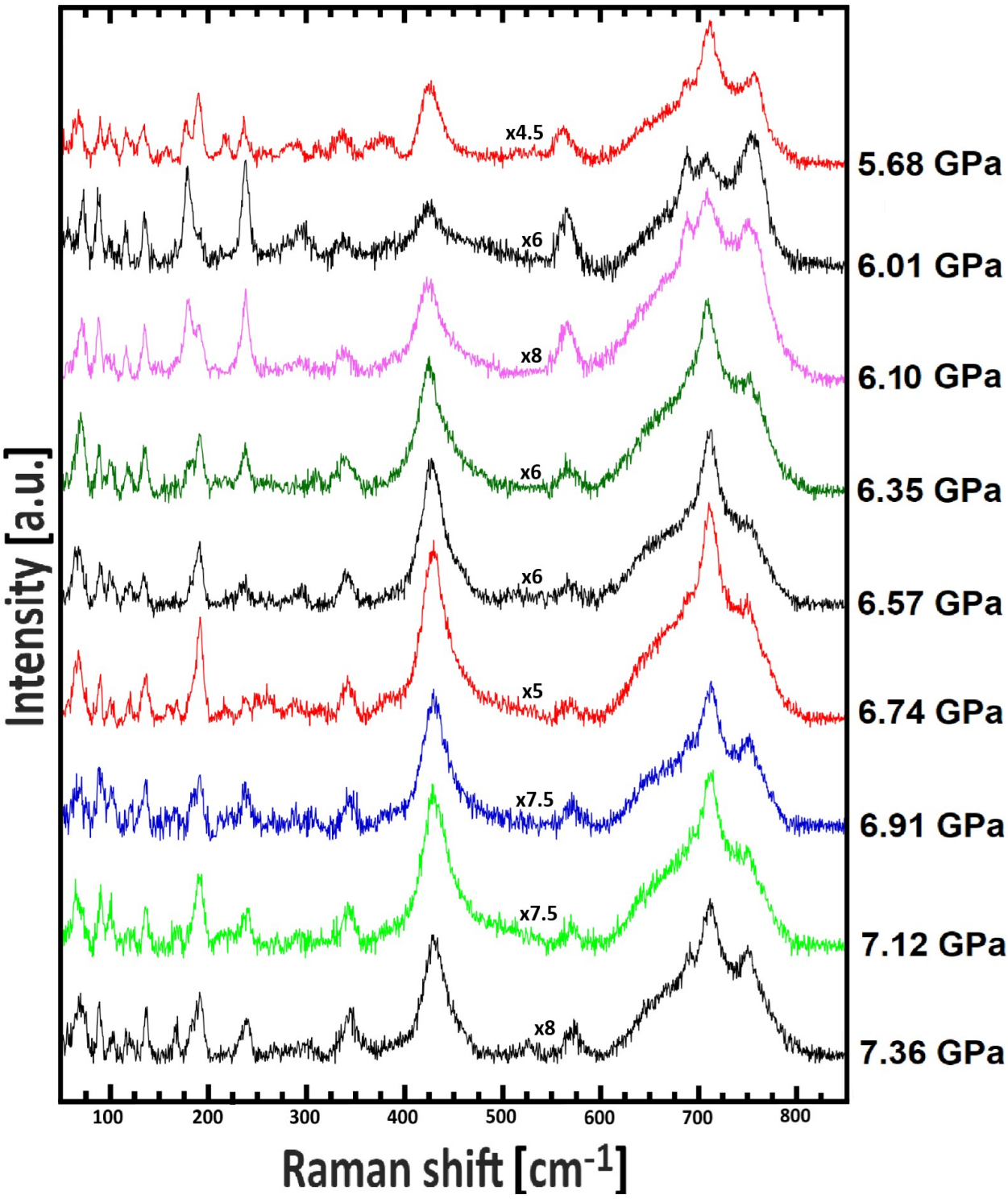

Figure 14: First part of the waterfall plot of the decompression series 1 following compression shown in Fig. 13. Start from bottom with 7.36 GPa and continua-tion onward to the top. Spectra which have been rescaled in the y-axis direction are marked with a multiplier on top. Vertical offset for easier visibility only.

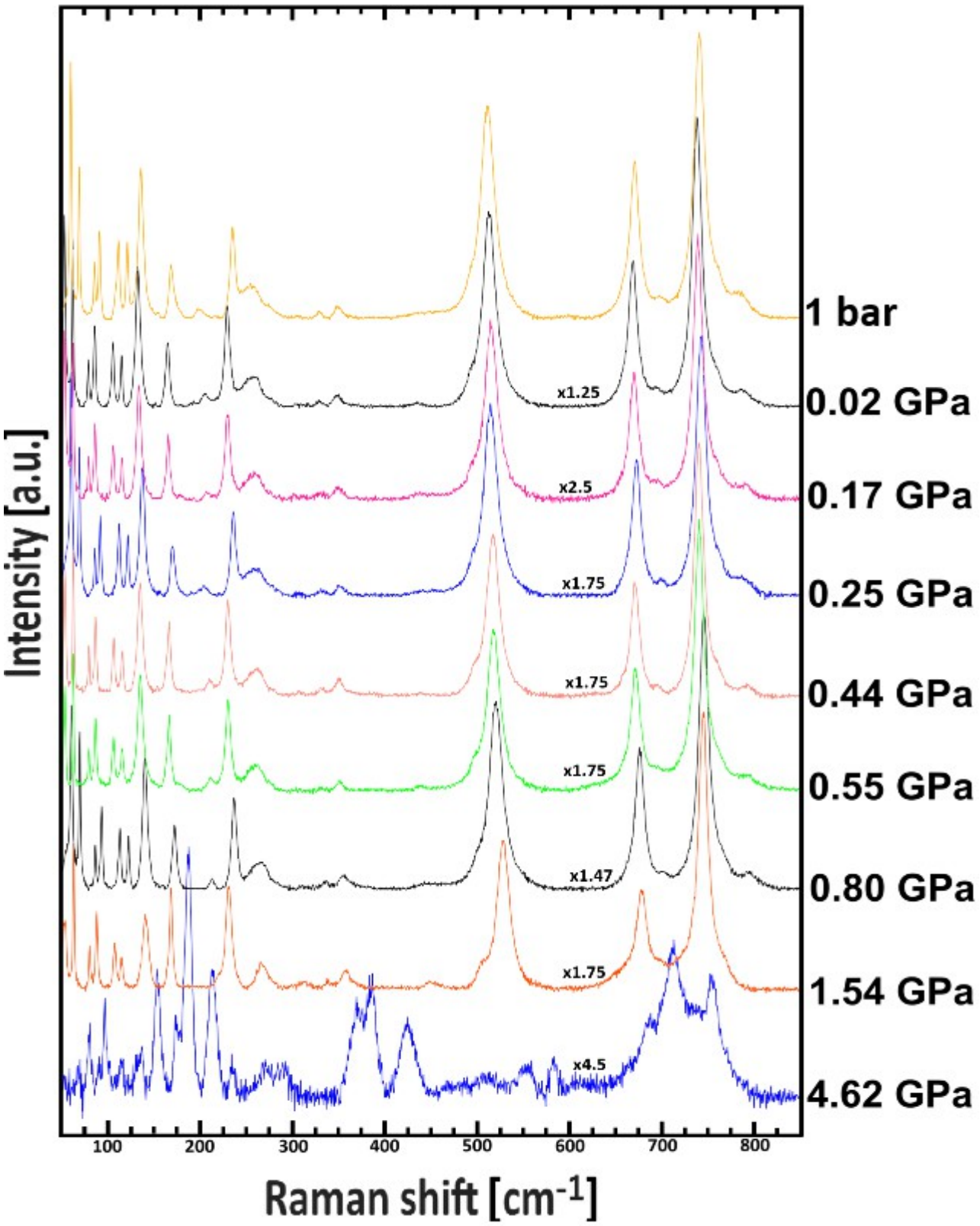

Figure 15: Second part of the waterfall plot of the decompression series 1 (continued from Fig. 14). Progression from bottom to top. Y-axis scaling multiplier for each spectrum can be seen on top. Vertical offset between spectra for visual purposes.

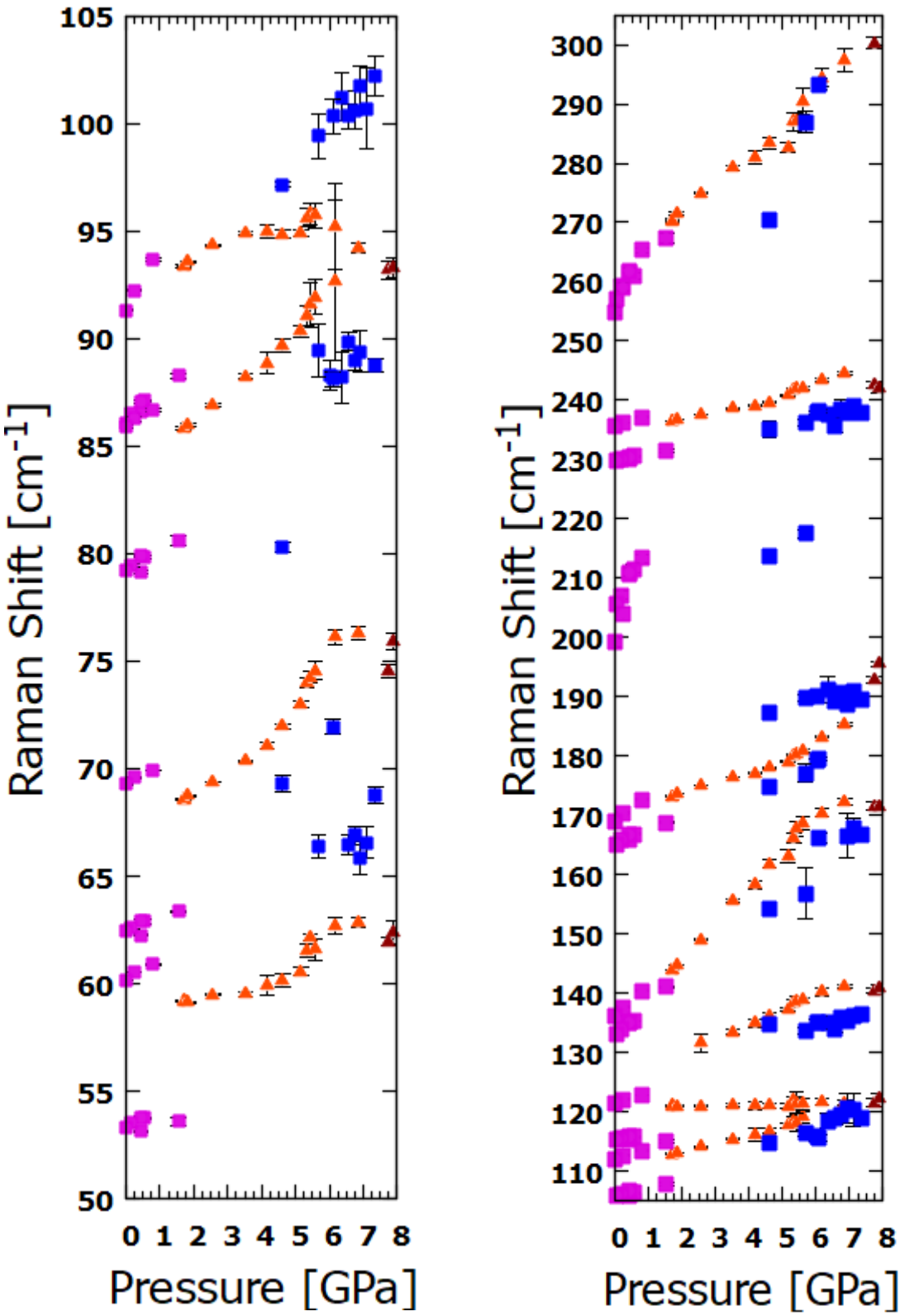

Figure 16: First Raman band position graph as a function of pressure for Raman measurement series s1. Error bars are displayed in black as whiskers and are only visible if the standard error is bigger than its correlated symbol. Triangles mark the compression series, where orange is the alpha phase and brown the beta phase. Blue squares show the beta phase of the decompression series, whereas purple squares display the alpha phase.

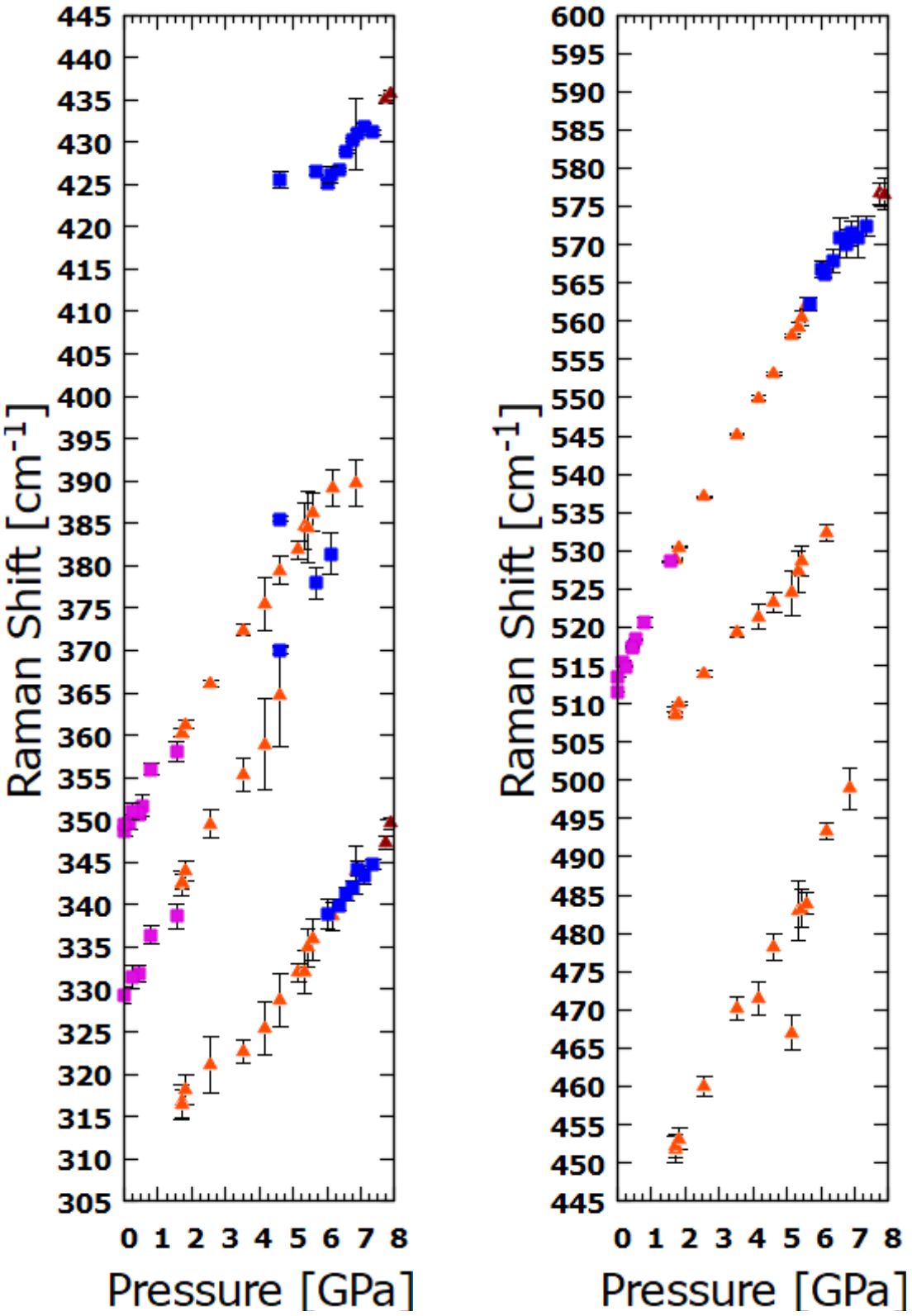

Figure 17: Second Raman band position graph as a function of pressure for Raman measurement series s1. Error bars are displayed in black as whiskers and are only visible if the standard error is bigger than its correlated symbol. Triangles mark the compression series, where orange is the alpha phase and brown the beta phase. Blue squares show the beta phase of the decompression series, whereas purple squares display the alpha phase.

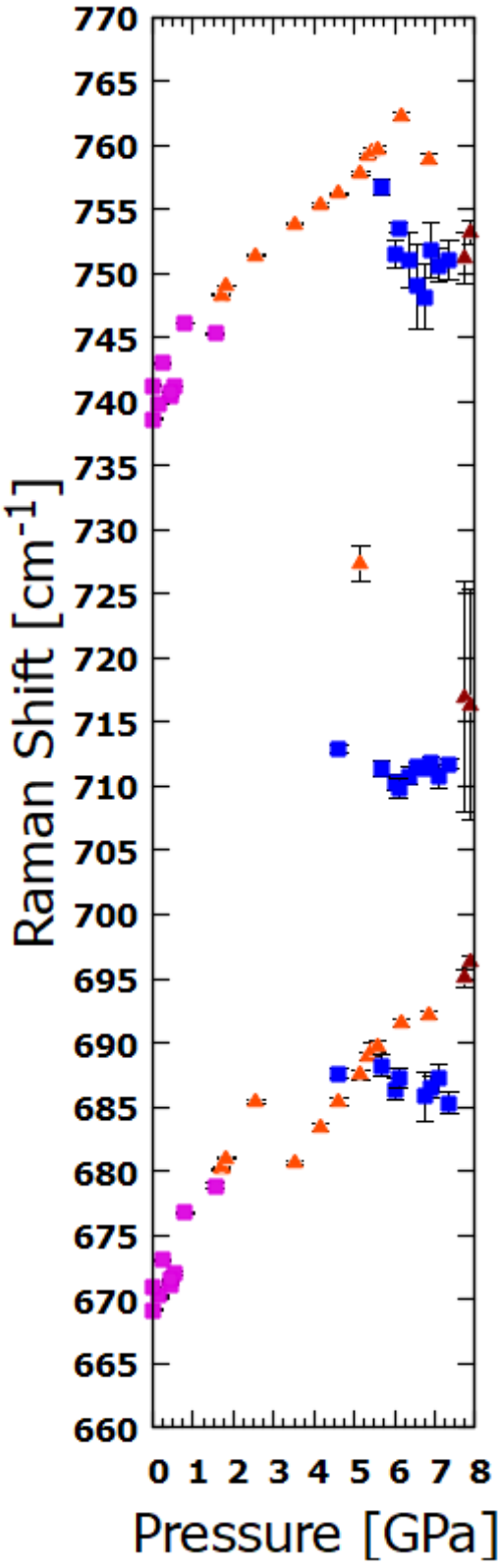

Figure 18: Third Raman band position graph as a function of pressure for Raman measurement series s1. Error bars are displayed in black as whiskers and are only visible if the standard error is bigger than its correlated symbol. Triangles mark the compression series, where orange is the alpha phase and brown the beta phase. Blue squares show the beta phase of the decompression series, whereas purple squares display the alpha phase.

An initially relatively weak Raman band, located in between 679 and 747 cm^{-1} (see Figure 18), undergoes a progressive intensity increase, eventually surpassing the relative intensity of adjacent Raman bands. For the decompression part of series 1 the filter setting was put down to 25%, to minimize additional marks (see Figure 5c) and provide more space to measure. Series 1 was proceeded by decompressing the sample in the range of 10 days. When the DAC reached 5.68 GPa the sample showed additional lamellae, about 45 degrees tilted relative to the ones noticed beforehand (see Figure 5d). As decompression continued the crystal seemingly showed present lamellae getting less visible at 1.54 GPa, displaying a rather check-like pattern in certain spots (see Figure 5e). After reaching ambient pressure conditions at 1 atm, the crystal was left by severe marks of laser damage. Apart from this fact, the sample hardly displays previously seen lamellae (see Figure 5f). Illustrated in Figure 14 and 15 Raman bands experience an expected redshift with decrease in pressure. At 1.54 GPa previously unresolved bands in the low energy region become discernible once again (see Figure 16). At 4.62 GPa Raman bands at 370 and 386 cm^{-1} (see Figure 17) appear as very dominant, exceeding the relative intensity of the Raman band at 425 cm^{-1}. Following further pressure decrease a subsequent pressure jump down to 1.54 GPa was noticed. This jump also comes with distinct differences in relative Intensity of observed Raman bands, being once again comparable to the initial Raman band profile of synthetic teineite at ambient conditions. The dominant band at initially 431 cm^{-1} becomes non-differentiable from the background and the Raman band at initially 712 cm^{-1} (see Figure 18) experiences substantial reduction in relative intensity.

High-Pressure Raman Measurement Series axr1

After loading the cell with a crystal of 110x83x40 µm in size (See Figure 6a) data collection was achieved by pressurizing the DAC up to 7.67 GPa over the course of 4 days. Reaching a pressure of 6.85 GPa inside the DAC, lamellae started to appear once again (see Figure 6b). Further increasing pressure to 7.30 GPa, additional domains were visible (see Figure 6c). Finally, being at 7.67 GPa other sets of lamellae appeared, tilted about 45° compared to the initial ones (see Figure 6d), creating an intricate pattern of domains. After using the sample at 7.67 GPa for SXRD measurement x-ray 1, the DAC was again decompressed over the course of 4 hours, measuring with already mentioned settings, using 15 sec. acquisition and 25% filter.

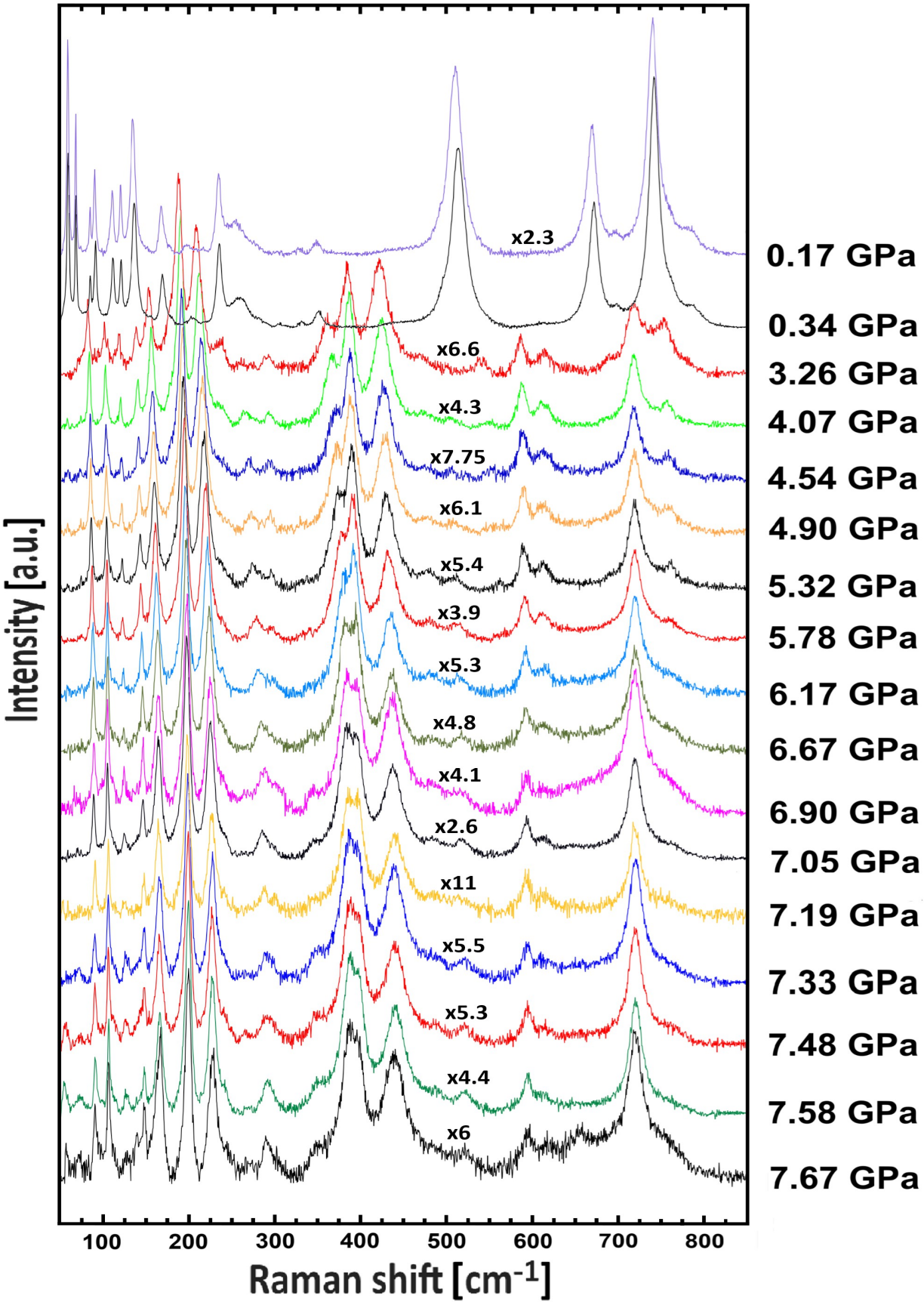

Figure 19: Waterfall plot of obtained spectra for Raman measurement series axr1. Progression from bottom to top. Multiplying factor for rescaled spectra in y-axis direction is displayed on top. Vertical offset for visibility purposes only.

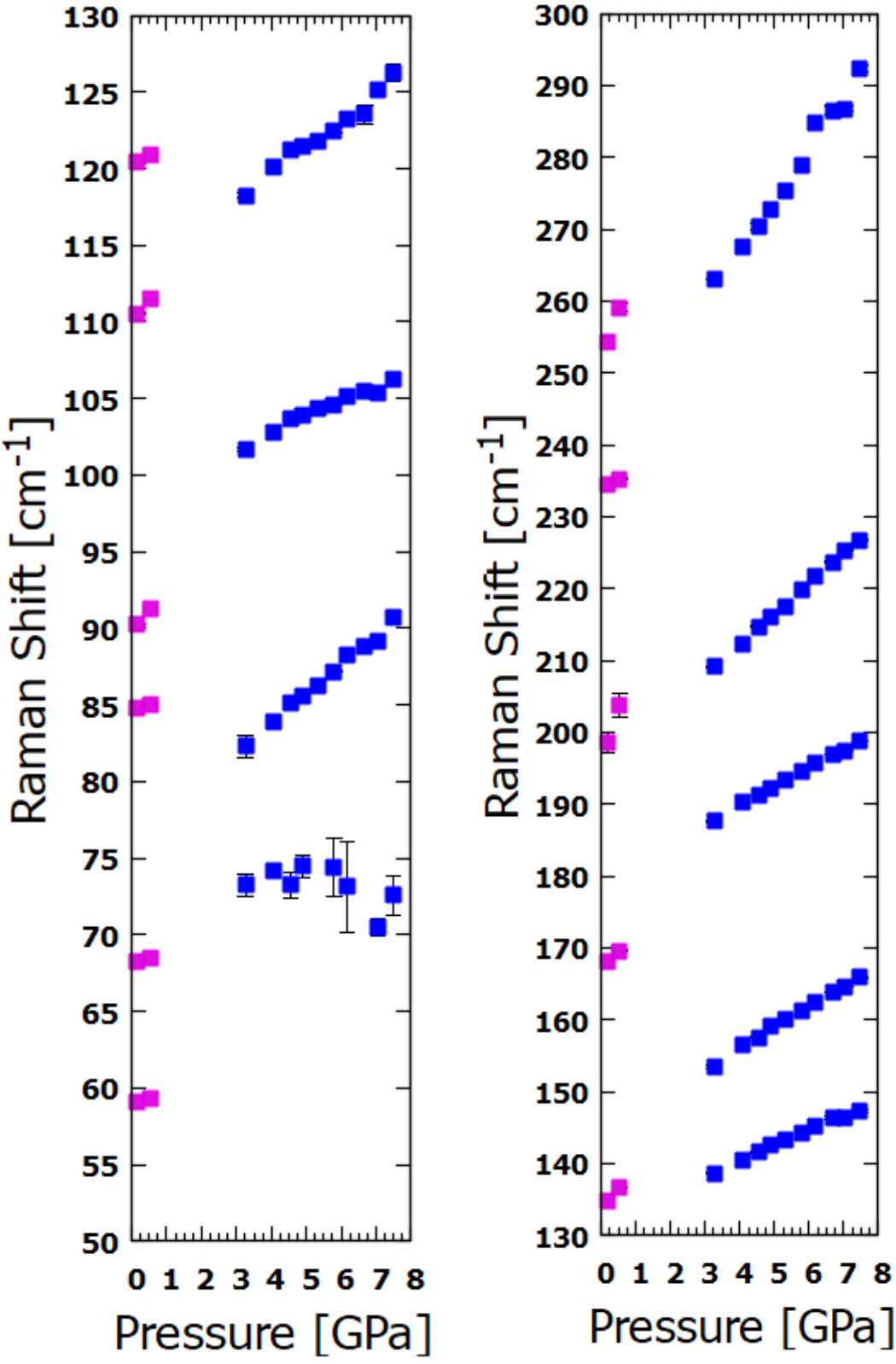

Figure 20: First Raman band position graph as a function of pressure for Raman measurement series axr1. Error bars are displayed in black as whiskers and are only visible if the standard error is bigger than its correlated symbol. Triangles mark the compression series, where orange is the alpha phase and brown the beta phase. Blue squares show the beta phase of the decompression series, whereas purple squares display the alpha phase.

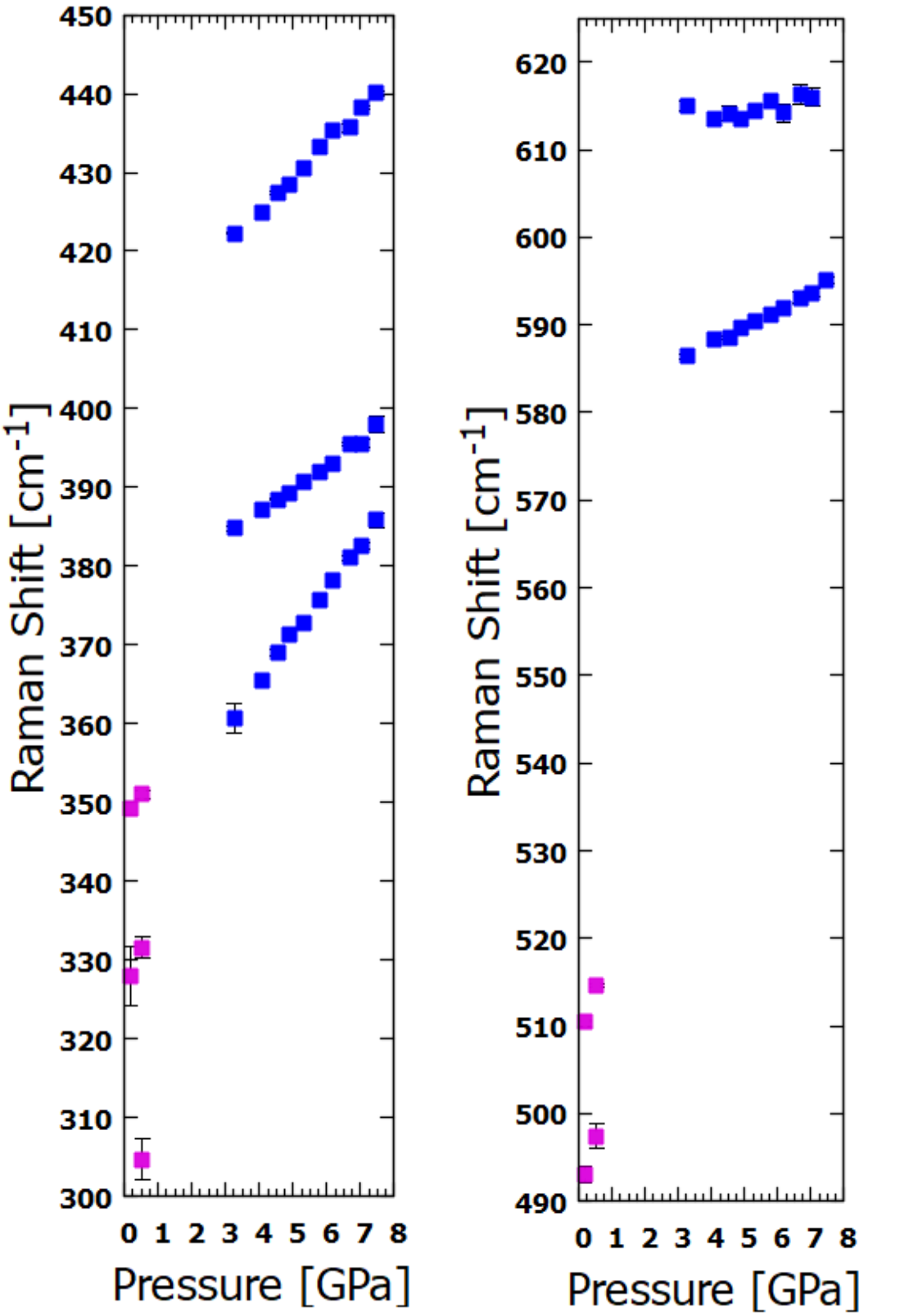

Figure 21: Second Raman band position graph as a function of pressure for Raman measurement series axr1. Error bars are displayed in black as whiskers and are only visible if the standard error is bigger than its correlated symbol. Triangles mark the compression series, where orange is the alpha phase and brown the beta phase. Blue squares show the beta phase of the decompression series, whereas purple squares display the alpha phase.

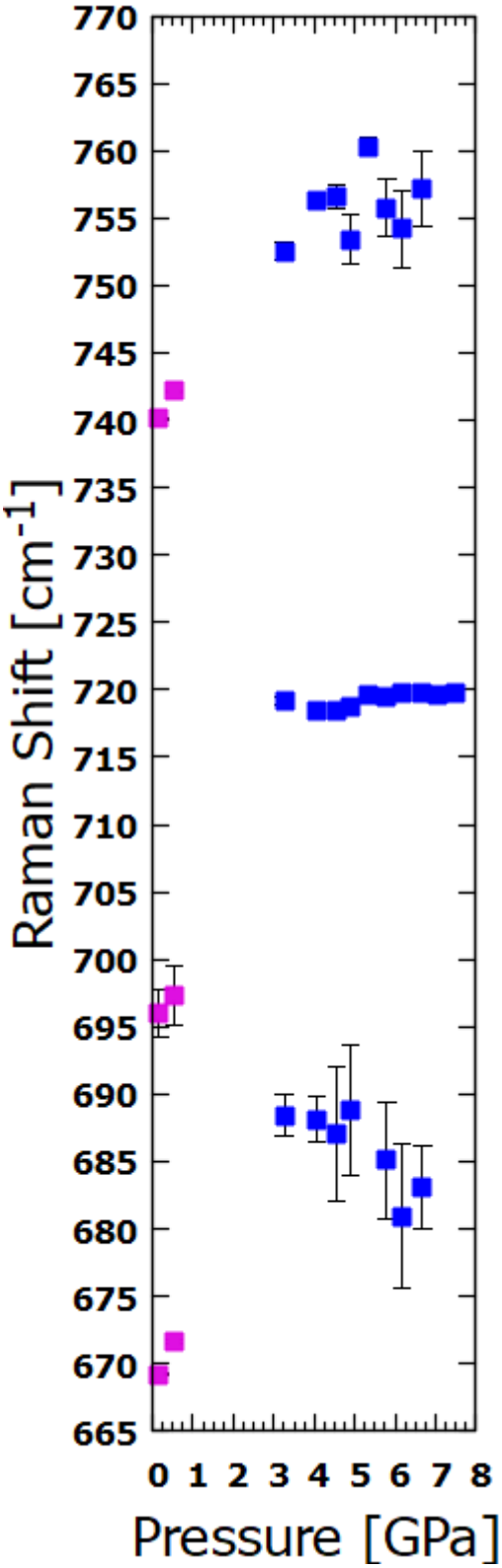

Figure 22: Third Raman band position graph as a function of pressure for Raman measurement series axr1. Error bars are displayed in black as whiskers and are only visible if the standard error is bigger than its correlated symbol. Triangles mark the compression series, where orange is the alpha phase and brown the beta phase. Blue squares show the beta phase of the decompression series, whereas purple squares display the alpha phase.

At 7.67 GPa the measured Raman band profile is very distinct from the one already known at ambient conditions, as Raman bands displayed at ~440, 720 and 391 cm^{-1} appear very dominant (see Figure 19), of which the latter turns out to be actually two converged Raman bands. Upon further decompression of the diamond anvil cell, Raman bands in the low energy region experienced a trend of divergence (see Figure 20), as well as the Raman bands at around 385 and 398 cm^{-1}, visible at 7.58 GPa (see Figure 21). This is observed alongside the general decrease in intensity, e.g. displayed for the Raman band initially at around 720 cm^{-1}, which remains easily trackable in comparison to adjacent Raman bands (see Figure 22). After advancing decompression of the DAC beyond 3.26 GPa a strong jump in pressure is notable to 0.34 GPa. As a result, Raman bands experienced a strong redshift, causing a drastic change in the Raman band profile. This sudden change is marked by the newly visible dominance of Raman bands at 515, 671 and 742 cm^{-1}, as well as the disappearance of previously strong Raman bands at initially 720, 440 and 391 cm^{-1}.

High-Pressure Raman Measurement Series s2

Measurement series 2 was conducted by loading DAC012 (see Table 1) with a synthetic teineite crystal of 130x90x40 µm in size, using Labspec6 with the same settings as in measurement series axr1. After the initial loading procedure, the cell was compressed up to 7.84 GPa over the course of 4 hours. Starting off at the initial pressure of 1.03 GPa after loading (see Figure 7a) lamellae began to show once again at 7.14 GPa (see Figure 7b) and 7.84 GPa (see Figure 7c). With advancing compression all Raman bands experienced a softening regarding their intensity aside the expected blueshift (see Figure 23). Still, most of the initially observed Raman bands remain easily trackable throughout compression. Raman bands in the low energy region at 84 and 89 cm^{-1}, as well as ~110 and 119 cm^{-1} show a trend of convergence upon pressure increase (see Figure 25). As Raman modes in the mid energy region remain relatively unchanged in terms of intensity and Raman band positions, Raman modes in the high energy region at initially 509 cm^{-1}, 668 and 739 cm^{-1} still remain dominant (see Figure 26), while the Raman band between the last two mentioned bands gains relative intensity, yet still remaining hardly traceable.

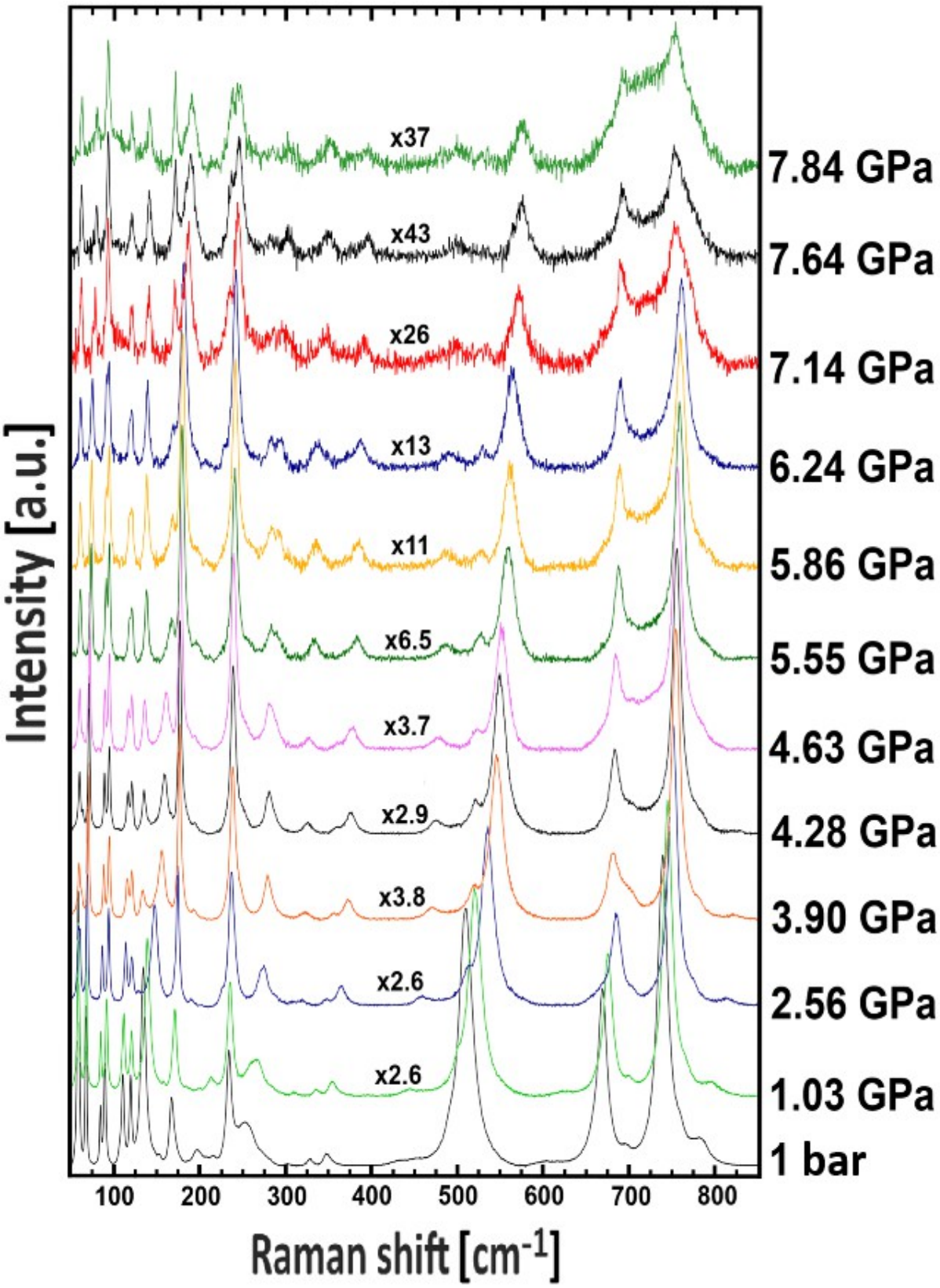

Figure 23: Waterfall plot of attained Raman spectra from compression series s2. Progression from bottom to top. Vertical offset is for visibility only. Spectra that have been rescaled in the y-axis direction for visibility purposes are marked with a multiplicator on top inside the graph.

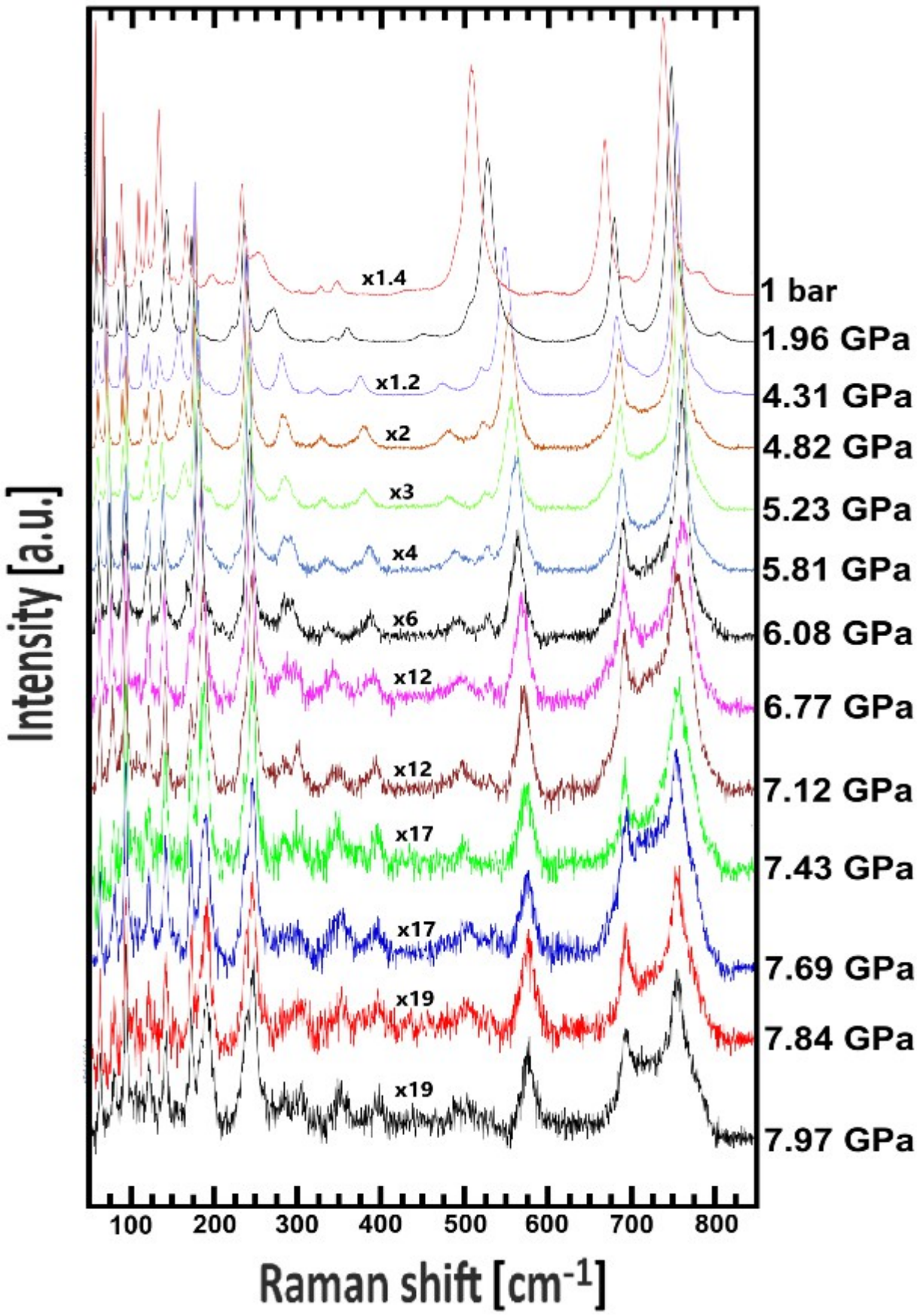

Figure 24: Waterfall plot of attained Raman spectra from decompression series s2 following compression shown in Fig. 23. Progression from bottom to top. Vertical offset is for visibility only. Spectra that have been rescaled in the y-axis direction for visibility purposes are marked with a multiplicator on top inside the graph.

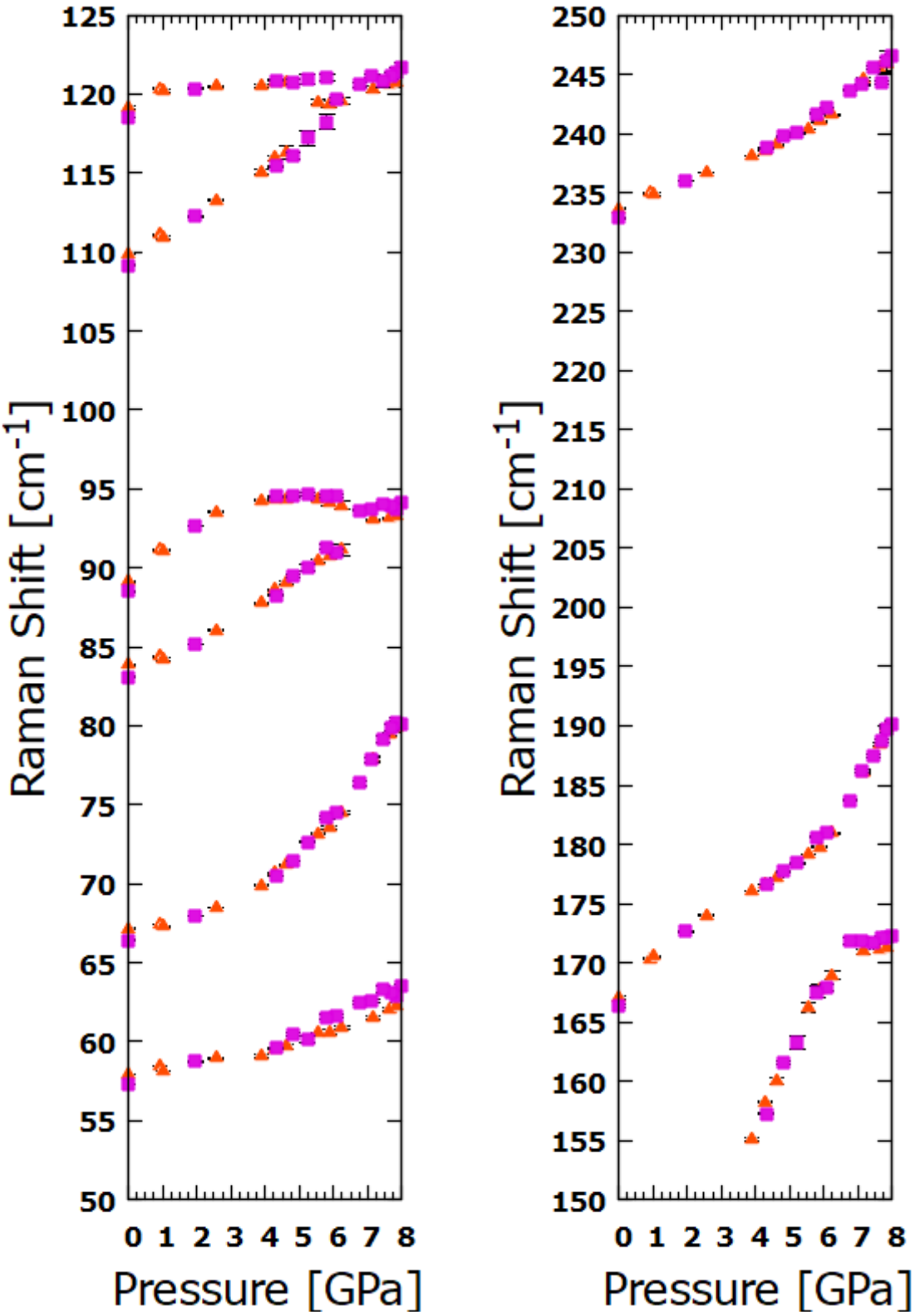

Figure 25: First Raman peak shift graph of measurement series s2. Orange triangles refer to data from the compression series, whereas registered Raman bands during decompression are marked as purple triangles. Error bars are marked for each data point, if not visible, the error is smaller than the data point symbol.

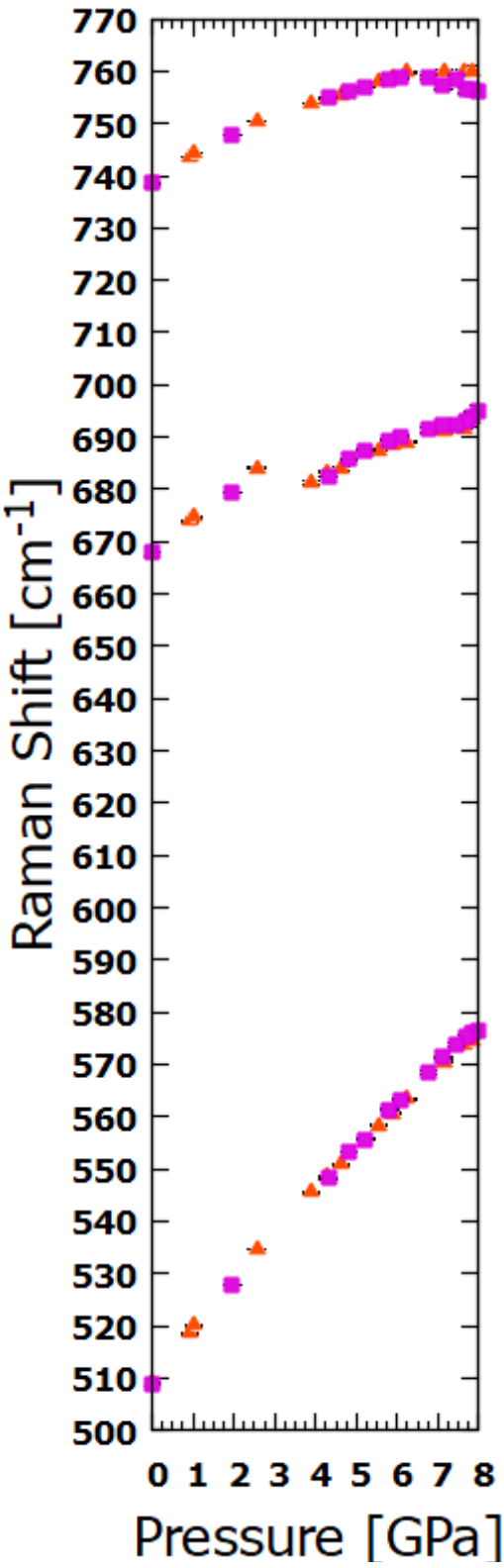

Figure 26: Second Raman peak shift graph of measurement series s2. Orange triangles refer to data from the compression series, whereas registered Raman bands during decompression are marked as purple triangles. Error bars are marked for each data point, if not visible, the error is smaller than the data point symbol.

At 7.84 GPa the DAC was decompressed in 3 1/2 hours, 17 days after the last compression measurement. The crystal showed severe damage through laser irradiation, but also a seemingly partial reversal of its innermost lamellae at 1.96 GPa (see Figure 7d). Following decompression after reaching 7.97 GPa (Figure 24) Raman bands in the high energy region at 576, 695 and 756 cm^{-1} gain intensity compared to other bands, while the band assumed at 726 cm^{-1} experiences a relative decrease in intensity. In the mid energy region Raman bands remain relatively low in intensity. Raman band pairs in the low energy region, which previously displayed convergence with increase in pressure, are separating once again, first visible at 6.08 GPa for bands at 91 and 95 cm^{-1}, as well as at 5.81 GPa for bands at around 118 and 121 cm^{-1}.

3.3 Single Crystal X-ray Diffraction

For SXRD four measurements were conducted, x-ray ambient at 1 bar, x-ray 1 at 7.67 GPa, x-ray 2 at 7.72 GPa and x-ray 3 at 7.52 GPa. For further information regarding data refer to Table 2, 3 and 4.

X-ray Ambient

At first, a crystal of 110x120x40 µm in size was measured at ambient conditions on the STOE StadiVari with the described instrumental setup in chapter 2.5. After data integration and refinement of the structure (see Figure 28) hydrogen atom positions were located, adding onto the work of Effenberger (1977).

X-ray 1

This high-pressure measurement was conducted with the same crystal as in axr1 (see Figure 6a-d) with the STOE StadiVari at the IfMK, demonstrating a complex pattern of domains, caused by the application of pressure. Due to this phenomenon, lattice parameters were not attainable, as multiple orientations were measured at once (see Figure 27), making the collected data too unreliable for further integration and refinement.

X-ray 2

HP-SXRD measurement x-ray 2 was done again by using the STOE Stadivari at the IfmK, measuring a crystal of 61x77x40 µm in size (see Figure 8a) after compressing the sample in a timeframe of 21 days with a mediate pressure increase rate of 1.149 x 10^{-2} GPa/h.

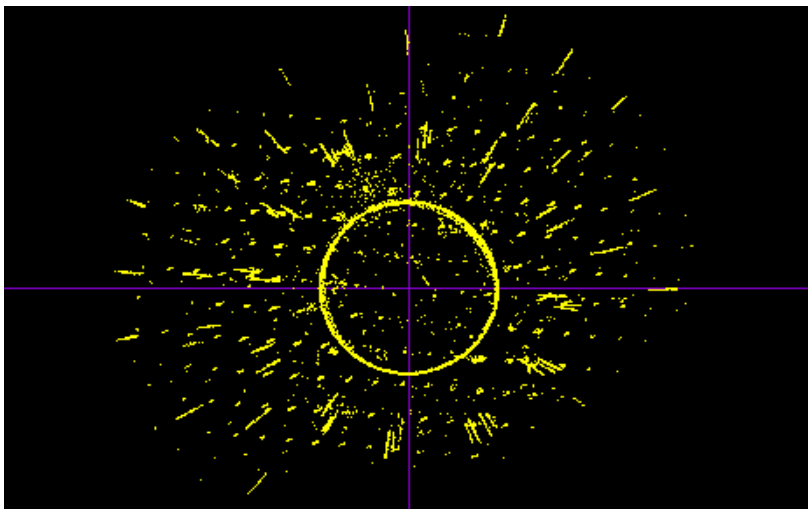

Figure 27: Collected reflections of x-ray 1 from STOE StadiVari in X-Area.

After the pressure inside the DAC reached 7.37 GPa, no further building of domains were visible, next to bubbles close to the crystal (see Figure 8b and c), first assumed to be a result of dehydration, which later on turned out to be an effect of H_2O contamination inside the cell, caused during the process of M-E 4:1 injection into the DAC. At maximum pressure of 7.72 GPa integration of the collected data and further refinement lead to the resulting structure (see Figure 29) using the experimental scaling approach. Due to high redundancy in data, hydrogen atom positions were hardly assignable and therefore not displayed in the structure for x-ray 2.

Table 2. Single-crystal X-ray data (SXRD) and structure refinements of ($CuTeO_3 \cdot 2H_2O$ (mineral name teineite)), space group $P2_12_12_1$.

Formula	**ambient conditions**	**DAC (7.52 GPa)**	**DAC (7.72 GPa)**
Diffractometer	Stoe StadiVari	Xpress BL	Stoe StadiVari
a [Å]	6.6394(11)	5.4424(3)	5.4466(11)
b [Å]	9.6200(14)	10.1941(16)	10.2632(14)
c [Å]	7.4417(2)	6.7748(10)	6.776(2)
V [Å^3]	475.31	375.88	378.78
Z	4	4	4
D_{calc} [g cm^{-3}]	3.86	4.86	4.56
Absorption coefficient [mm^{-1}]	10.572	13.2	5.042
λ [Å] [a]	0.71073	0.4956	0.71073
D [mm] [b]	60	249.9	60
2Θmin/2Θmax	3.0/83.65	3.348/47.28	3.0/65.43
Measured reflections	31838	648	5421
Unique reflections (n)	3237	330	251
$R_{int} = \Sigma F_o^2 - F_o^2(mean)/\Sigma F_o^2$	0.0311	0.0219	0.048

[a] wavelength of used X-ray beam for experiments
[b] detector-to-sample distance

Table 2. Cont.

Formula	ambient conditions	DAC (7.52 GPa)	DAC (7.72 GPa)
Extinction parameter k $F_c^* = F_c \cdot k[1+0.001 \cdot F_c^2 \lambda^3/\sin(2\Theta)]^{-1/4}$	0.0108(6)	0.024(7)	0.0012(11)
$R1 = \Sigma(F_o - F_c) / \Sigma F_o$	0.0138 / 0.0145	0.0313 / 0.0327	0.0138 / 0.0145
$wR2 = [\Sigma w(F_o^2 - F_c^2)^2 / \Sigma w F_o^4]^{1/2}$	0.0316	0.081	0.053
GooF = $\{\Sigma[w(F_o^2 - F_c^2)^2] / (n-p)\}^{0.5}$	1.11	1.15	1.26
Number of variable parameters (p)	82	39	45
max Δ/σ	< 0.001	< 0.001	< 0.001
Final difference Fourier map [eÅ^{-3}]	-0.83 to +1.40	-0.87 to +0.67	-0.52 to +0.40

X-ray 3

HP-SXRD measurements for x-ray 3 were conducted at the Elettra Sincrotrone Trieste (Lotti, et al., 2020) with the same sample as in x-ray 2, with a time gap of 24 days between x-ray 2 and this measurement, resulting in the proposed crystal structure visible in Figure 30. As in x-ray 2, the structure model is displayed without any hydrogen atoms, due to the lack of sufficient data.

Table 3. Fractional atomic coordinates and displacement parameters of $CuTeO_3 \cdot 2H_2O$. All atoms are at the Wyckoff position 4(*a*) and have point symmetry 1. The anisotropic displacement parameters are defined as: $\exp[-2\pi^2 \Sigma^3_{i=1} \Sigma^3_{j=1} U_{ij} a_i a_j h_i h_j]$.

(a) Atomic coordinates and equivalent respectively isotropic displacement parameters

Refinement at ambient conditions				
Atom	x	y	z	U_{equiv} / U_{iso}
Cu	0.53082(3)	0.15615(2)	0.20136(3)	0.01103(5)
Te	0.71051(2)	0.38924(2)	0.47389(2)	0.00960(4)
O1	0.24427(19)	0.21528(14)	0.73667(17)	0.0150(2)
O2	0.98093(17)	0.38160(15)	0.54440(15)	0.01438(18)
O3	0.2773(2)	0.06457(12)	0.13645(17)	0.01359(17)
O4	0.0657(2)	0.28856(16)	0.05479(17)	0.0169(2)
O5	0.2907(3)	0.44630(19)	0.3268(2)	0.0239(3)
H41	-0.041(10)	0.283(6)	0.125(8)	0.053(15)
H42	0.131(7)	0.205(4)	0.082(6)	0.032(10)
H51	0.232(9)	0.392(6)	0.218(10)	0.067(17)
H52	0.171(14)	0.427(8)	0.407(12)	0.10(2)

Table 3. (a) Cont.

Refinement at 7.52 GPa (x-ray 3)				
Atom	x	y	z	U_{equiv} / U_{iso}
Cu	0.3073(2)	0.3424(7)	0.8210(2)	0.0162(4)
Te	0.23084(13)	0.1103(3)	0.51843(11)	0.0143(19)
O1	0.1837(13)	0.170(4)	0.7789(13)	0.0136(16)
O2	0.3956(14)	0.325(3)	0.5437(13)	0.0153(16)
O3	0.4246(17)	0.511(3)	0.8567(13)	0.021(2)
O4	0.2472(14)	0.309(3)	0.1046(13)	0.0160(17)
O5	0.4053(16)	0.054(4)	0.1044(15)	0.0223(19)
Refinement at 7.72 GPa (x-ray 2)				
Atom	x	y	z	U_{equiv} / U_{iso}
Cu	0.3075(3)	0.3440(12)	0.8213(2)	0.022(6)
Te	0.23068(17)	0.1101(5)	0.51829(10)	0.016(3)
O1	0.1857(18)	0.166(6)	0.7815(13)	0.010(2)
O2	0.3974(18)	0.338(5)	0.5437(12)	0.012(2)
O3	0.425(2)	0.519(4)	0.8544(15)	0.014(3)
O4	0.249(2)	0.309(4)	0.1051(13)	0.012(2)
O5	0.405(2)	0.064(5)	0.1000(14)	0.019(3)

(b) Anisotropic displacement parameters

Atom	U^{11}	U^{22}	U^{33}	U^{23}	U^{13}	U^{12}
Refinement at ambient conditions						
Cu	0.01108(6)	0.01280(6)	0.00920(5)	-0.00047(5)	-0.00004(4)	-0.00318(5)
Te	0.00960(3)	0.01129(3)	0.00799(3)	-0.00006(2)	0.00038(2)	-0.00032(2)
O1	0.0149(4)	0.0189(4)	0.0119(4)	-0.0057(3)	-0.0033(3)	0.0063(3)
O2	0.0111(3)	0.022184)	0.0104(3)	0.0019(3)	-0.0015(3)	0.0021(3)
O3	0.0123(4)	0.0116(3)	0.0179(4)	-0.0021(3)	-0.0027(3)	-0.0011(3)
O4	0.0179(5)	0.0210(5)	0.0124(4)	0.0027(3)	0.0029(3)	0.0062(4)
O5	0.0195(5)	0.0323(6)	0.0214(5)	-0.0007(5)	0.0029(5)	-0.0090(5)
Refinement at 7.52 GPa (x-ray 3)						
Te	0.0154(3)	0.016(6)	0.0110(4)	0.0003(7)	0.0000(2)	0.0011(6)
Refinement at 7.72 GPa (x-ray 2)						
Cu	0.0179(12)	0.037(2)	0.0105(6)	0.000(2)	0.0014(6)	-0.003(3)
Te	0.0138(5)	0.026(10)	0.0088(4)	0.0001(12)	0.0004(3)	0.0015(16)

Table 4. Comparative table of structure parameters for conducted SXRD experiments of synthetic teineite including bond lengths of associated coordination polyhedra and bond angles. Corner sharing oxygen angles and distortion index are derived from VESTA (Momma and Izumi, 2011).

	ambient conditions	**7.52 GPa (x-ray 3)**	**7.72 GPa (x-ray 2)**
bond lengths [Å]			
Cu-O1	1.9350(12)	1.90(4)	1.96(5)
Cu-O2	1.9532(11)	1.948(10)	1.945(9)
Cu-O3	1.9585(13)	1.85(3)	1.92(4)
Cu-O4	1.9911(13)	1.978(11)	1.983(11)
Cu-O5	2.3480(17)	2.48(2)	2.45(2)
Te-O1	1.8704(12)	1.884(14)	1.89(2)
Te-O2	1.8737(12)	1.987(13)	1.939(16)
Te-O3	1.8761(12)	-	-
Te-O5	-	1.92(4)	2.01(4)
Te-O2*	3.0205(13)	2.37(3)	2.51(4)
Te-O3*	2.9677(14)	2.292(18)	2.27(2)
Te-O5*	3.0423(18)	3.016(12)	3.028(12)
bond angles [°]			
O1-Cu-O2	90.673(9)	81.7(10)	85.5(13)
O1-Cu-O5	101.717(12)	96.4(9)	95.1(13)
O2-Cu-O5	90.787(5)	117.0(5)	116.7(7)
O3-Cu-O2	90.579(9)	97.3(10)	93.5(14)
O3-Cu-O4	89.050(8)	95.2(9)	96.4(11)
O3-Cu-O5	91.405(11)	83.3(9)	84.8(13)
O3-Cu-O1	166.7985(11)	178.7(7)	178.8(6)
O4-Cu-O1	88.415(9)	85.9(10)	84.8(11)
O4-Cu-O5	94.858(6)	74.3(6)	73.4(7)
O4-Cu-O2	174.3505(16)	164.0(14)	166.6(18)
O1-Te-O2	95.663(8)	88.0(5)	90.0(6)
O1-Te-O3	96.336(16)	84.7(7)	82.7(9)
O2-Te-O3	96.699(4)	94.0(9)	93.3(10)
corner sharing oxygen angles [°] [a]			
Cu-O2-Te	116.206(2)	112.98(3)	111.561(3)
Cu-O1-Te	117.059(6)	113.565(11)	115.8515(10)
Cu-O3-Te	118.268(6)	137.698(5)	134.8(14)
distortion index (bond length) [b]			
$Cu^{[4+1]}$	0.06055	0.08810	0.07678
$Te^{[3]}$	0.00105	0.01894	0.02139
$Te^{[3+3]}$ *	0.23267	0.13946	0.14548

[a] angles of shared oxygen atoms between two connected coordination polyhedra of Cu and Te.
[b] sum of deviations from the average bond length between anion and cation (after Baur, 1974).
* bond lengths of additional oxygen atoms when creating a $Te^{[3+3]}$ coordination polyhedron.

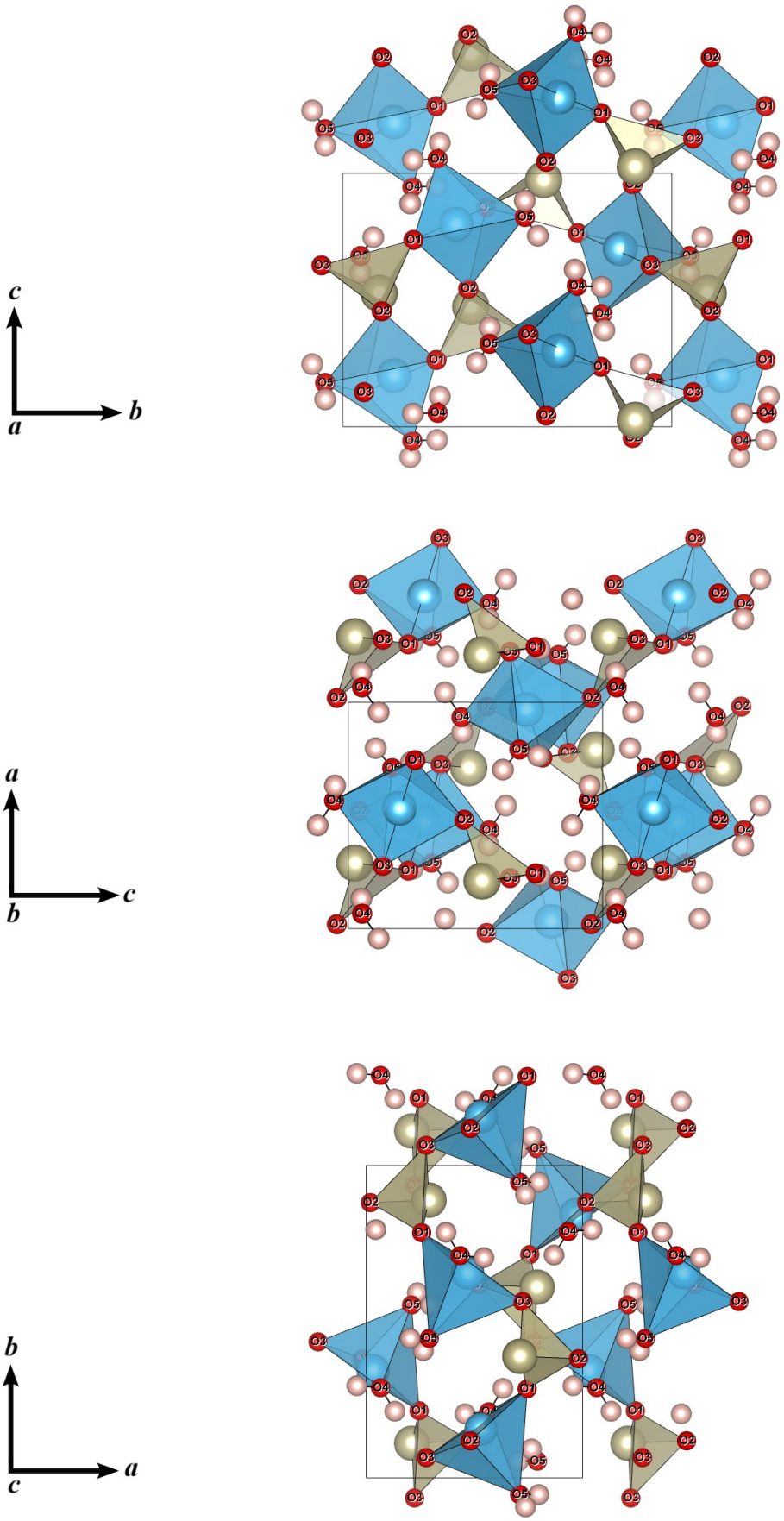

Figure 28: Different projections of the structure model from STOE StadiVari for synthetic teineite at 1 bar. Graphics derived from VESTA. H atoms are pink-white, Cu atoms are blue, Te in beige-grey and oxygen atoms are marked in red.

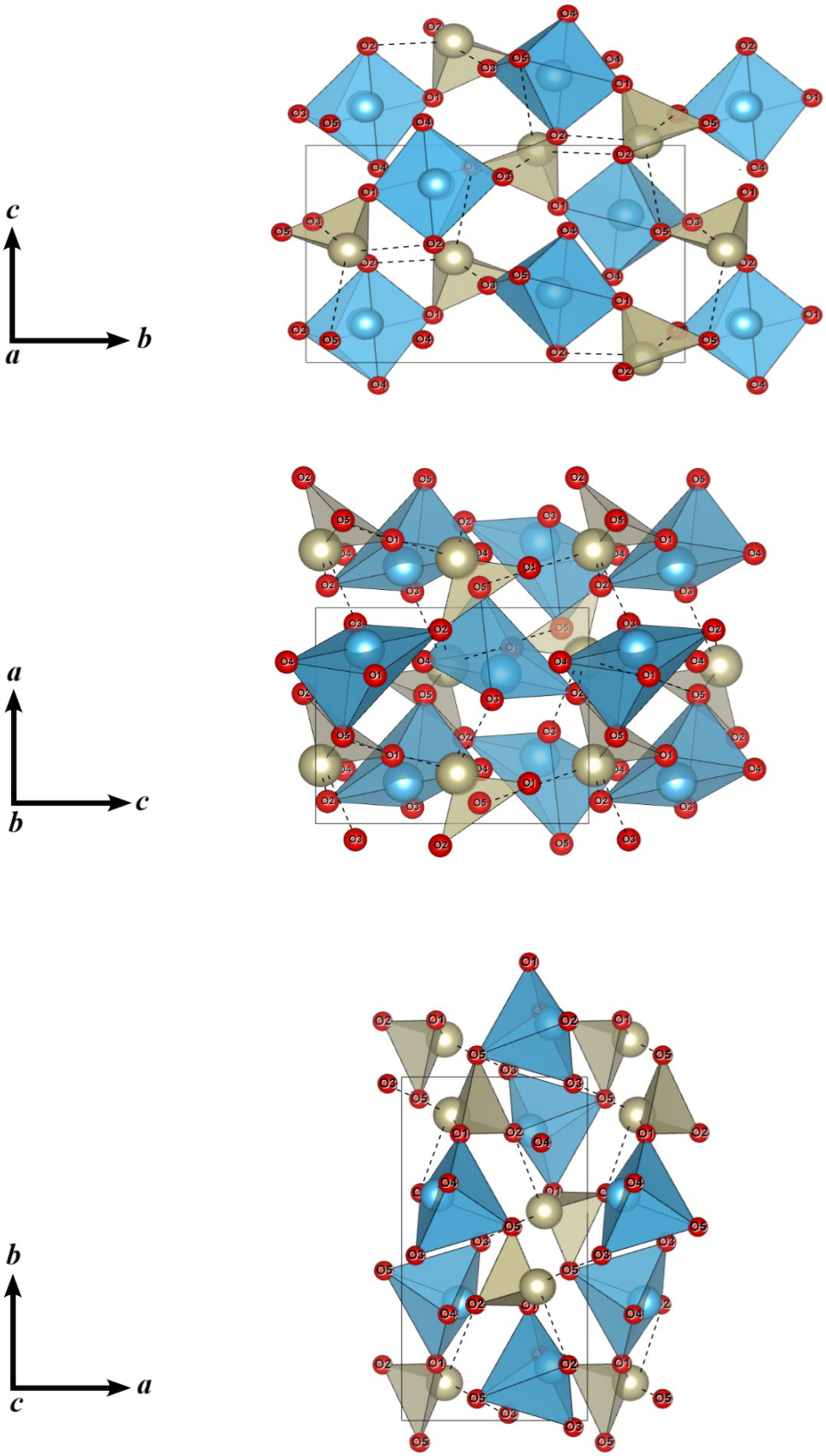

Figure 29: Different projections of the structure model from STOE StadiVari for synthetic teineite at 7.72 GPa. Graphics derived from VESTA. Cu is represented in blue, Te in beige-grey and oxygen atoms are marked in red. Dashed lines represent bonds of additionally coordinated oxygen atoms per Te, resulting in a $Te^{[3+3]}$ coordination polyhedron.

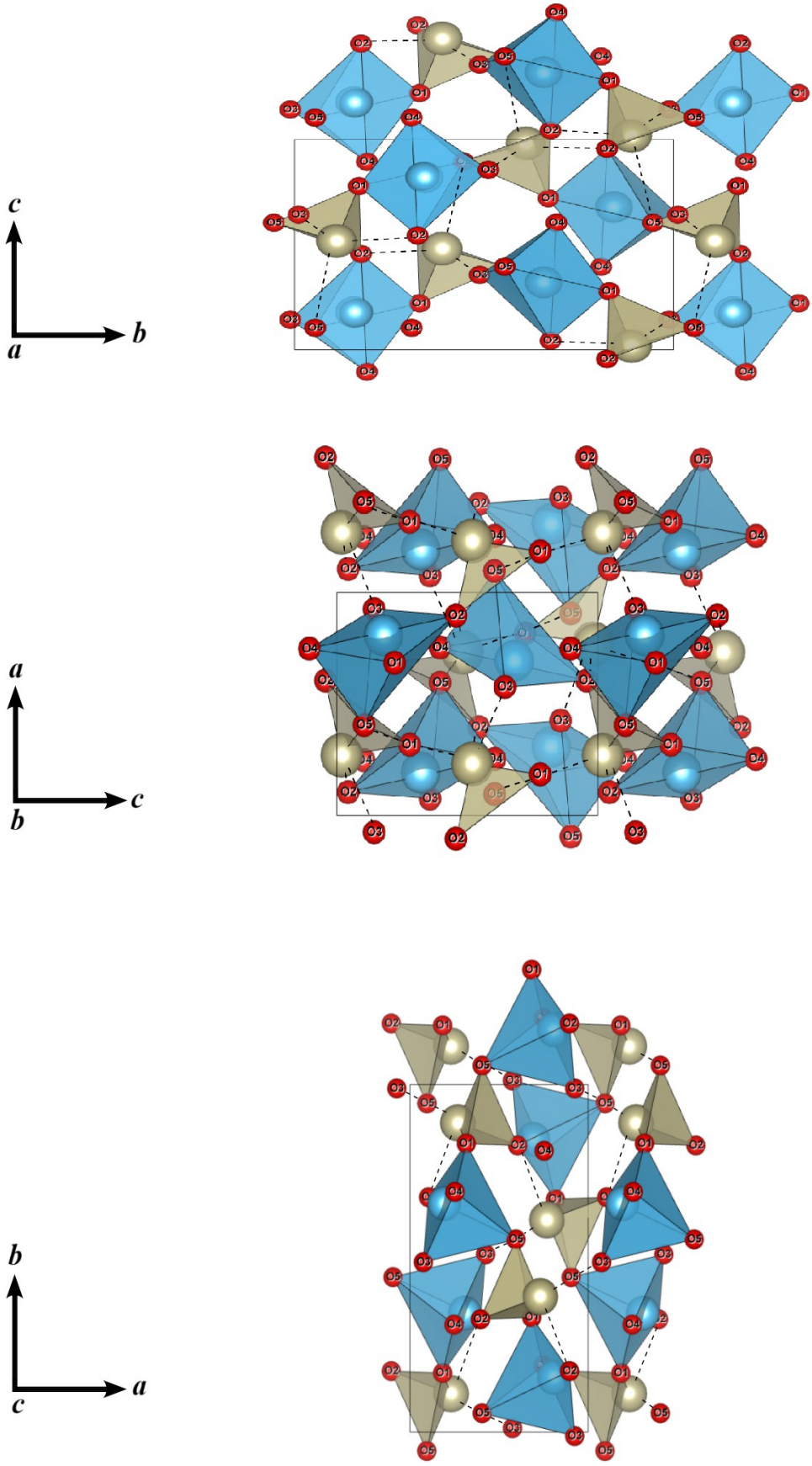

Figure 30: Different projections of the structure model from Xpress beamline (Elettra Sincrotrone Trieste) for synthetic teineite at 7.52 GPa. Graphics derived from VESTA. Cu is represented in blue, Te in beige-grey and oxygen atoms are marked in red. Dashed lines represent bonds of additionally coordinated oxygen atoms per Te, resulting in a $Te^{[3+3]}$ coordination polyhedron.

4. Discussion

Raman Spectroscopy

The Raman spectrum of teineite at ambient pressure (see Figure 31) exhibits a broad range of vibrational modes, extending from approximately 50 to 800 cm^{-1}. The low wavenumber region between 50-270 cm^{-1} is tentatively assigned to external vibrations, as literature on this specific spectral range for teineite is limited. Based on the vibrational mode assignments for $(TeO_3)^{2-}$ proposed by Frost and Keeffe (2009), the bands observed at 741 and 782 cm^{-1} can be attributed to the v_1 (A_1) symmetric stretching mode and registered bands at 670 and 697 cm^{-1} to v_3(E) antisymmetric stretching. The v_2(A_1) bending mode is likely associated with the Raman bands at 350 and 330 cm^{-1}, with a possible contributing band at 304 cm^{-1}. Raman bands observed at 390 and 455 cm^{-1} can be assigned to the v_4(E) bending mode. The characteristic H_2O librational mode is designated to the Raman band at 511 cm^{-1}, accompanied by a left shoulder at 503 cm^{-1}.

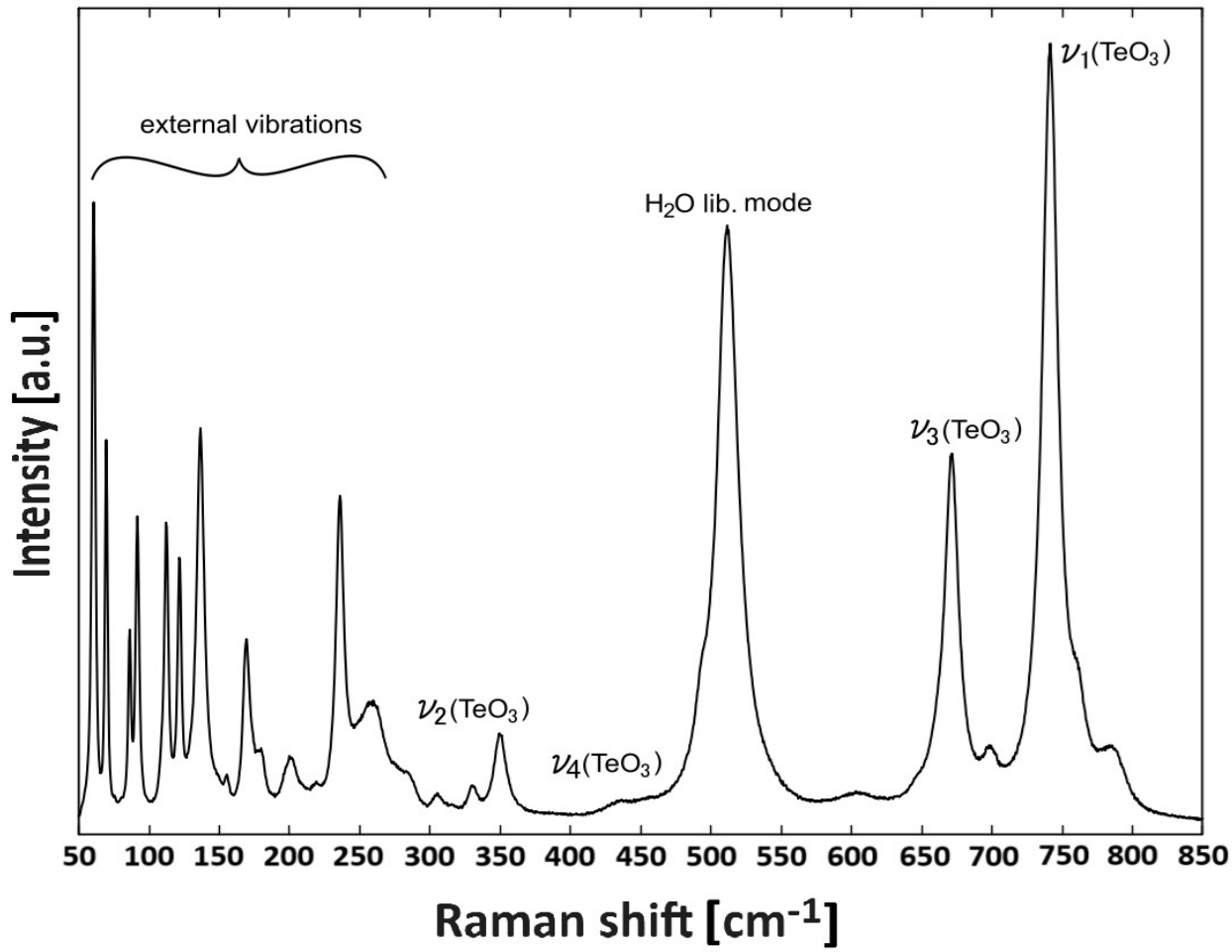

Figure 31: Raman profile of ambient synthetic teineite with distinctive Raman bands, reaching from 50 cm^{-1} to 800 cm^{-1}, consisting of external vibration Raman bands in the low energy region, a very prominent band assigned to the H_2O librational mode, next to different vibration modes of TeO_3.

Following Frost and Keeffes' assumption, as direct comparisons with teineite or closely related phases concerning CuO vibration modes are unavailable, the Raman band at 236 cm^{-1} may correspond to a CuO stretching vibration. Concerning orientation dependent measurements (see Figure 10, 11 and 12) it can be argued that with switching the orientation of the crystal, the detected Raman bands show a rather mediate change in intensity in relation to one another at most. After focusing on the orientation of the crystal relative to the sample stage and observing the ratio between each band for each spectrum over the course of three orientation dependent series (see Figure 32), it can be clearly stated from the first (s1) and second (s2) series of measurements at 1 bar (not so much for the third series (s3), as the intensity is much weaker overall) that the Raman bands at 740, 350, 285, 305 as well as 180 cm^{-1} are comparatively stronger, when the crystals' presumed crystallographic c-axis is parallel to the x-axis of the sample stage. In comparison, Raman bands at 670 and 136 cm^{-1} are relatively stronger, when the samples' assumed crystallographic a-axis is oriented parallel to the sample stages' x-axis.

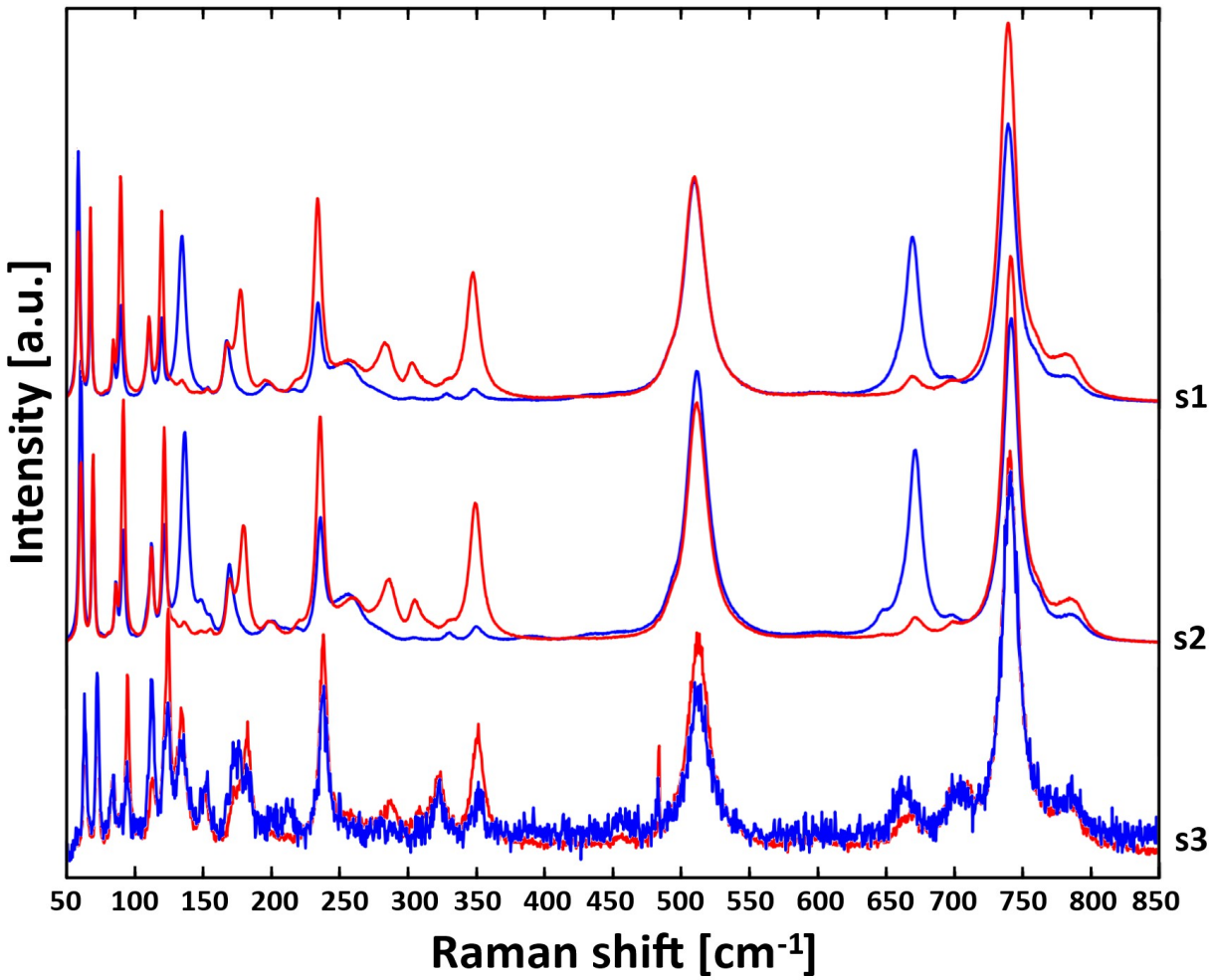

Figure 32: Comparative graph of orientation dependent Raman measurements series: spectra marked in blue are a result of orienting the samples' crystallographic a-axis close to the sample stages' x-axis. Spectra represented in red are attributed to the crystals c-axis being oriented approximately to the sample stages' x-axis.

Over the course of all three pressure variable Raman measurement series (s1, s2 and axr1) a blueshift of Raman bands was observed upon compression, consistent with the expected increase in phonon frequencies, caused by crystal lattice strain under pressure. As reported for all Raman measurement series in chapter 3.2, bands in the low energy region demonstrated convergence with increasing pressure, which can be attributed to the limitations of spectral resolution. As the pressure increased, the separation between the bands diminished, eventually exceeding the spectrometer's ability to resolve them as distinct. Upon decompression, the previously converged bands in the low-energy region exhibited gradual separation.

Aside from the expected blueshift of Raman bands, next to broadening, occasional slight tilting, decrease in intensity, as well as convergence of bands due to spectral resolution during compression, it can be claimed that in the case of Raman measurement series s1 and axr1 a first-order phase transition occurred in contrary to Raman measurement series s2 (see Figure 33). The phase transition during Raman measurement series s1 is most dominantly marked by the emergence of a prominent Raman band at ~435 cm^{-1} between 6.86 and 7.73 GPa, as well as the surpassing in intensity for the Raman band at ~713cm^{-1}, when compared to adjacent Raman bands. For series axr1, the Raman profile showed comparable signs of an first-order phase transition at 7.67 GPa, as dominant Raman bands, distinct from the profile seen at ambient conditions, also emerged at 440, 386 and 398 cm^{-1}, next to a Raman band relatively high in intensity at around 720 cm^{-1}. Aside from the newly emerged dominant Raman bands significant pressure discrepancies were observed between 4.62 and 1.54 GPa for series s1 and between 3.26 and 0.34 GPa for axr1. These discrepancies can be attributed to assumed volumetric changes of the sample, also hinting at a phase transition of first-order, although it is also potentially influenced by errors associated with the manual adjustment of the diamond anvil cell pressure screws.

Upon decompression, series 1 demonstrated a presumed reversal of the phase transition, shown by Raman bands returning to their initial positions and relative intensity compared to one another between 4.62 GPa and 1.54 GPa, while the same applies to axr1 between 3.26 and 0.34 GPa, demonstrating a rather high hysteresis, also being associable with a first-order phase transition. Focusing on series s2, data lacks the already mentioned signs for an assumed first-order phase transition, most evidently linked to the pressure increase rate over time.

The increase rate was calculated by taking the time of initial pressure change after loading as starting point and the time of reaching the maximum pressure as end point, including all hours in between, even when the DAC was at rest so to speak. As measurement series s2 was brought to the maximum pressure of 7.97 GPa at a mediate pressure increase rate of 2.24 GPa/h, while series s1 reached its maximum in pressure with a mediate rate of 3.661 $x10^{-2}$ GPa/h and axr1 was compressed at a rate of 10.507 $x10^{-2}$ GPa/h, it can be interpreted that in the case of series s2, the pressure was most likely applied to quickly beyond a critical point. As a result, the sample possibly remained in a metastable state, causing the absence of a detectable first-order phase transition via analysis of Raman bands. This hints at a rather high sensitivity concerning compression rates from alpha to beta phase. In contrary, pressure decrease rates applied in series s1 ($3.392x10^{-2}$ GPa/h) and axr1 (1.875 GPa/h) demonstrated no direct effect, when returning back from beta phase to alpha phase. However, this fact does not exclude the possibility of a potentially earlier reversal of the phase transition back to the alpha phase, in case a lower decrease rate would have been chosen.

Observing the general quality and reliability of collected data, the lack of being able to calibrate the used device precise sufficiently and the implicated worsening of such over time when not readjusted regularly, which results in the tendency of a defective, slowly progressive blueshift of measured spectra, must be taken into account. Therefore, not only does the measured pressure have to be assigned with a certain degree of error but also Raman band positions associated to the same vibration mode may differ from one series to the next. Apart from calibration, Raman band position errors are proportional to increasing pressure, explainable by the increased amount of strain on the crystal lattice, resulting in a decrease of intensity, broadening of bands, as well as visible tilting of Raman bands.

Another notable observation is that the creation of domains was first visible during compression for s1 at 6.86 GPa, for s2 at 7.14 GPa and for axr1 at 6.85 GPa, not reflecting any measured changes in the Raman band profile for s1 and s2, therefore noted as not being directly linked to the phase transition. Additionally, the seemingly observed disappearance of phase boundaries during decompression, e.g. visible in Figure 7f, is most likely a result of differences in levels of focus during measurements and cannot be associated with a phase transition back towards the initial structural state. And yet, the existence of domains is not to be deemed irrelevant, as multiple domains were possibly measured at the same time within each sample.

Concerning the relation to the already known isochemical polymorph of teineite found in nature, namely millsite (Rumsey et al., 2018), it is clear to see a Raman band profile distinct from the presumed high-pressure phase in this study. While Rumsey et al. (2019) appointed the symmetric and antisymmetric stretching mode of millsite to a Raman band at 749 cm^{-1} and a shoulder located to the right, the high-pressure phase in this study seemingly shows the same modes at 7.67 GPa for axr1 at ~720cm^{-1} with shoulders left and right of it. The vibrational bending modes of $(TeO_3)^{2-}$, assigned to millsite at 339 cm^{-1}, are potentially located at ~386cm^{-1} with a very close left shoulder and at around 398 cm^{-1} and 440 cm^{-1} for the high-pressure polymorph of teineite. The H_2O librational mode, located for millsite at around 484 cm^{-1}, is hardly trackable throughout higher pressures. By comparing data from series s1, s2 and axr1, there are two options for its position. Either the Raman band was affected by a rather strong blueshift as a direct cause of the presumed phase transition and is therefore positioned at ~600 cm^{-1}, or the H_2O librational mode did not shift relative drastically and follows a more constant blueshift rate towards a position at around 580 cm^{-1}, close to the intensity background.

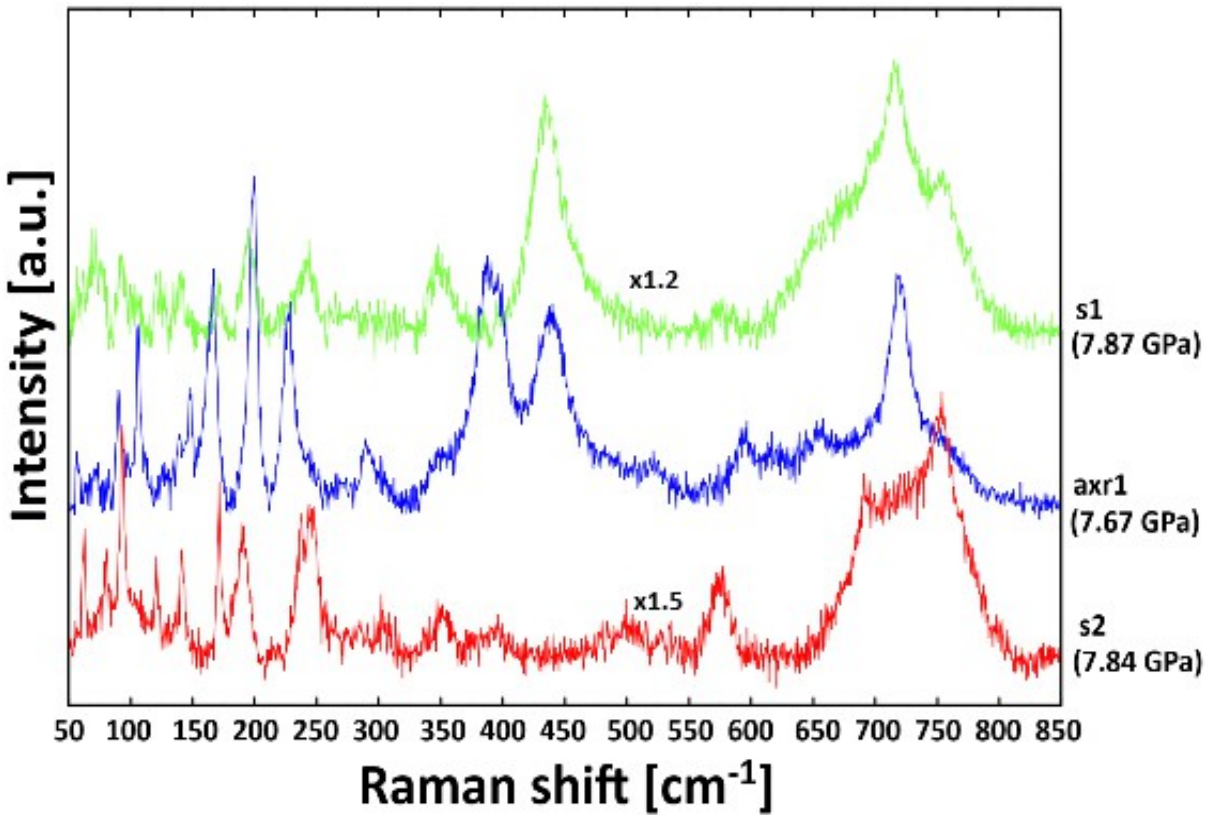

Figure 33: Comparison of high-pressure Raman measurement series s1 (green), s2 (red) and axr1 (blue) at maximum pressure. In this graph the spectrum for axr1 was shifted along the x-axis for comparative reasons, as calibration errors differ from series to series. Multiplying factor for rescaled spectra in y-axis direction is displayed on top.

In comparison to the phase transition of synthetic teineite seen in this study, the closely related mineral chalcomenite (Gonzalez-Platas et al., 2019) displays a rather nuanced change in Raman band positions. As the phase transition of chalcomenite at 4.5(2) GPa is of first-order as well, it can be mainly characterized by the splitting of Raman bands in the lower energy region

X-ray Diffraction

Overall, the proposed high pressure structure models for x-ray 2 (see Figure 29) and x-ray 3 (see Figure 30) sustain the initial space group ($P2_12_12_1$). With a mediate pressure increase rate of 1.501 x 10^{-2} GPa/h the measured sample showed no visible appearance of domains (see Figure 8a-c), visually confirming the SXRD measurement of a maintained single crystal. Significant changes for Te and Cu coordination are observed under compression in comparison to ambient conditions (see Figure 28). A critical alteration of the unit cell volume was observed (see Table 2). From initially 475.31 $Å^3$ the unit cell decreased down by 25.48% for x-ray 2 and 26.45 % for x-ray 3. Changes in unit cell parameters are also notable, as *a* becomes smaller by 21.91 %, *c* becomes smaller by 9.82 % and *b*, the longest axis, becomes larger by 6.27 % for x-ray 2. For x-ray 3 the unit cell axis *a* becomes 21.99 % smaller, as *c* decreased by 9.84 % and *b* becomes bigger by 5.63 %.

While both high pressure structure models are relatively comparable, the high discrepancy of b between x-ray 2 and x-ray 3, and subsequently all parameters derived from this value, are caused by limited data acquisition in the *b*-direction, due to the restricted opening angle inherent in diamond anvil cell experiments. The calculated density for the high pressure phase hints at a more closely packed structure, increasing density by 20.39 % for x-ray 2 and 25.36 % for x-ray 3.

Comparative analysis of atom positions for Cu and Te between the structure model at 1 bar and both high pressure models (see Table 3a) reveals the smallest positional deviation along the a-axis, in contrast to b and c. Furthermore, oxygen atoms exhibit substantial differences, leading to a drastic modification of Te and Cu coordination environments. Regarding anisotropic displacement parameters (see Table 3b), increased values hint at a heightened state of dynamic disorder within the crystal structure. Te-O bond lengths undergo a shortening for O2 and O3 (noted with * in Table 4) concurrent with a decrease in bond angles within the Te coordination polyhedron.

This results in a transformation of the $Te^{[3]}$ coordination figure into a $Te^{[3+3]}$ polyhedron. The novel incorporated oxygen atoms O2* and O3* possess intermediate atomic interactions with Te, as a bond length of 2.45 Å for bond lengths can be taken as a threshold between strong and weak atomic interactions (Christy et al., 2016). The incorporation of the O5* atom however can merely be based on geometrical conditions, having a bond length of 3.028(12) Å for x-ray 2 and 3.016(12) Å for x-ray 3. The proposal of a Te coordination modification can be further supported by a decrease in the distortion index for TeO_{3+3} of 15.99 % for x-ray 2 and 16.68 % for x-ray 3. Conversely, assuming the TeO_3 coordination is maintained during high pressure, the respective distortion index increases from 0.00105 at ambient conditions to 0.02139 (x-ray 2) and 0.01894 (x-ray 3). For Cu, changes in bond lengths and angles of O3 and O5 are observed as well, indicating a reorientation of the respective coordination polyhedra. This results in an increase in distortion index of 21.14% for x-ray 2 and 31.27 % for x-ray 3, while preserving the initial number of coordinated oxygens atoms.

Concerning connectivity, the displayed coordination polyhedra between Cu and Te evolve from sharing oxygen atoms solely at corners at ambient conditions to additionally sharing edges between O1 and O2 at high-pressure. This transition leads to increased structural rigidity and heightened electrostatic repulsion. Consequently, the two proposed high-pressure structural models for synthetic teineite exhibit varying degrees of compaction along the crystallographic axes. Minimal compaction is observed in the (100) plane of the high-pressure phase, while a slight structural compaction is evident in the (001) plane. Notably, interpolyhedral cavities experience a drastic reduction in volume within the (010) plane.

5. Conclusion

Synthetic teineite underwent a first-order phase transition upon compression between 6.86 and 7.67 GPa. High-pressure SXRD models concur that measured samples experienced a rearrangement of their structure, while maintaining the spacegroup $P2_12_12_1$. The unit cell shows decreased parameters *a* and *c*, while parameter *b* lengthened. Cu and Te atoms underwent a reorganization of their positions, most notable in the crystallographic *b* and *c* plane. Coordination number of Cu with 4+1 maintains, in contrast to the coordination figure of Te, which evolves from $Te^{[3]}$ to $Te^{[3+3]}$, caused by shortening of associated bond lengths and considering geometrical conditions. Complimented by Raman spectroscopy, structural changes are most prominently marked by the display of novel dominant Raman bands, e.g. visible at 7.67 GPa at around 391 and 440 cm^{-1}, associable to the v_4 Raman mode and at 720 cm^{-1}, correlated to the v_3 Raman mode. This goes alongside the softening of initially detected Raman bands assigned to the vibrational modes of v_1, v_3 and H_2O librational mode. In consequence of the modification from $Te^{[3]}$ to $Te^{[3+3]}$, Te and Cu coordination polyhedra are no longer solely connected via oxygen sharing corners, but also via an edge. Therefore, the structure becomes more rigid at high-pressure. This causes atoms to experience increased electrostatic repulsion and a heightened state of dynamic disorder, as data on anisotropic displacement parameters suggests. Consequently, these modifications caused a compaction of the structure, most pronounced in the (010) plane. Following measured decompression steps, spectra demonstrated a presumed reversal of the phase transition, marked by strong pressure jumps of 3.08 GPa at most, with Raman bands returning to their initial profile between 4.62 GPa and 1.54 GPa for series s1, while the same applies to axr1 between 3.26 GPa and 0.34 GPa. The substantial discrepancy in pressure points associated with the phase transition between compression and decompression indicates the presence of a hysteresis, typically observed for phase transitions of first-order. Being neither comparable to the isochemical mineral millsite (Rumsey et al., 2018) in terms of structure or Raman band profile, nor relatable to its Se-analogue chalcomenite (Gonzalez-Platas et al., 2019) concerning marks of a dedicated phase transition, a novel high-pressure polymorph of synthetic teineite with unique structural properties can be established among the field of high-pressure studies on Te-oxycompounds.

6. List of Figures

7. List of Tables

8. List of Equations

9. References

Allan, D. R., Miletich, R. and Angel, R. J. (1996): A diamond-anvil cell for single-crystal x-ray diffraction studies to pressures in excess of 10 GPa. Review of Scientific Instruments, 67. p. 840.

Andreeva, E., Matsueda, H., Okrugin, V., Takahash,i R. and Ono, S. (2013): Au–Ag–Te Mineralization of the Low-Sulfidation Epithermal Aginskoe Deposit, Central Kamchatka, Russia. Resource Geology, 63 (4). p. 337-349.

Anthony, J.W., Williams, S. A., Bideux, R. A., Grant, R. W. and Wilson, W. E. (1995): Mineralogy of Arizona. University of Arizona Press. p. 389.

Baur, W. H. (1974): The geometry of polyhedral distortions. Predictive relationships for the phosphate group. Acta Crystallographica Section B, Structural Crystallography and Crystal Chemistry,30 (5). p. 1195-1215.

Berger, L. I. (1997): Semiconductor Materials. CRC Press. p. 89-91.

Christy, A. G., Mills, S. J. and Kampf, A. R. (2016): A review of the structural architecture of tellurium oxycompounds. Mineralogical Magazine, 80 (3). p. 415-545.

Das, A. and Banik, B. K. (2022): Tellurium-based solar cells. Physical Sciences Reviews., 8 (12). p. 4631-4658.

Datchi, F., Dewaele, A., Loubeyre, P., Letoullec, R., Le Godec, Y. and Canny, B. (2007): Optical pressure sensors for high-pressure-high-temperature studies in a diamond anvil cell. High Pressure Research, 27 (4). p.447-463.

Du Ry, P., Fouassin, M., Jedwab, J. and Van Tassel, R. (1976): Occurrence de chalcoalumite, de minéraux de tellure (teinéite et paratellurite) et de béryl à Salmchâteau, Ardennes belges Université de Liège. Annales de la Société géologique de Belgique, 99 (1). p. 47-60.

Effenberger, H. S. (1977): Verfeinerung der Kristallstruktur von synthetischem Teineit, $CuTeO_3 \cdot 2H_2O$. Tschermaks mineralogische und petrographische Mitteilungen, 24 (4). p. 287-298.

Frost, R. L. and Keeffe, E. C. (2009): Raman spectroscopic study of the tellurite minerals: graemite $CuTeO_3 \cdot H_2O$ and teineite $CuTeO_3 \cdot 2H_2O$. Journal of Raman Spectroscopy, 40 (2). p. 128-132.

Gonzalez-Platas, J., Rodriguez-Hernandez, P., Muñoz, A., Rodríguez-Mendoza, U. R., Nénert, G., Errandonea, D. (2019): A High-Pressure Investigation of the Synthetic Analogue of Chalcomenite, $CuSeO_3 \cdot 2H_2O$. Crystals, 9 (12). p. 643.

Isbrekken, K. A. (1991): Oppdal-ett mineralparadis?. STEIN, 18 (4). p. 56-57.

Jha, A., Richards, B. D. O., Jose, G., Toney Fernandez, T., Hill, C. J., Lousteau, J., Joshi, P. (2012): Review on structural, thermal, optical and spectroscopic properties of tellurium oxide based glasses for fibre optic and waveguide applications. International Materials Reviews, 57 (6). p. 357.

Kato, A. and Sakurai, K. (1968): The Occurrence of Teineite from the Kawazu (rendaiji) Mine, Shizuoka Prefecture, Japan. Mineralogical Journal, 5 (4). p. 285-290.

Klotz, S., Paumier, L., Le March, G. and Munsch, P. (2009): The effect of temperature on the hydrostatic limit of 4: 1 methanol–ethanol under pressure. High Pressure Research, 29 (4). p. 649-652.

Knee, D. W. (1984): Tellurium -an unusual carbon oxidation catalyst. Carbon, 22 (6). p. 513-516.

Lotti, P., Milani, S., Merlini, M., Joseph, B., Alabarse,Lausi., A. (2020): J. Synchrotron Rad., 27. p. 222–229.

Mao, H. K. and Bell, P. M. (1980): Design and operation of a diamond-window, high-pressure cell for the study of single-crystal samples loaded cryogenically. Carnegie Inst. Washington Year Book, 79. p. 409-411.

Miletich, R. (1995): Crystal chemistry of the microporous tellurite minerals zemannite and kinichilite, Mg0.5[Me2+Fe3+(TeO3)3]-4.5H2O, (Me2+=Zn;Mn). European Journal of Mineralogy, 7 (3). p. 509-524.

Miletich, R., Allan, D. R. and Kuhs, W. F. (2000): High-Pressure Single-Crystal Techniques. Reviews in Mineralogy and Geochemistry, 41. p. 445–519.

Momma, K. and Izumi, F. (2011): VESTA 3 for three-dimensional visualisation of crystal, volumetric and morphology data. J. Appl. Cryst., 44. p.1272-1276.

Prescher, C. and Prakapenka, V. B. (2015): High Pressure Res., 35. p. 223–230.

Rewitzer, C. (2001): Bambolla, Bambollita, San Miguel und Candelaria: Untertage-Funde und Typmineralien von Moctezuma Typmineralien und klassische Funde Mineralliste der Gold/Tellur-Lagerstätten von Moctezuma, Mexiko. Lapis, 24 (1). p. 11-40.

Rigaku Oxford Diffraction, CrysAlisPro Software system, version 1.171.43. (2024): Rigaku Corporation, Wrocław, Poland.

Rumsey, M., Welch, M. D., Mo, F., Kleppe, A., Spratt, J., Kampf, A., Raanes, M. P. (2018): Millsite, CuTeO3·2H2O; a new polymorph of teineite from Graurdfjellet, Oppdal, Norway. Mineralogical Magazine, 82 (2). p. 433-444.

Sheldrick, G.M. (2008): Acta Cryst., A64. p. 112–122.

Sheldrick, G.M. (2015): Acta Cryst., A71. p. 3–8.

Shen, G., Wang, Y., Dewaele, A., Wu, C., Fratanduono, D. E., Eggert, J., Klotz, S., Dziubek, K. F., Loubeyre, P., Fat'yanov, O. V., Asimow, P. D., Mashimo, T., Wentzcovitch, R. M. M. (2020): High Pressure Res., 40. p. 299–314.

Strunz, H. and Nickel, E. H. (2001): Strunz Mineralogical Tables, 9th Edition.
E. Schweizerbart'sche Verlagsbuchhandlung. p. 280.

Williams, S. A. and Matter III, P. (1975): Graemite, anew Bisbee mineral. Mineralogical Record, 6. p. 32-34.

Yosimura, T. (1939): Teineite, a New Tellurate Mineral from the Teine Mine, Hokkaidō, Japan. Journal of the Faculty of Science, Hokkaido University. Geology and mineralogy,
4 (3-4). p. 465-470.

Zemann, A. und Zemann, J. (1960): Zur Kenntnis des Teineits. Beiträge zur Mineralogie und Petrographie, 7. p. 436-438.

10. Appendix

Compression/Decompression Timetables

High-pressure Raman Measurement Series s1

compression series 1		
date*	**time**	**P [GPa]****
9/8/23	14:59	1.56
9/8/23	16:40	1.71
10/8/23	11:53	1.69
10/8/23	12:31	1.83
10/8/23	12:57	2.57
10/8/23	14:20	3.52
10/8/23	14:51	4.17
10/8/23	15:16	4.62
10/8/23	15:41	5.16
17/8/23	13:22	5.34
17/8/23	13:55	5.43
17/8/23	14:17	5.59
17/8/23	14:39	6.18
17/8/23	15:04	6.86
18/8/23	12:41	7.73
18/8/23	13:29	7.87

decompression series 1		
date*	**time**	**P [GPa]****
29/8/23	13:09	7.36
29/8/23	13:44	7.11
29/8/23	14:08	6.91
29/8/23	14:30	6.74
29/8/23	14:50	6.57
29/8/23	15:12	6.35
29/8/23	15:33	6.01
30/8/23	13:09	6.10
30/8/23	13:14	4.62
30/8/23	13:43	5.68
30/8/23	14:44	1.54
31/8/23	13:35	0.55
31/8/23	14:08	0.44
31/8/23	14:33	0.17
31/8/23	14:52	0.02
7/9/23	14:14	0.80
7/9/23	14:51	0.25
7/9/23	15:13	1 bar

* date is set in the format DD/MM/YY.

** P refers to the pressure measured via the R1 luminscence line of the ruby inside the diamond anvil cell.

High-Pressure Raman Measurement Series axr1/HP-SXRD Measurement x-ray 1

series axr1/x-ray 1 (compression)		
date*	**time**	**P [GPa]****
15/12/23	11:36	1 bar
23/1/24	12:50	1.13
23/1/24	13:10	2.15
23/1/24	13:25	2.87
23/1/24	14:23	3.41
23/1/24	14:41	3.96
23/1/24	15:20	4.37
23/1/24	15:31	4.69
24/1/24	13:21	4.87
24/1/24	13:33	4.94
24/1/24	13:56	5.35
24/1/24	14:11	5.89
24/1/24	14:24	6.75
24/1/24	14:40	6.85
24/1/24	14:58	6.98
24/1/24	15:14	7.16
24/1/24	15:25	7.30
24/1/24	15:39	7.58
26/1/24	13:40	7.67

series axr1/x-ray 1 (decompression)		
date*	**time**	**P [GPa]****
30/5/24	10:53	7.67
30/5/24	11:05	7.58
30/5/24	11:23	7.48
30/5/24	11:37	7.33
30/5/24	11:50	7.19
30/5/24	12:03	7.05
30/5/24	12:23	6.90
30/5/24	12:38	6.67
30/5/24	12:56	6.17
30/5/24	13:12	5.79
30/5/24	13:28	5.32
30/5/24	13:38	4.90
30/5/24	13:51	4.54
30/5/24	14:03	4.07
30/5/24	14:15	3.26
30/5/24	14:30	0.54
30/5/24	14:42	0.17

* date is set in the format DD/MM/YY.

** P refers to the pressure measured via the R1 luminscence line of the ruby inside the diamond anvil cell.

High-pressure Raman Measurement Series s2

compression series 2		
date*	**time**	**P [GPa]****
3/4/24	12:10	1 bar
9/4/24	13:37	1.03
9/4/24	13:51	2.56
9/4/24	14:07	3.9
9/4/24	14:23	4.28
9/4/24	14:57	4.63
9/4/24	15:11	5.55
9/4/24	15:27	5.86
9/4/24	15:42	6.24
9/4/24	16:02	7.14
9/4/24	16:23	7.64
9/4/24	16:39	7.84

decompression series 2		
date*	**time**	**P [GPa]****
26/4/24	12:59	7.97
26/4/24	13:10	7.84
26/4/24	13:34	7.69
26/4/24	13:55	7.43
26/4/24	14:21	7.12
26/4/24	14:38	6.77
26/4/24	15:03	6.08
26/4/24	15:15	5.81
26/4/24	15:32	5.23
26/4/24	15:42	4.82
26/4/24	15:55	4.31
26/4/24	16:03	1.96
26/4/24	16:17	1 bar

HP-SXRD Measurement x-ray 2/x-ray 3

x-ray 2/x-ray 3 (compression)		
date*	**time**	**P [GPa]****
8/7/24	15:02	1 bar
9/7/24	13:09	0.49
11/7/24	13:55	0.85
12/7/24	12:13	1.25
15/7/24	13:35	1.95
17/7/24	15:09	4.39
18/7/24	15:24	4.72
24/7/24	13:54	6.11
29/7/24	13:50	6.69
5/8/24	13:52	7.72

* date is set in the format DD/MM/YY.

** P refers to the pressure measured via the R1 luminscence line of the ruby inside the diamond anvil cell.

Raman Measurement Tables

Raman Compression Series s1

p start (1.56 GPa)

Peak	1	Gauss+Lor	Area			
	Parm	Value	Std Error	t-value	95	
	Area	12606.1351	733.258634	17.1919355	11168.2264	14044.0439
	Ctr	58.5162374	0.04827147	1212.23227	58.4215778	58.610897
	Wid	3.57222844	0.13950172	25.607057	3.29866775	3.84578914
	Shpe	0.8209908	0.17735748	4.629017	0.47319555	1.16878606
Peak	2	Gauss+Lor	Area			
	Parm	Value	Std Error	t-value	95	
	Area	13436.8806	559.392382	24.0204926	12339.9208	14533.8403
	Ctr	67.9395297	0.02526199	2689.39774	67.8899913	67.989068
	Wid	2.09406495	0.08311601	25.1944837	1.93107575	2.25705415
	Shpe	0.39036726	0.11191066	3.48820449	0.17091221	0.60982232
Peak	3	Gauss+Lor	Area			
	Parm	Value	Std Error	t-value	95	
	Area	3499.46228	527.206156	6.63774928	2465.61924	4533.30533
	Ctr	85.1847704	0.09935077	857.414295	84.9899451	85.3795957
	Wid	1.84770437	0.4054998	4.55660977	1.05252558	2.64288316
	Shpe	0.02791912	0.38648321	0.07223889	-0.7299684	0.78580666
Peak	4	Gauss+Lor	Area			
	Parm	Value	Std Error	t-value	95	
	Area	10204.7165	655.584886	15.5658202	8919.12472	11490.3082
	Ctr	92.6987682	0.05548175	1670.79736	92.5899693	92.8075671
	Wid	2.8331467	0.19182363	14.7695393	2.45698354	3.20930985
	Shpe	0.28740655	0.17311922	1.66016552	-0.0520775	0.62689064
Peak	5	Gauss+Lor	Area			
	Parm	Value	Std Error	t-value	95	
	Area	6570.50968	734.674544	8.94342907	5129.82436	8011.195
	Ctr	112.284434	0.08688597	1292.31952	112.114052	112.454817
	Wid	2.8331467	0.2977574	9.51494982	2.24924909	3.41704431
	Shpe	0.28740655	0.27959537	1.02793748	-0.2608756	0.8356887
Peak	6	Gauss+Lor	Area			
	Parm	Value	Std Error	t-value	95	
	Area	4528.60427	855.71775	5.29217054	2850.55511	6206.65343
	Ctr	120.722284	0.17892688	674.701791	120.371412	121.073157
	Wid	3.57222844	0.6132202	5.82536004	2.3697132	4.77474369
	Shpe	0.28740655	0.47632056	0.60338894	-0.6466506	1.22146374
Peak	7	Gauss+Lor	Area			
	Parm	Value	Std Error	t-value	95	
	Area	29221.4029	938.38602	31.1400663	27381.2425	31061.5632
	Ctr	142.788354	0.07200212	1983.11312	142.647159	142.929549
	Wid	6.83090705	0.24952778	27.3753372	6.34158697	7.32022714
	Shpe	0.28740655	0.08891923	3.23222064	0.11303734	0.46177577

Peak	8	Gauss+Lor	Area			
	Parm	Value	Std Error	t-value	95	
	Area	14091.2936	660.404735	21.33736	12796.2502	15386.3369
	Ctr	172.68757	0.06191991	2788.88611	172.566146	172.808994
	Wid	3.80739082	0.21387719	17.8017622	3.38798099	4.22680064
	Shpe	0.28740655	0.13055578	2.20140817	0.03138871	0.5434244
Peak	9	Gauss+Lor	Area			
	Parm	Value	Std Error	t-value	95	
	Area	2902.32609	1142.36626	2.54062658	662.163668	5142.48851
	Ctr	221.458567	0.56627387	391.080323	220.348112	222.569021
	Wid	5.68309071	1.91975101	2.96032698	1.91848893	9.44769248
	Shpe	0.28740655	0.92316994	0.31132573	-1.5229153	2.09772841
Peak	10	Gauss+Lor	Area			
	Parm	Value	Std Error	t-value	95	
	Area	34673.84	1489.40352	23.2803531	31753.1429	37594.5371
	Ctr	236.00224	0.06742015	3500.47049	235.87003	236.13445
	Wid	7.1668533	0.22812235	31.416708	6.71950893	7.61419768
	Shpe	0.28740655	0.09927261	2.89512433	0.09273451	0.4820786
Peak	11	Gauss+Lor	Area			
	Parm	Value	Std Error	t-value	95	
	Area	18419.3842	1663.0543	11.0756361	15158.1607	21680.6077
	Ctr	269.456887	0.39550921	681.291051	268.6813	270.232474
	Wid	15.6215006	1.368398	11.4159042	12.9380934	18.3049077
	Shpe	0.28740655	0.24009979	1.19702962	-0.1834254	0.75823849
Peak	12	Gauss+Lor	Area			
	Parm	Value	Std Error	t-value	95	
	Area	437.325287	740.9997	0.59018281	-1015.7636	1890.41414
	Ctr	315.929451	2.51919615	125.408834	310.989347	320.869556
	Wid	4.47928331	8.70678566	0.51445889	-12.594588	21.5531542
	Shpe	0.28740655	4.63299652	0.0620347	-8.7978274	9.37264046
Peak	13	Gauss+Lor	Area			
	Parm	Value	Std Error	t-value	95	
	Area	968.843713	979.854716	0.98876262	-952.6361	2890.32353
	Ctr	341.405375	1.36946611	249.298155	338.719873	344.090877
	Wid	5.03919373	4.70812161	1.07031936	-4.1933593	14.2717468
	Shpe	0.28740655	2.48833291	0.11550165	-4.5921755	5.16698856
Peak	14	Gauss+Lor	Area			
	Parm	Value	Std Error	t-value	95	
	Area	6566.60739	1284.03309	5.11404843	4048.63854	9084.57624
	Ctr	359.322508	0.48300321	743.933989	358.375347	360.26967
	Wid	8.95856663	1.65103247	5.42603903	5.72091771	12.1962155
	Shpe	0.28740655	0.50378202	0.57049783	-0.7005021	1.27531525
Peak	15	Gauss+Lor	Area			
	Parm	Value	Std Error	t-value	95	
	Area	1740.46758	1523.81466	1.142178	-1247.7092	4728.64436
	Ctr	452.183651	2.66823355	169.469292	446.951286	457.416015
	Wid	14.893617	7.37925522	2.01830897	0.42301266	29.3642214
	Shpe	1	2.73041422	0.3662448	-4.3542997	6.35429969

Peak	16	Gauss+Lor	Area			
	Parm	Value	Std Error	t-value	95	
	Area	20858.0133	2863.81824	7.28328811	15242.1104	26473.9162
	Ctr	507.318029	0.43159985	1175.43606	506.471669	508.16439
	Wid	15.6215006	0.94982771	16.4466675	13.7589032	17.4840979
	Shpe	1	0.34233223	2.92113894	0.32869184	1.67130816
Peak	17	Gauss+Lor	Area			
	Parm	Value	Std Error	t-value	95	
	Area	1.004e+05	2694.56237	37.2619892	95120.7594	1.0569e+05
	Ctr	527.5028	0.10391944	5076.07453	527.299015	527.706584
	Wid	17.2452408	0.24030008	71.7654392	16.7740161	17.7164655
	Shpe	1	0.06456522	15.488214	0.8733886	1.1266114
Peak	18	Gauss+Lor	Area			
	Parm	Value	Std Error	t-value	95	
	Area	46080.3984	1199.8921	38.403785	43727.4287	48433.3681
	Ctr	679.115342	0.07962719	8528.68603	678.959194	679.271489
	Wid	12.8555431	0.21843051	58.8541551	12.4272043	13.2838819
	Shpe	1	0.08314992	12.0264702	0.83694431	1.16305569
Peak	19	Gauss+Lor	Area			
	Parm	Value	Std Error	t-value	95	
	Area	1.8187e+05	1168.61922	155.627474	1.7958e+05	1.8416e+05
	Ctr	747.519597	0.03350818	22308.5731	747.453888	747.585306
	Wid	12.8492414	0.13356731	96.200496	12.587318	13.1111648
	Shpe	0.02791912	0.01758501	1.58766607	-0.0065648	0.06240304

Raman Decompression Series s1

p start (7.36 GPa)

Peak	1	Gauss+Lor	Area			
	Parm	Value	Std Error	t-value	95	
	Area	2153.87796	290.041383	7.42610566	1584.99963	2722.75628
	Ctr	68.7723853	0.40827319	168.446977	67.9716107	69.5731599
	Wid	13.3894215	1.25528527	10.6664371	10.9273432	15.8514997
	Shpe	0.50140891	0.34437328	1.45600413	-0.1740343	1.17685216
Peak	2	Gauss+Lor	Area			
	Parm	Value	Std Error	t-value	95	
	Area	863.014266	295.916786	2.91640862	282.612102	1443.41643
	Ctr	88.7430962	0.30886572	287.319343	88.1372964	89.348896
	Wid	5.70858304	0.99190224	5.75518718	3.76309623	7.65406985
	Shpe	0.38570462	0.68739418	0.56111126	-0.9625294	1.7339386
Peak	3	Gauss+Lor	Area			
	Parm	Value	Std Error	t-value	95	
	Area	473.210584	448.862172	1.05424474	-407.174	1353.59517
	Ctr	102.184528	0.92933497	109.954464	100.361759	104.007297
	Wid	7.53170198	3.14020931	2.39847133	1.37259117	13.6908128
	Shpe	0.29329025	1.81014544	0.16202579	-3.2570738	3.84365435
Peak	4	Gauss+Lor	Area			
	Parm	Value	Std Error	t-value	95	
	Area	542.214191	466.473751	1.16236806	-372.7132	1457.14159
	Ctr	118.847443	0.99201855	119.80365	116.901728	120.793158
	Wid	9.18673888	3.05154135	3.01052413	3.20153869	15.1719391
	Shpe	0.49196108	1.88974354	0.26033219	-3.2145243	4.19844645
Peak	5	Gauss+Lor	Area			
	Parm	Value	Std Error	t-value	95	
	Area	826.0329	235.785841	3.5033185	363.569739	1288.49606
	Ctr	136.565551	0.33894435	402.91438	135.900756	137.230346
	Wid	5.99860129	1.10590725	5.42414502	3.82950853	8.16769406
	Shpe	0.33426703	0.59997181	0.55713789	-0.8424994	1.51103344
Peak	6	Gauss+Lor	Area			
	Parm	Value	Std Error	t-value	95	
	Area	739.505545	224.550482	3.29327079	299.079074	1179.93202
	Ctr	166.655138	0.65911162	252.848127	165.362377	167.9479
	Wid	7.88833549	2.56039157	3.0809098	2.86646152	12.9102095
	Shpe	0.0422499	0.643792	0.06562663	-1.2204641	1.30496391
Peak	7	Gauss+Lor	Area			
	Parm	Value	Std Error	t-value	95	
	Area	2141.21496	300.526404	7.12488131	1551.77163	2730.65829
	Ctr	189.643152	0.37764679	502.170702	188.902447	190.383857
	Wid	12.9201624	1.18740223	10.8810327	10.5912279	15.249097
	Shpe	0.46858086	0.35656467	1.31415393	-0.2307742	1.16793592

Peak	8	Gauss+Lor	Area			
	Parm	Value	Std Error	t-value	95	
	Area	1390.82142	251.974897	5.51968245	896.605534	1885.0373
	Ctr	237.987942	0.5645225	421.57388	236.880705	239.095179
	Wid	12.2722706	1.9300475	6.35853292	8.48673424	16.0578069
	Shpe	0.30313903	0.44763143	0.67720675	-0.5748316	1.18110968
Peak	9	Gauss+Lor	Area			
	Parm	Value	Std Error	t-value	95	
	Area	1244.15857	456.025071	2.72826791	349.724895	2138.59224
	Ctr	296.378319	2.38008696	124.524156	291.710089	301.046549
	Wid	25.7202352	9.24418438	2.78231526	7.58897378	43.8514967
	Shpe	0	0.7837776	0	-1.5372775	1.53727749
Peak	10	Gauss+Lor	Area			
	Parm	Value	Std Error	t-value	95	
	Area	2312.01547	320.732646	7.20854425	1682.94024	2941.09071
	Ctr	344.827457	0.56972086	605.256856	343.710024	345.94489
	Wid	15.8853332	2.10512604	7.54602475	11.7564031	20.0142632
	Shpe	0.11599145	0.29525157	0.39285633	-0.463106	0.69508887
Peak	11	Gauss+Lor	Area			
	Parm	Value	Std Error	t-value	95	
	Area	8517.11505	320.408679	26.582036	7888.67524	9145.55487
	Ctr	431.144043	0.25604291	1683.87417	430.641848	431.646237
	Wid	25.3371183	0.84794554	29.8805964	23.6739838	27.0002528
	Shpe	0.39340773	0.10133591	3.88221447	0.19465057	0.59216489
Peak	12	Gauss+Lor	Area			
	Parm	Value	Std Error	t-value	95	
	Area	1187.15774	486.992705	2.43773208	231.985094	2142.33039
	Ctr	523.35075	2.81021952	186.23127	517.838871	528.862629
	Wid	27.2897132	10.7229589	2.54497974	6.25802848	48.3213978
	Shpe	0	0.79666125	0	-1.5625471	1.56254709
Peak	13	Gauss+Lor	Area			
	Parm	Value	Std Error	t-value	95	
	Area	2211.89999	436.78443	5.06405412	1355.20433	3068.59566
	Ctr	572.387521	1.20251882	475.990488	570.028938	574.746105
	Wid	23.6528369	4.64669753	5.09024672	14.538946	32.7667277
	Shpe	0	0.37583564	0	-0.7371526	0.73715256
Peak	14	Gauss+Lor	Area			
	Parm	Value	Std Error	t-value	95	
	Area	5916.00061	1754.73598	3.37144772	2474.31496	9357.68627
	Ctr	685.289831	0.8515883	804.719644	683.619552	686.96011
	Wid	24.4744387	2.8660395	8.53946317	18.8530762	30.0958012
	Shpe	0	0.16463708	0	-0.3229142	0.32291416
Peak	15	Gauss+Lor	Area			
	Parm	Value	Std Error	t-value	95	
	Area	10174.5716	3514.53809	2.8949954	3281.26372	17067.8795
	Ctr	711.701417	0.37798971	1882.85925	710.96004	712.442795
	Wid	25.0453833	2.62193673	9.55224548	19.9027965	30.1879701
	Shpe	0.15045003	0.39249424	0.38331779	-0.6193762	0.92027627

Peak	16	Gauss+Lor	Area			
	Parm	Value	Std Error	t-value	95	
	Area	12210.6676	1708.02231	7.14900941	8860.60468	15560.7305
	Ctr	751.06383	1.5167925	495.165839	748.088839	754.03882
	Wid	40.9237761	3.50474417	11.67668	34.0496777	47.7978745
	Shpe	0.17015516	0.09859527	1.72579445	-0.0232266	0.36353692

Raman Series axr1

p start (7.67 GPa)

Peak	1	Gauss+Lor	Area			
	Parm	Value	Std Error	t-value	95	
	Area	426.24627	155.251569	2.74551988	121.717407	730.775133
	Ctr	57.608549	0.39457073	146.003099	56.8345911	58.3825069
	Wid	4.29074338	1.40468029	3.05460495	1.53543665	7.0460501
	Shpe	0.20931962	0.83392243	0.25100611	-1.4264349	1.8450741
Peak	2	Gauss+Lor	Area			
	Parm	Value	Std Error	t-value	95	
	Area	566.199959	233.439708	2.4254655	108.303594	1024.09632
	Ctr	72.1359802	0.75257546	95.8521557	70.6597894	73.6121711
	Wid	7.73527572	2.73735122	2.82582508	2.36590999	13.1046415
	Shpe	0.15289826	0.96432642	0.15855447	-1.7386461	2.04444261
Peak	3	Gauss+Lor	Area			
	Parm	Value	Std Error	t-value	95	
	Area	918.032844	135.154723	6.79245849	652.924322	1183.14137
	Ctr	90.7301969	0.16740772	541.971404	90.4018235	91.0585703
	Wid	4.12866485	0.59100477	6.98584019	2.96939792	5.28793177
	Shpe	0.2359432	0.3633389	0.64937501	-0.4767529	0.94863926
Peak	4	Gauss+Lor	Area			
	Parm	Value	Std Error	t-value	95	
	Area	1352.39599	131.960374	10.2485008	1093.55325	1611.23874
	Ctr	106.627784	0.1026648	1038.60118	106.426405	106.829163
	Wid	3.99948382	0.34865413	11.4712075	3.31559221	4.68337542
	Shpe	0.32362485	0.24757965	1.30715448	-0.1620073	0.80925698
Peak	5	Gauss+Lor	Area			
	Parm	Value	Std Error	t-value	95	
	Area	575.707614	527.2499	1.09190654	-458.50295	1609.91818
	Ctr	127.118995	1.53063482	83.049852	124.116626	130.121364
	Wid	8.30838259	5.32887316	1.5591256	-2.144302	18.7610672
	Shpe	0	0.96389986	0	-1.8907076	1.89070764
Peak	6	Gauss+Lor	Area			
	Parm	Value	Std Error	t-value	95	
	Area	888.554992	1048.21756	0.84768184	-1167.5434	2944.65338
	Ctr	139.632072	0.77197068	180.877428	138.117837	141.146307
	Wid	7.89838311	3.10578495	2.54311977	1.80632771	13.9904385
	Shpe	0.07682349	1.53143187	0.05016449	-2.9271088	3.08075582
Peak	7	Gauss+Lor	Area			
	Parm	Value	Std Error	t-value	95	
	Area	1585.88083	679.607803	2.33352358	252.817385	2918.94428
	Ctr	148.751432	0.46274052	321.457542	147.843757	149.659106
	Wid	8.00991537	1.52585474	5.24946129	5.0169227	11.002908
	Shpe	0.081796	0.49781128	0.16431126	-0.8946702	1.05826216

Peak	8	Gauss+Lor	Area			
	Parm	Value	Std Error	t-value	95	
	Area	3363.61174	305.305877	11.0171864	2764.74854	3962.47494
	Ctr	165.960061	0.13189318	1258.29143	165.70135	166.218772
	Wid	8.30509688	0.39201028	21.1859159	7.53616136	9.0740324
	Shpe	0.46917124	0.1868243	2.51129662	0.10271187	0.83563062
Peak	9	Gauss+Lor	Area			
	Parm	Value	Std Error	t-value	95	
	Area	4752.86736	169.301147	28.0734505	4420.77999	5084.95473
	Ctr	199.293387	0.0716951	2779.73519	199.152756	199.434019
	Wid	7.72964707	0.23024055	33.5720493	7.27802591	8.18126822
	Shpe	0.47126298	0.09746257	4.83532253	0.28008831	0.66243764
Peak	10	Gauss+Lor	Area			
	Parm	Value	Std Error	t-value	95	
	Area	3234.88176	167.042572	19.3656127	2907.22462	3562.53889
	Ctr	228.092668	0.13105155	1740.48052	227.835608	228.349728
	Wid	8.62685511	0.43713445	19.7350153	7.76940769	9.48430253
	Shpe	0.36792514	0.14031545	2.62212859	0.09269377	0.64315652
Peak	11	Gauss+Lor	Area			
	Parm	Value	Std Error	t-value	95	
	Area	1575.96119	249.446957	6.31782088	1086.66631	2065.25607
	Ctr	293.26279	0.60743942	482.785244	292.071286	294.454294
	Wid	13.8665734	2.1850059	6.3462407	9.58064336	18.1525034
	Shpe	0.1931011	0.37770738	0.51124525	-0.547779	0.93398121
Peak	12	Gauss+Lor	Area			
	Parm	Value	Std Error	t-value	95	
	Area	2387.4684	647.77066	3.68566925	1116.85411	3658.08269
	Ctr	351.903464	1.30294872	270.082359	349.347706	354.459222
	Wid	23.907154	4.72501065	5.05970373	14.6389571	33.175351
	Shpe	0.02654452	0.40643012	0.0653114	-0.7706758	0.82376482
Peak	13	Gauss+Lor	Area			
	Parm	Value	Std Error	t-value	95	
	Area	11789.0337	1011.35724	11.6566464	9805.23753	13772.8299
	Ctr	391.043195	0.22213047	1760.42126	390.607482	391.478908
	Wid	26.0246598	0.67334416	38.6498633	24.7038826	27.345437
	Shpe	0.44914606	0.17617326	2.54945647	0.10357891	0.79471322
Peak	14	Gauss+Lor	Area			
	Parm	Value	Std Error	t-value	95	
	Area	10161.3762	664.203521	15.2985882	8858.5285	11464.2238
	Ctr	439.529434	0.30845234	1424.95087	438.924399	440.134469
	Wid	27.1312044	0.97841521	27.729745	25.2120246	29.0503842
	Shpe	0.33138407	0.11769081	2.81571755	0.10053135	0.56223679
Peak	15	Gauss+Lor	Area			
	Parm	Value	Std Error	t-value	95	
	Area	2283.6273	613.788347	3.72054523	1079.66996	3487.58465
	Ctr	519.962232	1.20755249	430.591825	517.593595	522.330869
	Wid	25.5650096	4.87381377	5.24538089	16.0049326	35.1250867
	Shpe	0	0.41895771	0	-0.8217934	0.82179339

Peak	16	Gauss+Lor	Area			
	Parm	Value	Std Error	t-value	95	
	Area	2501.16974	2443.46749	1.0236149	-2291.7376	7294.07703
	Ctr	593.481187	2.44498986	242.733599	588.685294	598.27708
	Wid	20.9817102	6.92124512	3.03149359	7.40555819	34.5578623
	Shpe	0.24972942	0.52915292	0.47194187	-0.788214	1.28767279
Peak	17	Gauss+Lor	Area			
	Parm	Value	Std Error	t-value	95	
	Area	2162.71159	6785.1405	0.31874234	-11146.469	15471.8919
	Ctr	619.210701	2.92211615	211.90489	613.478916	624.942487
	Wid	23.1287199	25.3274338	0.91318845	-26.551516	72.8089561
	Shpe	0.19603759	2.93700052	0.06674755	-5.564944	5.95701916
Peak	18	Gauss+Lor	Area			
	Parm	Value	Std Error	t-value	95	
	Area	3322.06184	10303.1818	0.32243067	-16887.822	23531.946
	Ctr	654.303429	3.4230718	191.145108	647.589009	661.017848
	Wid	29.5904855	29.9570567	0.98776344	-29.170843	88.3518138
	Shpe	0.42459674	2.71533911	0.15636969	-4.9015918	5.75078531
Peak	19	Gauss+Lor	Area			
	Parm	Value	Std Error	t-value	95	
	Area	4958.63507	16780.8354	0.29549393	-27957.288	37874.5583
	Ctr	694.522989	11.1995219	62.0136284	672.554917	716.491061
	Wid	44.7291497	71.9118925	0.62199934	-96.327375	185.785675
	Shpe	0.39065873	2.90691195	0.1343896	-5.3113036	6.092621
Peak	20	Gauss+Lor	Area			
	Parm	Value	Std Error	t-value	95	
	Area	7083.95098	6908.30945	1.02542468	-6466.8275	20634.7295
	Ctr	720.054834	0.53889717	1336.1637	718.997777	721.111891
	Wid	20.3389345	5.48415086	3.70867524	9.5816698	31.0961992
	Shpe	0.41768898	0.7405128	0.56405369	-1.0348408	1.87021873
Peak	21	Gauss+Lor	Area			
	Parm	Value	Std Error	t-value	95	
	Area	5354.11502	4478.18168	1.19560023	-3429.9223	14138.1523
	Ctr	750.298666	5.90837425	126.989022	738.709279	761.888053
	Wid	45.4672147	10.9061101	4.16896715	24.0746753	66.8597541
	Shpe	0.3944003	0.6948657	0.56759213	-0.9685918	1.75739239

Raman Compression Series s2

p start (1 bar)

Peak	1	Gauss+Lor	Area			
	Parm	Value	Std Error	t-value	95	
	Area	40358.2059	615.570132	65.5623198	39150.7738	41565.638
	Ctr	57.9360417	0.01446316	4005.76545	57.9076724	57.964411
	Wid	2.6125404	0.05401106	48.3704714	2.50659847	2.71848233
	Shpe	0.13793846	0.04145567	3.32737239	0.05662375	0.21925318
Peak	2	Gauss+Lor	Area			
	Parm	Value	Std Error	t-value	95	
	Area	19143.2068	520.756061	36.760411	18121.7512	20164.6625
	Ctr	67.1726126	0.01802179	3727.29918	67.1372631	67.2079621
	Wid	1.8733764	0.06717284	27.888896	1.74161782	2.00513498
	Shpe	0.17433435	0.07421473	2.34905323	0.02876321	0.31990549
Peak	3	Gauss+Lor	Area			
	Parm	Value	Std Error	t-value	95	
	Area	5589.53373	700.242045	7.98228808	4216.01888	6963.04858
	Ctr	83.8775421	0.06370387	1316.67884	83.7525879	84.0024964
	Wid	1.89479096	0.2288602	8.27925079	1.44588493	2.34369699
	Shpe	0.19441342	0.28909166	0.67249749	-0.3726358	0.76146261
Peak	4	Gauss+Lor	Area			
	Parm	Value	Std Error	t-value	95	
	Area	15649.0145	842.049568	18.5844339	13997.3462	17300.6828
	Ctr	89.1448977	0.04121279	2163.03967	89.0640594	89.225736
	Wid	2.74150032	0.14790624	18.5353929	2.45138432	3.03161632
	Shpe	0.15625781	0.12660596	1.23420582	-0.092078	0.4045936
Peak	5	Gauss+Lor	Area			
	Parm	Value	Std Error	t-value	95	
	Area	15990.3215	800.669294	19.9711936	14419.82	17560.8229
	Ctr	109.907209	0.05478025	2006.32924	109.799759	110.01466
	Wid	3.34361161	0.20823684	16.056773	2.93515801	3.75206522
	Shpe	0.09045822	0.12533842	0.72171186	-0.1553913	0.33630775
Peak	6	Gauss+Lor	Area			
	Parm	Value	Std Error	t-value	95	
	Area	13249.9376	865.204677	15.3142233	11552.8509	14947.0243
	Ctr	119.147746	0.05699765	2090.39743	119.035946	119.259546
	Wid	3.03017886	0.2159247	14.0334981	2.60664562	3.4537121
	Shpe	0.09299556	0.15212814	0.61129755	-0.2054016	0.39139276
Peak	7	Gauss+Lor	Area			
	Parm	Value	Std Error	t-value	95	
	Area	74487.2294	1103.51995	67.4996674	72322.6907	76651.7682
	Ctr	133.828409	0.03397779	3938.70262	133.761762	133.895056
	Wid	6.68319608	0.13264666	50.3834485	6.42301154	6.94338062
	Shpe	0.04943701	0.03799959	1.30098805	-0.0250986	0.12397266

Peak	8	Gauss+Lor	Area			
	Parm	Value	Std Error	t-value	95	
	Area	22187.2031	890.823015	24.9064098	20439.8664	23934.5398
	Ctr	167.06799	0.09451632	1767.61	166.882598	167.253383
	Wid	5.89720952	0.37608377	15.6805744	5.15952653	6.6348925
	Shpe	0.03069635	0.10879512	0.28214818	-0.1827037	0.24409643
Peak	9	Gauss+Lor	Area			
	Parm	Value	Std Error	t-value	95	
	Area	40857.4486	1924.80421	21.2268076	37081.9724	44632.9248
	Ctr	233.643148	0.0704446	3316.69344	233.504972	233.781324
	Wid	6.81658581	0.26879884	25.3594318	6.2893407	7.34383093
	Shpe	0	0.07748674	0	-0.1519891	0.15198915
Peak	10	Gauss+Lor	Area			
	Parm	Value	Std Error	t-value	95	
	Area	54278.0297	2938.62294	18.4705662	48513.9624	60042.097
	Ctr	253.020828	0.44274748	571.478864	252.152385	253.889271
	Wid	24.0413103	1.41792436	16.955284	21.2600718	26.8225489
	Shpe	0.09576789	0.09368976	1.02218093	-0.0880033	0.27953903
Peak	11	Gauss+Lor	Area			
	Parm	Value	Std Error	t-value	95	
	Area	2.8112e+05	1504.04049	186.906572	2.7816e+05	2.8407e+05
	Ctr	509.030775	0.04247785	11983.4403	508.947456	509.114095
	Wid	19.1284382	0.16879899	113.320812	18.7973414	19.459535
	Shpe	0.03351133	0.01485869	2.25533575	0.00436622	0.06265644
Peak	12	Gauss+Lor	Area			
	Parm	Value	Std Error	t-value	95	
	Area	1.2826e+05	1256.39066	102.085483	1.2579e+05	1.3072e+05
	Ctr	668.14963	0.05159983	12948.6799	668.048418	668.250843
	Wid	12.7978393	0.20923341	61.165371	12.3874309	13.2082476
	Shpe	0	0.02672895	0	-0.0524285	0.05242846
Peak	13	Gauss+Lor	Area			
	Parm	Value	Std Error	t-value	95	
	Area	2.6543e+05	1348.76702	196.791273	2.6278e+05	2.6807e+05
	Ctr	738.622477	0.03136465	23549.5197	738.560956	738.683998
	Wid	14.9688012	0.12717685	117.700678	14.7193456	15.2182568
	Shpe	0	0.01389673	0	-0.0272582	0.02725824

Raman Decompression Series s2

p start (7.97 GPa)

Peak	1	Gauss+Lor	Area			
	Parm	Value	Std Error	t-value	95	
	Area	523.737891	68.7117258	7.62224912	388.961746	658.514037
	Ctr	63.5214747	0.14581065	435.643586	63.2354712	63.8074783
	Wid	3.54802718	0.50864196	6.97549056	2.55034007	4.54571428
	Shpe	0.26482703	0.34606289	0.76525694	-0.4139657	0.94361981
Peak	2	Gauss+Lor	Area			
	Parm	Value	Std Error	t-value	95	
	Area	732.531617	115.77682	6.32710084	505.438592	959.624641
	Ctr	80.1512373	0.2487249	322.24854	79.6633703	80.6391043
	Wid	5.89397463	0.9223472	6.39019083	4.08481616	7.7031331
	Shpe	0.11958455	0.36947979	0.32365655	-0.6051398	0.84430892
Peak	3	Gauss+Lor	Area			
	Parm	Value	Std Error	t-value	95	
	Area	1787.0047	102.971089	17.3544315	1585.02976	1988.97964
	Ctr	94.1233814	0.08441743	1114.97569	93.957799	94.2889639
	Wid	5.12660949	0.31875844	16.0830551	4.50137366	5.75184533
	Shpe	0.08444505	0.13101165	0.64456136	-0.1725307	0.34142077
Peak	4	Gauss+Lor	Area			
	Parm	Value	Std Error	t-value	95	
	Area	1152.4498	116.323603	9.9072739	924.284273	1380.61532
	Ctr	121.731309	0.2645841	460.085501	121.212335	122.250283
	Wid	7.97563444	1.05978714	7.52569466	5.89689133	10.0543775
	Shpe	0	0.24364368	0	-0.4779003	0.47790032
Peak	5	Gauss+Lor	Area			
	Parm	Value	Std Error	t-value	95	
	Area	1106.12767	97.0712597	11.3950069	915.725086	1296.53026
	Ctr	141.699263	0.15805265	896.532005	141.389247	142.009279
	Wid	5.79104843	0.59458034	9.739724	4.62479556	6.95730129
	Shpe	0.11122606	0.21384454	0.52012577	-0.3082241	0.5306762
Peak	6	Gauss+Lor	Area			
	Parm	Value	Std Error	t-value	95	
	Area	1308.74564	126.800167	10.3213242	1060.03063	1557.46065
	Ctr	172.305765	0.13554241	1271.23136	172.039902	172.571627
	Wid	5.74081165	0.50757861	11.3101922	4.74521027	6.73641302
	Shpe	0.10420822	0.19206151	0.54257732	-0.2725151	0.48093155
Peak	7	Gauss+Lor	Area			
	Parm	Value	Std Error	t-value	95	
	Area	3695.37708	215.505438	17.1474888	3272.66914	4118.08503
	Ctr	190.175897	0.18311159	1038.57924	189.816729	190.535066
	Wid	14.4597593	0.56757698	25.4762965	13.3464728	15.5730458
	Shpe	0.34644725	0.13165625	2.63145316	0.08820717	0.60468733

Peak	8	Gauss+Lor	Area			
	Parm	Value	Std Error	t-value	95	
	Area	1237.62718	262.484717	4.71504473	722.770685	1752.48368
	Ctr	237.57824	0.34519539	688.242799	236.901149	238.255332
	Wid	7.96922026	1.0286095	7.7475663	5.95163124	9.98680928
	Shpe	0.21847081	0.29648851	0.73686095	-0.3630832	0.80002481
Peak	9	Gauss+Lor	Area			
	Parm	Value	Std Error	t-value	95	
	Area	3414.84867	409.929662	8.33032832	2610.783	4218.91434
	Ctr	246.541443	0.19970729	1234.51399	246.149723	246.933163
	Wid	9.43980146	0.65145808	14.4902669	8.16198449	10.7176184
	Shpe	0	0.15216364	0	-0.2984648	0.29846476
Peak	10	Gauss+Lor	Area			
	Parm	Value	Std Error	t-value	95	
	Area	1279.02654	668.068577	1.91451385	-31.371458	2589.42454
	Ctr	282.433747	1.342398	210.39494	279.800671	285.066824
	Wid	19.2076084	4.58102434	4.19286321	10.2220561	28.1931607
	Shpe	0	0.67344102	0	-1.3209359	1.3209359
Peak	11	Gauss+Lor	Area			
	Parm	Value	Std Error	t-value	95	
	Area	1232.67827	805.852549	1.52965735	-347.97917	2813.33571
	Ctr	303.574813	1.11966595	271.129807	301.378619	305.771006
	Wid	17.9934453	4.66334663	3.85848334	8.8464201	27.1404705
	Shpe	0.03563817	0.73638753	0.04839594	-1.4087656	1.48004189
Peak	12	Gauss+Lor	Area			
	Parm	Value	Std Error	t-value	95	
	Area	2000.39572	863.365324	2.31697483	306.928566	3693.86288
	Ctr	351.080008	0.98271795	357.254092	349.152434	353.007582
	Wid	26.5375305	3.85940927	6.87606022	18.9674062	34.1076549
	Shpe	0.15318718	0.67827398	0.22584853	-1.1772284	1.48360279
Peak	13	Gauss+Lor	Area			
	Parm	Value	Std Error	t-value	95	
	Area	1081.75157	1280.97099	0.8444778	-1430.8375	3594.34067
	Ctr	395.680521	1.14248475	346.333308	393.439569	397.921473
	Wid	18.2282945	7.25353467	2.51302231	4.00068724	32.4559017
	Shpe	0.13007739	0.98032122	0.13268854	-1.7927955	2.0529503
Peak	14	Gauss+Lor	Area			
	Parm	Value	Std Error	t-value	95	
	Area	1449.62792	3581.91379	0.40470765	-5576.1967	8475.45254
	Ctr	442.324698	4.01386719	110.199136	434.451609	450.197787
	Wid	46.1104078	31.5629829	1.46090146	-15.799508	108.020324
	Shpe	0.21597445	3.58071954	0.06031594	-6.8075077	7.23945659
Peak	15	Gauss+Lor	Area			
	Parm	Value	Std Error	t-value	95	
	Area	2156.64692	1537.11432	1.40304914	-858.36021	5171.65405
	Ctr	501.08693	4.09206806	122.453225	493.060452	509.113408
	Wid	41.5617919	12.4304473	3.34354758	17.1798141	65.9437698
	Shpe	0.32443054	0.56313535	0.57611468	-0.7801438	1.42900493

Peak	16	Gauss+Lor	Area			
	Parm	Value	Std Error	t-value	95	
	Area	3198.81432	282.109763	11.3388998	2645.46384	3752.1648
	Ctr	576.272179	0.31709081	1817.37269	575.650214	576.894144
	Wid	17.8388188	1.2696613	14.050061	15.3484133	20.3292243
	Shpe	0	0.14422893	0	-0.282901	0.28290104
Peak	17	Gauss+Lor	Area			
	Parm	Value	Std Error	t-value	95	
	Area	4608.4983	1625.72917	2.83472696	1419.67559	7797.321
	Ctr	695.061731	1.17282035	592.641263	692.761276	697.362186
	Wid	28.5482094	2.96976996	9.61293628	22.7230879	34.3733309
	Shpe	0.25481144	0.20594797	1.23726124	-0.1491498	0.65877268
Peak	18	Gauss+Lor	Area			
	Parm	Value	Std Error	t-value	95	
	Area	2779.57351	3496.58594	0.79493928	-4078.8829	9638.02992
	Ctr	726.047772	1.33838824	542.479194	723.422561	728.672983
	Wid	30.8710684	12.6174371	2.44669881	6.12231516	55.6198216
	Shpe	0.35054542	1.45976194	0.24013876	-2.5127372	3.213828
Peak	19	Gauss+Lor	Area			
	Parm	Value	Std Error	t-value	95	
	Area	8130.30357	1612.45462	5.04219064	4967.51853	11293.0886
	Ctr	756.093284	0.4825154	1566.9827	755.146843	757.039724
	Wid	24.9008903	1.74932104	14.2346029	21.4696456	28.3321351
	Shpe	0.00450626	0.08440507	0.05338846	-0.161052	0.17006447